Spatial and spectral regularization in unmixing of remotely sensed data

by

PATEL JIGNESH RAMESHCHANRA
201521011

A Thesis Submitted in Partial Fulfilment of the Requirements for the Degree of

DOCTOR OF PHILOSOPHY
in
INFORMATION AND COMMUNICATION TECHNOLOGY
to

DHIRUBHAI AMBANI INSTITUTE OF INFORMATION AND COMMUNICATION TECHNOLOGY

January, 2022

Declaration

I hereby declare that

i) the thesis comprises of my original work towards the degree of Doctor of Philosophy in Information and Communication Technology at Dhirubhai Ambani Institute of Information and Communication Technology and has not been submitted elsewhere for a degree,

ii) due acknowledgment has been made in the text to all the reference material used.

Patel Jignesh Rameshchanra

Certificate

This is to certify that the thesis work entitled SPATIAL AND SPECTRAL REGULARIZATION IN UNMIXING OF REMOTELY SENSED DATA has been carried out by PATEL JIGNESH RAMESHCHANRA for the degree of Doctor of Philosophy in Information and Communication Technology at *Dhirubhai Ambani Institute of Information and Communication Technology* under our supervision.

Prof. Manjunath V. Joshi
Thesis Supervisor

Dr. Jignesh S. Bhatt, IIIT, Vadoadara
Thesis Co-Supervisor

Acknowledgments

First and above all, I praise God, the almighty, to provide me with this opportunity and grant me the capability to proceed successfully. Although the work described here was performed independently, I would never have been able to complete it if not for the support of many beautiful people. I want to offer my sincere thanks to them.

I want to begin by expressing my sincere gratitude to my supervisor Prof. Manjunath V. Joshi, with whom I have learned immensely and has had a strong influence on my development as a researcher. He has continuously encouraged me to ensure that I remain focused on achieving my goal. I am grateful to him for patiently supervising and directing my work, fruitful discussions, providing learning opportunities on several occasions, and helping me throughout all the different steps of my doctoral research endeavour for the past few years. Prof. Joshi's achievements, work ethics, and a keen eye for every crucial detail have been an inspiration throughout the years I have worked with him. Along with Prof. Joshi, I feel my self lucky to have a co-supervisor, Dr. Jignesh Bhatt, IIIT,Vadodara. I want to thank him for their constant motivation and support to pursue my research. He introduced me to the world of hyperspectral imaging and continues from there to today in my PhD journey.

On a broader note, I wish to acknowledge all the professors of DA-IICT who have inspired me directly or indirectly. I want to thank faculty Prof. Aditya Tatu and Prof. Pankaj Kumar, who have shaped my thinking about this research direction during the thesis work. I express my gratitude to Prof. K. S. Dasgupta (Director), Mr Soman Nair (Registrar), Prof. Sanjeev Gupta and Prof. Amit Bhatt, Prof. Suman Mitra. They have helped me throughout my time at DA-IICT. I want

to thank the administrative and technical staff members, Mr Ramesh Prajapati, Mr Rajendra Shah and the help-desk of DA-IICT, who have been kind enough to advise and help me in their respective roles. My gratitude also extends to the staff of the DA-IICT resource-center.

I made many new friends at DA-IICT, who helped me in many steps of my study. I thank all of them for everything that they did for me. I am thankful to Rishikant for helping me with the mathematical derivations. Thanks to Sumukh (Technicolour, France), Kamal (SVNIT, Surat), Prashant.

I am deeply thankful to my entire family for their love and support. Words can not express how grateful I am to my mother, father, and sisters for all of the sacrifices you have made on my behalf. Your prayer for me was what sustained me thus far. I acknowledge my entire family for providing me with a healthy, educated atmosphere in our family. Finally, I want to thank my best friend and my life partner Ankita. We started our life journey along with a PhD. Her constant support and encouragement make me able to reach this far. Last but not least, I want to thank our true inspiration of life, our daughter Mahasvi.

Contents

Abstract

The hyperspectral imaging opens the broad possibilities for remote sensing data analysis with it's rich spectral information. However, this has a trade-off with limited spatial details due to the presence of several hardware constraints. Hence, due to the low spatial (ground) resolution, more than one material is generally mixed in a single pixel (location) of acquired scene data. The process of identifying and then quantifying the materials present in a scene, pixel-by-pixel, is called spectral unmixing. This has three steps, 1) estimating the number of endmembers (pure pixels), 2) extracting endmembers, i.e., spectral signatures of the constituted materials, and, 3) estimating abundances, i.e., fractional contribution of each endmember across all locations in a scene. With the passive remote sensing and to achieve mathematical tractability, endmembers are considered as non-negative while abundances are constrained to non-negative as well as sum-to-one at every location. To improve the performance, one should employ regularization that captures the prior information about data.

Abundance maps are used to infer the proportions of endmembers with the given endmember signatures and reflectance value at each location. In this thesis, we begin with an algorithmic approach to estimate fractions (abundances) of materials (endmembers) in a pixel by considering linear mixture model (LMM) and where the endmembers are known. We propose the use of Inhomogeneous Gaussian Markov random field (IGMRF) as a prior on abundances that captures the smoothness as well as preserves the discontinuities among the abundance values. We obtain the IGMRF parameters using the initial estimate of abundances. Both the abundances and IGMRF parameters are refined by optimizing an energy function. A two-step iterative approach is proposed to obtain the final estimates

of both the abundance maps and their prior parameters. In order to demonstrate the efficacy of the proposed approach, we conduct experiments on the synthetic hyperspectral images (HSIs) with different noise levels as well as on the real HSIs and compare our results with other state-of-the-art approaches.

The IGMRF prior captures the smoothness and preserves discontinuities among abundance values locally. Besides, abundance maps exhibit redundancy which can be taken into account by another prior called sparsity-induced prior. We then build upon our first work and include sparsity-induced prior along with IGMRF prior. Here, we calculate IGMRF parameters at every pixel location, learn a dictionary and the sparse representation for abundances using the initial estimate in phase one; while the final abundance maps are estimated in the phase two. In order to learn the sparsity, we use the approach based on K- singular value decomposition (K-SVD). Both the IGMRF and sparseness parameters are initialized using an initial estimate of abundances and refined using the two-phase iterative approach. The experiments are conducted on the synthetic HSIs with different noise levels as well as on two real HSIs. The results are qualitatively and quantitatively compared with state-of-the-art approaches. Experimental results demonstrate the effectiveness of the proposed approach.

We note that the abundance maps contain spatial information of the HSI. Hence, we seek to use abundance maps to enhance the spatial resolution of the HSI. We transfer the mapping from the low-resolution (LR) and high-resolution (HR) natural images learnt by a deep convolutional neural network (CNN) to get the initial estimates of the super-resolved abundance maps where the input corresponds to LR abundances maps. To get the better estimates of abundances and in turn improve the super-resolution (SR) of HSIs, we use a regularization framework in which both the LR and HR abundances are modelled as IGMRF that serves as the prior. Finally, the SR HSIs are obtained by using a linear mixing model that uses the SR abundances and the endmembers estimated using an appropriate technique. Experiments on synthetic as well as on real HSIs show that the proposed method performs better when compared to other existing SR approaches. One can see that the method do not require auxiliary image as used in many of the existing

SR methods and, the spectral details are better preserved since the SR is carried out in abundance domain. Moreover, computational complexity is reduced since the SR is carried out on abundances which are a few in number when compared to the number of hyperspectral band images.

Finally, we propose a novel approach for jointly estimating endmembers and abundances based on unsupervised learning using autoencoder with IGMRF as prior for regularization. The decoder part of proposed autoencoder has linear weights making it a LMM. The weights represent the endmember matrix that makes the hidden units of autoencoder as abundances. IGMRF is used to apply spatial regularization on abundances that also preserves the discontinuities. To incorporate the spectral regularization, we use IGMRF priors on endmembers. In addition, we also apply the spatial and spectral regularizations on the given HSI. IGMRF parameters at every pixel location are calculated using initial estimates of endmembers and abundances. We obtain both the endmembers and their abundances by optimizing the energy function that consists of a data term and IGMRF prior terms. Experiments are performed with different noise levels on the synthetic data and on two real data (Jasper ridge and Urban). The results of the proposed approach are better when compared to the existing state-of-the-art approaches.

Keywords:

Abundance estimation, Autoencoder, Deep learning, Inhomogeneous Gaussian Markov random field (IGMRF), Hyperspectral image (HSI) super-resolution, K-singular value decomposition (K-SVD), Regularization, Sparse representation, Spectral unmixing, Transfer learning.

List of Tables

List of Figures

CHAPTER 1

Introduction

The term remote sensing refers to the process of monitoring and detecting scene that has no or limited direct exploration without direct contact of it. It collects the physical characteristics of the scene by measuring radiance emitted or reflected by it. There are two types of sensing techniques and they correspond to active and passive [1]. An active sensor has an external source of energy and captures the reflectance from the object while the passive sensor do not require the external energy source. Every material has the characteristics to react to each spectrum range differently. In remote sensing, multispectral sensors capture reflectance in 4 to 6 visible and infrared wavelength bands, while the hyperspectral sensors capture the reflectance in hundreds of contiguous bands in visible and near-infrared range, each with a narrow bandwidth. Hence, they provide rich spectral details that make the signatures (reflectance) distinguishable. Such sensors are airborne to capture the selected area. To capture larger area, sensors can be mounted on the spaceborne platform. In the case of hyperspectral images (HSI), the reflectance value at a pixel represents the average of the material's reflectance within the instantaneous field of view (IFOV). Due to this, the spatial resolution depends on IFOV. The spectral resolution of sensors is determined by the spectral width of each band and the number of spectral bands [2].

Hyperspectral imaging emerges to identify new landcover classes remotely that are difficult to identify with lower spectral resolution images. Researchers successfully used hyperspectral images to identify minerals and map vegetation species [3, 4], measure water vapour in the atmosphere [5], geological mapping [6] and many more. Hyperspectral imaging is not only used in remote sensing but

also explored for lab-scale applications such as food safety [7, 8], quality control in the pharmaceutical industry [9], biomedical [10], forensic [11] etc.

Many signal processing techniques are used or developed for hyperspectral imaging to better understand the hyperspectral data. Dimensionality reduction, target detection, change detection, classification and spectral unmixing are the most investigated techniques in the domain of hyperspectral imaging [12]. Since the hyperspectral data has high spectral dimension, dimensionality reduction is often explored to reduce the same that aids in succeeding processing tasks. Target or anomaly detection techniques locate pixels in the scene with specific known or unknown spectral signature. The HSI data recorded for a particular scene at different acquisition times gives the temporal dimension to the HSI data which can be used to detect changes in specific region. Classification and spectral unmixing techniques are developed to identify and analyse the hyperspectral data at a pixel location [13]. In classification, the goal is to assign the class to each pixel, whereas spectral unmixing gives the fractions (abundances) of the materials (endmembers) present at the pixels. A spectral unmixing technique gives the sub-pixel information that helps in better analysis of the remotely sensed data. Hence, the researchers continue to explore the spectral unmixing area to improve the performance of the various remote sensing applications [14–17].

1.1 Hyperspectral data

Hyperspectral data is recorded in hundreds of contiguous bands with very narrow bandwidth. HSI sensors are mounted on airborne or spaceborne craft to capture the reflected light energy of the sun from the scene (passive remote sensing). These sensors have a number of filter banks to capture images in the visible, near-infrared, and shortwave infrared spectral bands. Hence, the HSI imaging is also referred to as the imaging spectroscopy, which combines both imaging and spectroscopy. Spectroscopy gives detail properties of the material by using the interaction between material and electromagnetic radiation as a function of the wavelength. One may note that, the term hyperspectral is used due to the large

Table 1.1: Hyperspectral datasets

Datasets	Parameter				
	Altitude of vehicle (km)	Spatial resolution (m)	Spectral resolution (nm)	Spectral range (μm)	Number of bands
HYDICE [18]	1.6	0.75	7-14	0.4-2.5	210
AVIRIS [19]	20	20	10	0.4-2.5	224
HYPERION [20]	705	30	10	0.4-2.5	220
EnMAP [21]	653	30	6.5-10	0.4-2.5	228
PRISMA [22]	614	5-30	10	0.4-2.5	238
CHRIS [23]	556	36	1.3-12	0.4-1.0	63
HyspIRI [24]	626	60	4-12	0.38-2.5	217

number of spectral bands for a single pixel location. Few of the hyperspectral datasets with their specifications are shown in Table 1.1.

HSIs data can be seen as a stack of images registered for the same scene area where each image represents radiance in the respective bands. HSI data can be visualized as HSI cube, as shown in Figure 1.1. The scene shown in Figure 1.1 consists of four materials, and these are: soil, water, rock and vegetation. To better understand, the plots of reflectance vectors of pure and mixed pixels are also shown in the same figure. There are hardware, signal-to-noise ratio (SNR) as well as recording time constraints that limit the IFOV of the HSI sensor resulting in low spatial resolution. HSI data is spectrally smooth and has the spatially piecewise smoothness similar to the natural images. Hence, the analysis tools used for natural data can also be employed for HSIs [13, 25].

1.2 Linear mixing model

HSI has a low spatial resolution, and hence the value of each pixel represents more than one material rather than a specific material. In order to take care of this, spectral unmixing techniques analyze both pure and mixed spectrums. Here, the pure spectrum is reflectance caused due to interaction with one material while the mixed spectrum has reflectance having interaction with more than one material. In the study of the spectral unmixing, both linear and non-linear mixture models have been used to model hyperspectral data [12]. In the checkerboard type scene, reflectance received at sensor has undergone single reflection, and hence reflectance can be modelled as a linear mixture. In other scenarios such as

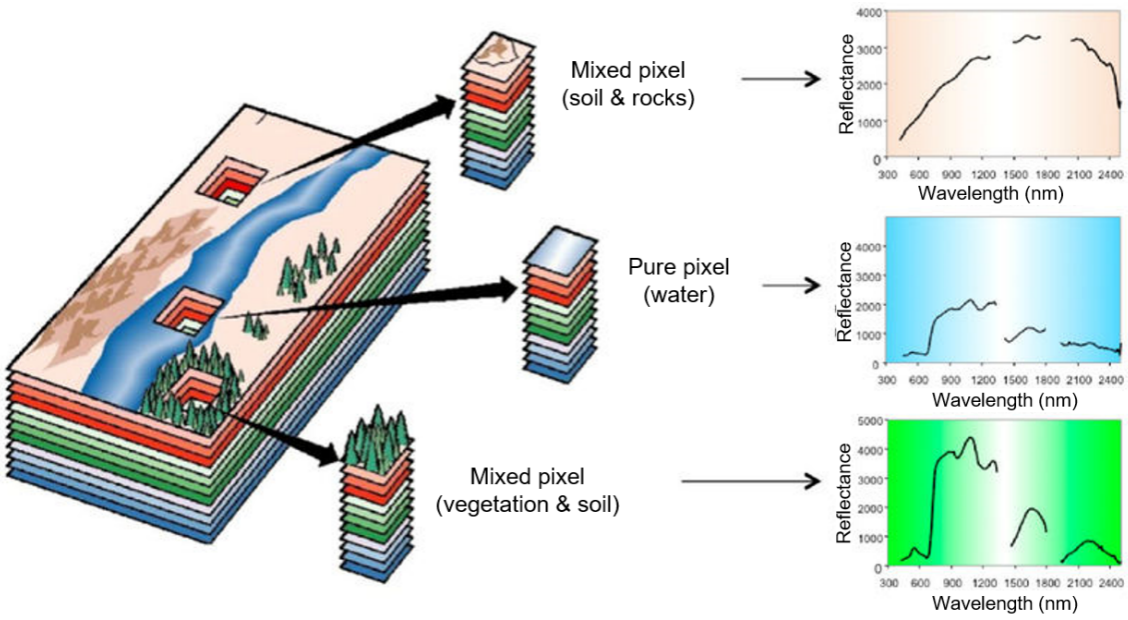

Figure 1.1: Hyperspectral data cube and pure and mixed pixels reflectance [26].

multilayer structure or an intimate mixture of materials, reflectance received at the sensor has undergone multiple reflections, leading to the non-linear mixture. Non-linear mixing model is too complex since mimicking a complete physical phenomena is challenging. In addition to this, it relies on scene parameters making it too difficult to solve the unmixing problem [13]. On the contrary, LMM is mathematically tractable and can represent hyperspectral data accurately. Hence, LMM is widely used in hyperspectral data analysis when compared to the non-linear model.

In LMM, the data forms a simplex with endmembers as a vertex of it and the reflectance represented as linear combination of endmembers [27]. In this model, the reflectance value at each pixel can be considered as a linear combination of endmembers present in the data. A mixed data for single input vector of reflectance can be modeled as,

$$\mathbf{r} = \mathbf{M}\alpha + \eta, \tag{1.1}$$

where, $\mathbf{r} \in R^{l\times 1}$ denotes the spectral measurement, $\mathbf{M} \in R^{l\times p}$ is the endmember matrix, $\alpha \in R^{p\times 1}$ is called the abundance vector. Here, l represents the number of spectral bands, p is the number of endmembers and $\eta \in R^{l\times 1}$ corresponds to

independent and identically distributed (IID) white Gaussian noise.

1.3 Thesis contribution

In this section, we discuss contribution of the thesis in brief and the details of the same are discussed in the subsequent chapters.

The mixed pixel problem is caused by the lower spatial resolution of the data in which each pixel may represent more than one endmember. In this connection, to start with, in the chapter on literature review, we discuss various spectral unmixing techniques. Abundance estimation refers to estimation of the fraction of endmembers at every pixel location given the endmembers and HSI data. Abundance maps have spatial information about the data that is smooth with limited discontinuity. In our first work, we use Inhomogeneous Gaussian Markov random field (IGMRF) regularization to capture this spatial information to obtain better estimate of the abundance maps. Abundance maps also have spatial redundancy. Taking this into account, we use sparsity induced prior in addition to IGMRF for improving the abundance estimation in our next work. We used the K- singular value decomposition (K-SVD) [28] algorithm to learn sparsity in the abundance maps.

We know that HSI data has low spatial resolution due to various constraints. Many researchers have developed algorithms to super-resolve HSI image using the available high-resolution auxiliary image of the same scene. Since the spatial details are contained in abundances and the auxiliary image is rarely available, one may super-resolve abundances and use them in obtaining the super-resolution of HSIs. Hence, in our next work, we use transfer learning based approach to super-resolve HSIs where we use super-resolution of abundances. To improve the solution, we use spatial regularization on the abundance maps.

An autoencoder compresses higher dimensional data to lower dimension represented by hidden units as encoder and reconstructs back using the decoder. Spectral unmixing can be formulated in an autoencoder framework where hidden units represent abundance values and the decoder weights correspond to the

endmembers. By making use of autoencoder, we perform unsupervised spectral unmixing as our final contribution. Here, both the endmembers and the abundances are unknown. We use autoencoder framework with spatial and spectral regularization that results in better estimates of abundances and endmembers. In all, our thesis includes following contributions:

- Given the HSI and endmembers present in the data, abundances (material maps) are estimated using IGMRF as prior using an optimization framework..
- Given the HSI and endmembers, abundances are estimated using IGMRF and sparsity induced priors.
- Super-resolution (SR) of HSI is obtained using the transfer learning with spectral unmixing and IGMRF regularizer, where we use the input as the given low resolution HSI data.
- Both the endmembers and their abundances are estimated using an autoencoder framework with spatial and spectral regularizations with the input as low resolution HSIs where the number of endmembers is known.

1.4 Thesis organization

The contents of this thesis are organized as follows. The literature review is presented in chapter 2. Use of modified IGMRF parameters for abundance estimation is discussed in chapter 3. We extend the work on abundance estimation in chapter 4 using the regularization framework in which we make use of IGMRF and sparsity induced priors. In chapter 5, we discuss the HSI SR using transfer learning, spectral unmixing and IGMRF regularizations. We then discuss an autoencoder framework with spatial and spectral regularizations for simultaneous estimation of endmembers and abundances in chapter 6. Finally, we conclude the thesis in chapter 7.

CHAPTER 2

Literature Review

Hyperspectral camera (HSC) gives advantage of capturing the broad electromagnetic spectrum covering near-infrared, shortwave infrared with visible bands of a scene. HSCs help us to introduce the spectroscopic analysis in imaging to enable material identification. However, HSCs mounted on the spaceborne/airborne have hardware constraints that lead to reduction in spatial ground resolution of resultant hyperspectral images (HSIs). Hence, spectra measured by the HSCs can be the mixture of spectral signatures of materials present in the scene. To address this mixed pixel phenomena and to better analyse the HSI data, researchers are exploring HSI unmixing since past three decades. The process of decomposing pixel spectra into a set of pure spectral signatures (endmembers) and their fractions (abundances) is referred to as spectral unmixing. This is a challenging inverse ill-posed problem due to mixing characteristics, correlations among the hyperspectral signatures, endmember variability, size of the data, noise; and hence it is difficult to find a suitable model to find inverse for getting the unknowns.

Mixing of spectra depends on how incident light interacts with the materials. In case incident light interacts with only one material, reflected light is not mixed and has only one material signature within a pixel resolution. However, due to hardware limitations of the sensors, mixing of spectra occurs at the sensors. In such cases, abundances (fractions) represent the amounts of endmembers in each pixel and hence can be modelled as a linear mixture [29]. However, there are possibilities of incident light interacting with more than one material when the surface has a multilayered structure or intimate mixture of materials. In order to replicate these physical conditions of the surface, the non-linear mixing model can

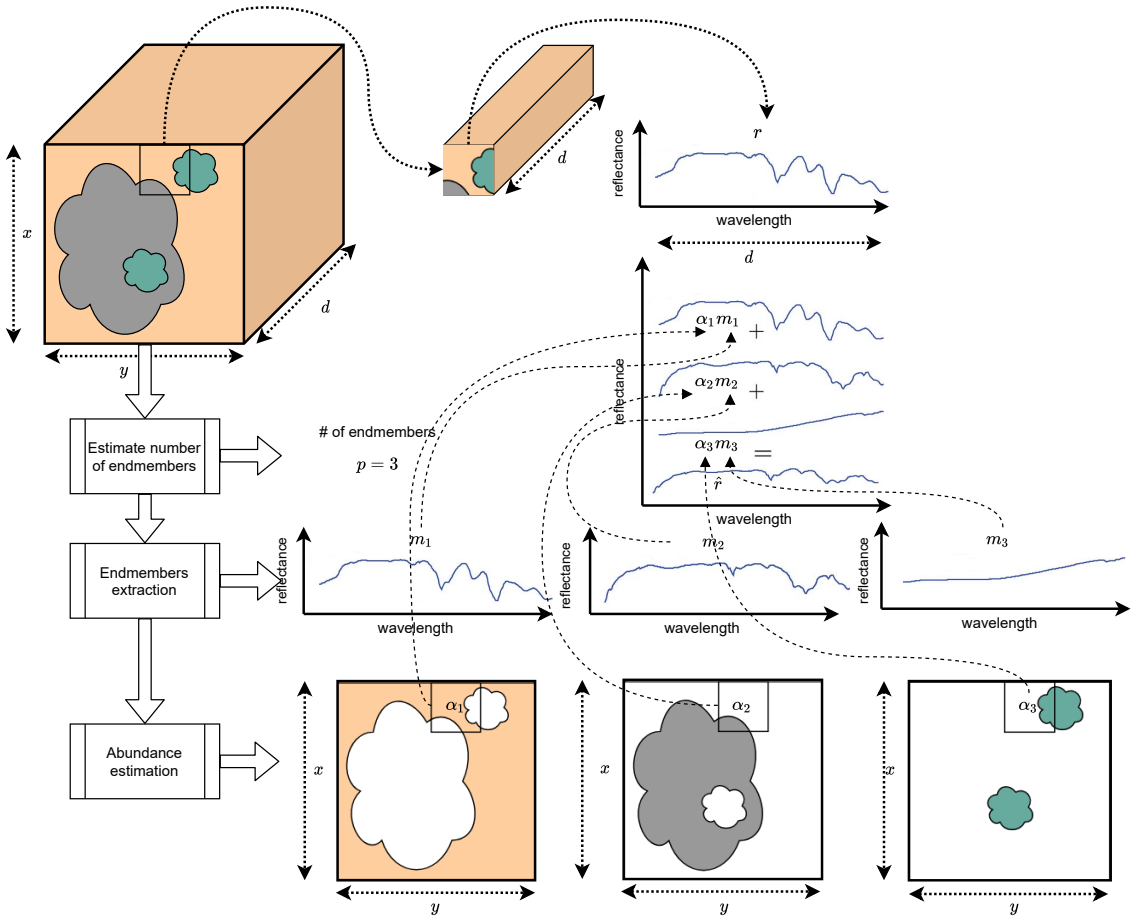

Figure 2.1: Spectral unmixing process.

be used to solve for the unmixing. In [30], the authors proposed a model to address multilayer scattering by representing the reflectance as an infinite sequence of power of products of pure spectra. However, only first-order terms of this infinite series referred to as the bilinear mixing model are enough for the spectral unmixing. The Hapke model is used to address microscopic or intimate mixing, which is a too complex ill-posed problem since it relies on the scene parameters. These two mixing scenarios (multilayered and microscopic) have a different physical structure, and hence both cannot be modelled using the same modelling technique. In addition to that, non-linear models generally require prior knowledge of endmembers. Most of the real scenario suggests macroscopic mixing and hence mathematically tractable linear mixing model (LMM) is explored to a great extent compared to the non-linear models.

Remotely sensed hyperspectral data requires atmospheric correction as the ra-

diance since the HSC is affected by the scattering of light. Radiance received at sensors is converted to reflectance for atmospheric corrections. HSI data is then presented for further preprocessing and analysis. HSI unmixing can be classically illustrated as the three-step process after considering atmospheric corrections and preprocessing of data. The unmixing process is shown in Figure 2.1. In the figure, we have shown HSI cube with dimension $x \times y \times d$ where each pixel is recorded in d spectral bands. The first step in unmixing is the estimation of number of pure signatures (endmembers) p present in the scene. The second step would be the extraction of endmembers m_1, m_2 and m_3. To better understand, a single pixel is illustrated by using a small rectangular box. The final step corresponds to the estimation of abundances of each endmembers in a scene. Here, for the selected mixed pixel, we have shown abundance values as α_1, α_2 and α_3 for endmembers m_1, m_2 and m_3, respectively. The abundance values have to satisfy the condition that $\alpha_i > 0$, $i = 1, 2, 3$ (non-negativity constraints) and $\sum_{i=1}^{3} \alpha_i = 1$ (sum-to-one constraints).

2.1 Estimation of number of endmembers

Hyperspectral data is recorded at hundreds of spectral bands, and the number of endmembers present in a scene is often less than the number of bands. Hence, if a linear mixing model is used, the data can be conveniently represented by lower-dimensional linear subspace [12]. This is also the accurate representation of a spectral vector since it helps to decrease the computational complexity and enhance signal-to-noise ratio (SNR) [12]. This makes the signal subspace identification as the first processing step in hyperspectral data analysis as depicted in Figure 2.1. It also is the number of endmembers present in HSI [31].

Band selection based techniques are developed for unsupervised subspace identifications that select higher SNR bands to represent the data [32]. Also, projection-based dimensionality reduction techniques can find subspace of the data in an unsupervised way [33]. In [34], a real-time system measures angle metric between every new pixel spectra with already defined pure pixel spectra and

if it is sufficiently different, then add them into a pure pixel set. In another similar work, the authors extract pure pixels using orthogonal projections by the modified Gram-Schmidt procedure [35]. The eigenvalues of sample correlation and the covariance matrices are used to estimate the number of endmembers in the data in [36]. Along with this, the virtual dimensionality (VD) method [37] includes noise covariance as a noise-whitening step. Recently, VD based methods have been proposed to control false discovery rate and to avoid false estimation of the number of endmembers [38, 39]. The fully automatic and unsupervised HySime algorithm estimates the signal and noise correlation matrices and then performs eigen decomposition [31]. HySime selects a subset of eigenvalues that represent best signal subspace. In the case of non-linear mixing, linear subspace is replaced with low dimensional manifold to estimate the number of endmembers [40].

2.2 Endmember extraction

The second step in the spectral unmixing process is the extraction of endmembers. Researchers have used geometry based approaches to solve linear spectral unmixing by representing HSI data as simplex and hence vertices of a simplex represent endmembers of the data. Few of these approaches assume that pure pixel spectra for each endmember is present in the data. This assumption makes them computationally less taxing. The pixel purity index (PPI) [41, 42] is an endmembers extraction algorithm that finds the pure pixels from the data. It uses maximum noise fraction (MNF) dimensionality reduction technique as preprocessing step to improve the SNR of the spectral vector. After that, it projects each spectral vector of the data on a large set of random vectors known as skewers. The spectral vectors marked as extreme for each skewer direction highest number of times are considered as pure pixels. The simplex form by the purest pixels (endmembers) represents the maximum volume. Using this fact, N-FINDER in [43] finds a set of pixels from the data that form the largest volume simplex. The vertex component analysis (VCA) proposed by the authors in [44] iteratively projects data onto a direction orthogonal to the subspace spanned by already estimated

endmembers. Here, The new endmember signature corresponds to the extreme of the projection, and algorithm iterate till it exhausts all the endmembers. The HSI data is represented as the convex cone, sequential maximum angle convex cone (SMACC) in [45] which starts with the first endmember (brightest pixel in the image) and identifies the new endmember that has a maximum angle with the existing cone. The algorithm keeps increasing the dimension of the cone till it covers all the data points with some tolerance.

Non-negative matrix factorization (NMF) is widely used method to analyse high dimensional data [46]. The minimum volume constrained -Non-negative matrix factorization (MVC-NMF) [47] is the NMF based method used to extract endmembers. MVC-NMF, minimum volume simplex analysis (MVSA) [48] and the simplex identification via variable splitting and augmented Lagrangian (SISAL) [49] use the minimum volume of the simplex concept for extracting endmembers. These geometric methods do not require pure pixel assumption.

Geometric methods fail when the data is highly mixed. In such cases, statistical methods perform better; however at a higher computational cost [12]. As spectral unmixing is the problem of blind source separation, independent component analysis (ICA) [50] also can be used for the same. However, ICA requires independent sources as a condition which is not the case in hyperspectral data [51]. To overcome this limitation a dependent component analysis is proposed in [52]. Other statistical methods are proposed in [53, 54] use Bayesian approaches to take care of endmember variability.

2.3 Abundance estimation

Abundance estimation refers to obtaining the fractions of endmembers at every pixel location given the endmembers. These endmembers are known apriori or can be obtained using endmember extraction algorithms. Number of researchers have developed statistical and geometric approaches for abundance estimation [12]. Most of the statistical approaches are constrained least-squares sense based. Unconstrained optimization methods using orthogonal subspace projection gives

a solution with negative abundance value or total abundance as higher than 100% [55]. However, we know that the abundances cannot be negative, and their sum at each pixel should be one. Hence, partially constrained solutions with sum-to-one constrained least square (SCLS) [56] and non-negative constrained least square (NCLS) [57] are proposed for the same. SCLS has a closed form solution and hence computationally effective when compared to NCLS, but the solution provided by NCLS is practically acceptable than that given by SCLS. A fully constrained least squares (FCLS) [58] is a well-known algorithm that yields most acceptable solution using quadratic programming. It imposes both non-negativity and sum-to-one constraints while solving the problem. In [59], a maximum entropy-based algorithm is proposed which represents the geometric version of FCLS. One of the other geometric-based algorithms i.e., simplex projection unmixing (SPU) [60], uses orthogonal projection and yields computationally efficient solution when the number of endmembers is relatively less.

The semi-supervised spectral unmixing algorithms estimate the fractions as a linear combination of a subset of spectral signatures from the spectral library. Here, the number of endmembers is much smaller than spectral signatures available in a spectral library [61]. Hence, techniques such as linear sparse regression techniques based on sparsity-inducing regularizers are used to estimate abundances [62]. Few researchers have developed sparse unmixing algorithms by imposing spatial regularization on abundances leading to better accuracy and robustness [63–65]. The Tikhonov regularization within the total least square (TLS) estimation framework is proposed for abundance estimation when outliers are present in the data [66]. In [67], Huber Markov random field is used to apply spectral regularization on abundance. The abundance estimation problem is also explored in the wavelet domain, where the smoothness prior is imposed to improve the solution [68].

2.4 Complete spectral unmixing

Researches also have attempted complete spectral unmixing where they perform all the three steps of unmixing [69]. However, this unmixing performed by three steps chain process struggled with error propagation at each stage, inconsistent estimation of the number of endmembers and computational complexity [35]. A New Fast Algorithm for Linearly unmixing referred to as FUN [35] is based on orthogonal projection using the modified Gram-Schmidt method and it performs the estimation of the number of endmembers and also extracts them. NMF is used for joint estimation of endmembers and abundances in [70]. Multilayer NMF uses successive layers to decompose endmembers and abundance matrices by applying sparsity on these matrices [71]. Robust collaborative NMF uses collaborative regularization to perform complete unmixing by removing redundant endmembers [72]. In [73], complete spectral unmixing is performed using temporal hyperspectral data by modelling temporal variation in abundance maps.

Statistical-based approaches are more suitable than those based on geometry for highly mixed data and hence Bayesian framework is explored for joint estimation of endmembers and abundances. In [74], Bayesian model and Markov Chain Monte Carlo are used to estimate endmembers and their abundances. Here, authors used subspace rather than observational space and iteratively maximized the negative log-posterior distribution. A hierarchical Bayesian model is proposed in [75] which incorporates non-negativity constraint by applying Gamma prior on endmembers. Dependent component analysis used in [76] uses Dirichlet density to enforce the non-negativity and sum-to-one constraints on the abundances.

2.5 Deep learning for hyperspectral unmixing

Deep learning based approaches out perform in every field of studies and they are also investigated for solving various problems in remote sensing. Various Deep learning frameworks are used for hyperspectral unmixing problems [77]. To ex-

tract features from the HSI an auto-associative network is used and the extracted features are then made use of in abundance estimation in [78]. In [79], a deep convolution neural network based approach is proposed for abundance estimation.

Autoencoder represents a widely used unsupervised network. Therefore, unsupervised based spectral unmixing can be modelled by using autoencoder and incorporating various constraints such as non-negativity and sum-to-one. In [80], authors concatenate marginalizing denoising autoencoder (mDA) with non-negative sparse autoencoder (NNSAE) for joint estimation of endmembers and abundances. Here, mDA is used to denoise data while NNSAE extracts endmembers as decoder weights and their abundances as hidden units. However, NNSAE uses tied weights that results in compromising on the accuracy in extracted endmembers. In [4], the authors used untied denoising autoencoder (uDAS) by imposing sparsity and denoising constraints that overcame the limitation of tied weights.

CHAPTER 3

Abundance estimation using discontinuity preserving prior

We begin by addressing the problem of abundance estimation in this chapter. It is the task of estimating fractions of the endmembers at every pixel location, given the endmember signatures and hyperspectral image (HSI). Linear spectral unmixing algorithms assume that an observed hyperspectral spectrum is a convex combination of endmember spectra and their coefficients are the fully constrained abundances. Hence, most of these algorithms represent every pixel spectrum within the convex hull formed by the endmembers. Once the endmembers are estimated from the data, abundance estimation can be derived by inverting the data model for the unknown coefficients. In [81], ordinary least-squares linear regression is used to solve an overdetermined linear equations system. However, accurate abundance estimation is difficult when we consider noisy data with possible error in endmember extraction. Therefore, various constraints are incorporated to estimate the abundances. Statistical approaches based on partial and fully constrained least square-based solutions are proposed for the same [56–58]. Among them, fully constrained least squares (FCLS) method provides an accurate and computationally effective solution. Simplex projection unmixing uses a sequence of orthogonal projections to give a faster solution with accuracy similar to FCLS [60]. In [82], dimensional geometry is used for a fast and effective abundance estimation by using distances among the endmembers and the observed pixels.

Interestingly, most of abundance estimation algorithms show limited perfor-

mance when the data is noisy or there are outliers and give an inaccurate estimate of abundances. Use of regularization improves the solution by capturing the dependencies present in the data [83]. Since the abundance maps are generally found spatially smooth with discontinuities at places; this property, in practice, can be captured by making use of Markov random field (MRF) based priors. Note that, the homogeneous MRF does not take into account the presence of discontinuities in the abundance values. Notably the Inhomogeneous Gaussian Markov random field (IGMRF) based prior models have been successfully used for satellite image deblurring [84], multiresolution fusion of satellite images [85], and in disparity estimation [86]. To this end, IGMRF prior can be used to capture the smoothness and also preserve the discontinuity [84]. However, the estimation of the prior parameters requires the availability of true abundances which themselves have to be estimated. To this end, one may use initial estimate of abundance maps to initialize the IGMRF parameters, which can be refined iteratively.

In this chapter, we use IGMRF prior on abundances to capture spatial dependencies in order to improve abundance estimation. The expressions for computing these parameters are modified appropriately. We estimate the IGMRF parameters by using an initial abundance map and modify them iteratively. To get the final estimate, an objective function consisting of data fitting and prior terms is formulated and optimized using Adam optimization [87]. Using an iterative approach, refined abundance maps are used to reinitialize the IGMRF parameters and again the optimization is carried out in order to obtain the final abundances. Doing so, as a by-product, we get the refined IGMRF parameters leading to better estimates of both the abundances and IGMRF parameters. The block diagram of the proposed approach is shown in Figure 3.1.

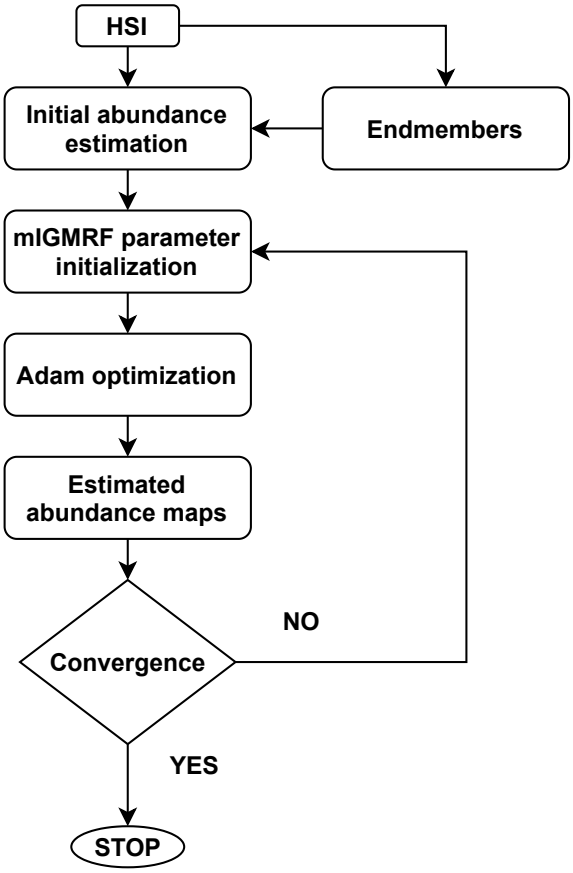

Figure 3.1: Block diagram of abundance estimation using IGMRF.

3.1 Problem Formulation

Linear mixture model (LMM) is widely used for hyperspectral image analysis [61]. In this model, the reflectance value at each pixel can be considered as a linear combination of endmembers present in the data. A mixed data for single input vector of reflectance $\mathbf{r}$ can be modeled as,

$$\mathbf{r} = \mathbf{M}\boldsymbol{\alpha} + \boldsymbol{\eta}, \tag{3.1}$$

where, $\mathbf{r} \in R^{l\times 1}$ denotes the spectral measurement, $\mathbf{M} \in R^{l\times p}$ is the endmember matrix, $\boldsymbol{\alpha} \in R^{p\times 1}$ is called the abundance vector. Here, l represents the number of spectral bands, p is the number of endmembers and $\boldsymbol{\eta} \in R^{l\times 1}$ corresponds to independent and identically distributed (IID) white Gaussian noise. The abundance vector follows the abundance non-negativity constraint (ANC):

$\alpha_i \geq 0$, for $i = 1, .., p$ and a abundance sum-to-one constraint (ASC): $\sum_{i=1}^{p} \alpha = 1$.

We formulate abundance estimation problem in an energy minimization framework. Given the hyperspectral data and the endmembers, we estimate the abundances $\boldsymbol{\alpha}$ by minimizing the following energy function (cost function),

$$E(\boldsymbol{\alpha}) = E_D(\boldsymbol{\alpha}) + E_P(\boldsymbol{\alpha}), \tag{3.2}$$

where, $E_D(\boldsymbol{\alpha})$ represents the data fitting term measuring the reconstruction error between the given and the reconstructed reflectance. $E_P(\boldsymbol{\alpha})$ represents the prior term that constraints the smoothness and discontinuity of abundance values. Using the LMM Eq. (3.1), the data term $E_D(\boldsymbol{\alpha})$ in Eq. (3.2) can be obtained as,

$$E_D(\boldsymbol{\alpha}) = \sum_{(x,y)} \|\boldsymbol{r}(x,y) - \boldsymbol{M}\boldsymbol{\alpha}(x,y)\|_2^2, \tag{3.3}$$

where, $r(x,y)$ represents the spectral measurement at (x,y) pixel location and $\boldsymbol{\alpha}(x,y)$ represents the abundance vector consisting of abundance values for each endmember. We define the prior term $E_P(\boldsymbol{\alpha})$ using the modified IGMRF (mIGMRF) as follows.

3.2 Proposed mIGMRF prior for abundances

Abundance estimation is an ill-posed problem, and hence additional regularization is necessary to make it better posed. Abundance maps are spatially smooth with discontinuities at some places. Markov random field (MRF) based models can capture smoothness in abundance maps. However, they use small number of global parameters while regularizing. In practice, abundance maps do not have the uniform variation at each pixel location and may exhibit sudden changes, i.e., discontinuities. Therefore, we propose to employ IGMRF prior that considers the spatial variation among abundances locally. The fact that the abundance maps have both smoothness as well as discontinuities motivates us to use the IGMRF as a prior. IGMRF parameters are spatially varying at each pixel location, and hence they take care of varying degrees of spatial smoothing. Due to this, the

IGMRF can control smoothness as well as discontinuities with in the abundance maps.

We model the abundance map by an IGMRF prior in our energy function that adjusts the amount of regularization locally. While using IGMRF prior, one can write the prior term $E_P(\boldsymbol{\alpha})$ as the sum of squares of finite difference approximations to the first order derivatives of abundances at each pixel location (x, y) for each of the endmember p [84] as follows,

$$\begin{aligned} E_P(\boldsymbol{\alpha}) = \sum_{(x,y)} \sum_{p} & b^{x}_{(x,y,p)} (\alpha(x-1,y,p) - \alpha(x,y,p))^2 \\ & + b^{y}_{(x,y,p)} (\alpha(x,y-1,p) - \alpha(x,y,p))^2, \end{aligned} \tag{3.4}$$

where, b^x and b^y are the spatially adaptive IGMRF parameters in horizontal and vertical directions, respectively. In [84], the authors derive the expressions for IGMRF parameters as,

$$\begin{aligned} b^{x_{IGMRF}}_{(x,y,p)} &= \frac{1}{\max(4(\alpha_{in}(x-1,y,p) - \alpha_{in}(x,y,p)))^2, 4)}, \\ b^{y_{IGMRF}}_{(x,y,p)} &= \frac{1}{\max(4(\alpha_{in}(x,y-1,p) - \alpha_{in}(x,y,p)))^2, 4)}, \end{aligned} \tag{3.5}$$

where, $\boldsymbol{\alpha}_{in}$ represents initial estimate in our work which is obtained by using FCLS [58]. One may observe that the IGMRF parameters computed using Eq. (3.5) take a regularizer value of 0.25 if neighbouring pixels have a difference of less than or equal to 1. We know that abundance values vary between 0 and 1. Hence, such a computation given in Eq. (3.5) apply a constant penalty of 0.25 at every location, as shown in the Figure 3.2. This motivates us to modify the expression given in Eq. (3.5) for proper regularization. We know that the logistic function varies smoothly from 0 to 1 [88]. Hence, we modify the expressions for computing the IGMRF parameters appropriately, by using logistic function. This makes them to vary from high to low as the input difference d_x varies from 0 to 1. With this, the

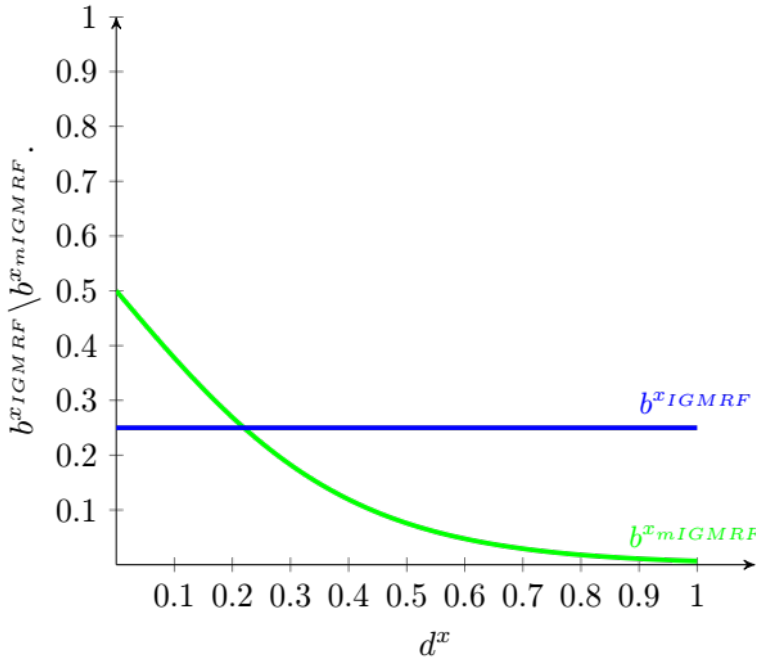

Figure 3.2: IGMRF parameter $b^{x_{IGMRF}}$ and modified IGMRF parameter $b^{x_{mIGMRF}}$ with the difference d^x (between two neighboring abundances).

modified expressions for computing the parameters are now given as,

$$
\begin{aligned}
b^x_{(x,y,p)} &= 1 - \frac{1}{1 + \mathrm{e}^{-5\times|(\alpha_{in}(x-1,y,p) - \alpha_{in}(x,y,p))|}}, \\
b^y_{(x,y,p)} &= 1 - \frac{1}{1 + \mathrm{e}^{-5\times|(\alpha_{in}(x,y-1,p) - \alpha_{in}(x,y,p))|}}.
\end{aligned}
\tag{3.6}
$$

Here, the constant 5 used in the exponential terms is chosen to balance the weightage given for smoothness as well as discontinuities and we have arrived at this value via experimentations.

In Figure 3.2, we show the variation of b^x (modified parameter) w.r.t variation in $d^x = |\alpha_{in}(x-1,y,p) - \alpha_{in}(x,y,p)|$. As shown in Figure 3.2, the proposed parameter now has a larger penalty for smaller differences (smooth region) and smaller penalty for higher differences (edges). Thus, we have arrived at mIGMRF parameters for abundance estimation. In Figure 3.3, we show an illustration for mIGMRF prior on abundance maps. Here, Ammonioalunite abundance map of synthetic data (will be discussed in section 3.4.1) is used where mIGMRF parameters are computed for selected regions displayed by blue square in Figure 3.3 (a). These calculated parameters for the selected region (Figure 3.3 (b)) for horizon-

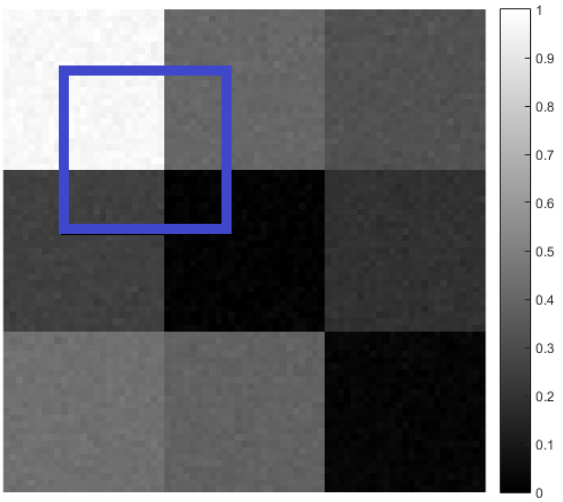

(a) Ammonioalunite abundance map

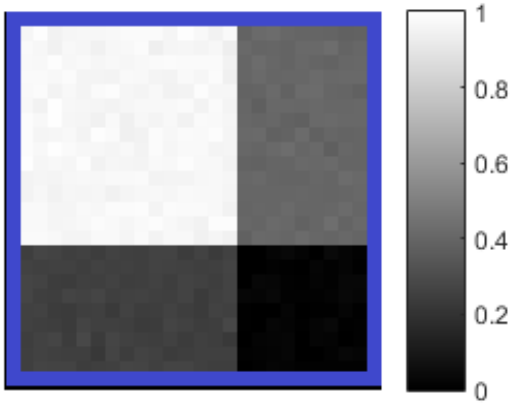

(b) Selected region

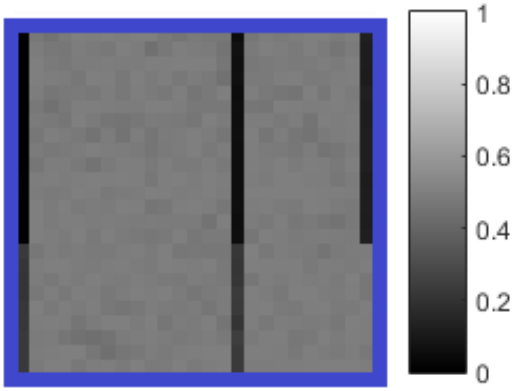

(c) Horizontal mIGMRF parameters (b^x)

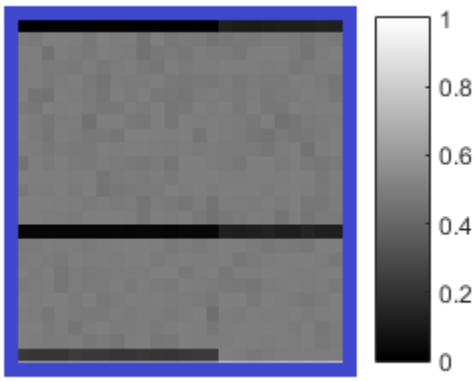

(d) Vertical mIGMRF parameters (b^y)

Figure 3.3: An illustration for mIGMRF prior parameters for Ammonioalunite abundance map.

tal and vertical direction are shown in Figure (c) and (d), respectively. One can observe that IGMRF parameters for edge region have smaller values and for the smooth region they take comparatively larger values.

3.3 Estimation of final abundance maps using mIGMRF

Using terms given in Eq. (3.3) and Eq. (3.4), the final energy function to be minimized for abundance estimation is given by,

$$\begin{aligned} E(\boldsymbol{\alpha}) = & \sum_{(x,y)} \|\boldsymbol{r}(x,y) - \boldsymbol{M}\boldsymbol{\alpha}(x,y)\|^2 + \\ & \sum_{(x,y)} \sum_{p} b^{x}_{(x,y,p)} (\alpha(x-1,y,p) - \alpha(x,y,p))^2 \\ & + b^{y}_{(x,y,p)} (\alpha(x,y-1,p) - \alpha(x,y,p))^2. \end{aligned} \tag{3.7}$$

Here, b^x and b^y are estimated using Eq. (3.6). See that Eq. (3.7) results in a convex function and hence can be minimized by using gradient-descent optimization method. To carry out the optimization, we use Adam optimizer [87] that computes the adaptive learning rates from the estimates of first and second moments of the gradients of energy function w.r.t. abundances. Once the abundances are estimated, we iterate on the following two steps until convergence in order to get the final abundance maps.

Step 1: Compute b^x and b^y parameters using Eq. (3.6) by keeping $\boldsymbol{\alpha}$ fixed.

Step 2: Optimize Eq. (3.7) for $\boldsymbol{\alpha}$ by keeping the b^x and b^y fixed.

3.4 Experimental results

We first conduct the experiment on synthetic HSIs generated using three spectral signatures of the U.S. Geological Survey (USGS) digital spectral library [89]. Next, we show the experiments on the two real data sets consisting of Urban data captured by Hyper-spectral Digital Imagery Collection Experiment (HYDIC) [90] and Cuprite data collected by the Airborne Visible/Infrared Imaging Spectrometer (AVIRIS) [91] used in the hyperspectral unmixing [92]. In all our experiments, the IGMRF parameters were initialized by computing them with the use of initial estimate of abundances obtained using the method of FCLS [58]. The comparison between the true and the estimate of abundances is done using the root mean-squared error (RMSE) [93], abundance angle mapper (AAM) [94] and the

abundance information divergence (AID) [95] as the quantitative measures. The ideal value for each of these quantitative measures is zero. Here, the AAM and AID measure the accuracy of the estimate in terms of spectral content whereas the RMSE gives the magnitude of error between the true and the estimated abundances.

3.4.1 Experiment on synthetic data

The synthetic HSIs are generated by using the linear mixing of the spectral signatures of three materials, namely: Ammonioalunite NMNH145596, Brucite HS247.3B, and Andradite WS487 which are available in the USGS library [89]. The spectral signatures of 224 contiguous bands are recorded and these are in the spectral range of $400 - 2500nm$. With this, the size of the endmember matrix $\mathbf{M}$ becomes 224×3, in which every column represents a different material. The reflectance vector $\boldsymbol{r}$ of size 224×1 is constructed as $\boldsymbol{r} = \mathbf{M}\boldsymbol{\alpha}$ where $\boldsymbol{\alpha}$ is the abundance vector of size 3×1. Choosing different $\boldsymbol{\alpha}$ vectors at 75×75 locations, image cube of the size $75 \times 75 \times 224$ is generated by multiplying $\mathbf{M}$ and $\boldsymbol{\alpha}$ vectors. The ground truth abundance maps are shown in Figure 3.4 (a). One can see that each synthetically generated abundance map has 9 square regions, wherein one of the diagonal square regions in the maps consists of abundance values close to 1 with the center pixel having a value of 1. In order to to satisfy sum to one constraint, other two diagonal square regions have values closer to 0 with the value at the center exactly equal to 0. Here, off-diagonal square regions have abundance values with different mean values in every square region leading to edge between two square regions. Note that, the abundance maps displayed in Figure 3.4 have both the homogeneous and heterogeneous abundance values. The synthetic HSI is generated by using these abundance maps in the LMM.

The experiments are performed at different signal-to-ratio (SNR) levels. In order to generate noisy data, we add IID Gaussian noise to synthetically generated pure data. To obtain specific SNR data, we calculate the required noise variance based on the signal variance and then add noise to pure data. For example, for 10 dB SNR, we fix the noise variance as 0.10 times of signal variance. The estimated

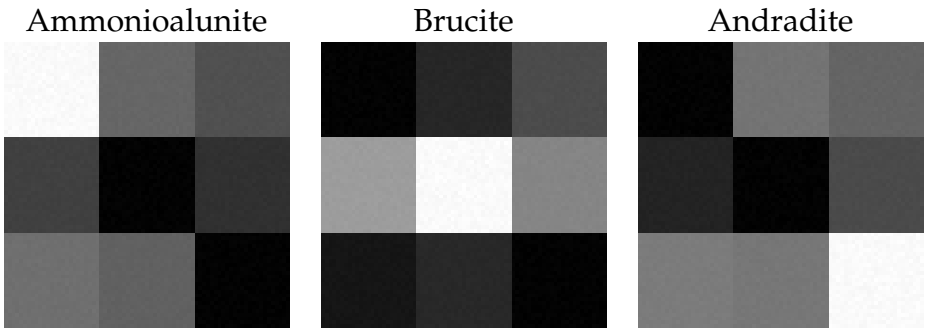

(a) Ground truth

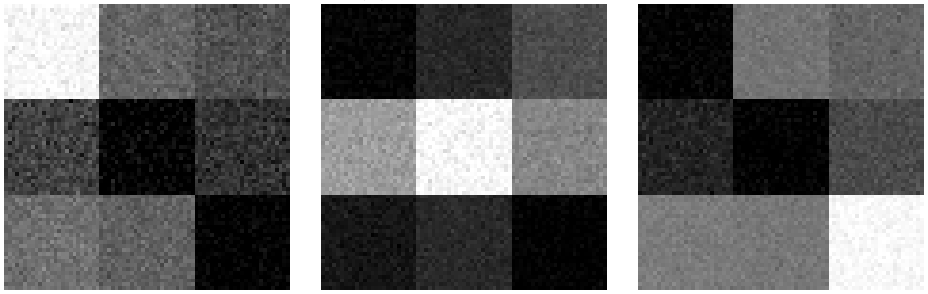

(b) FCLS [58]

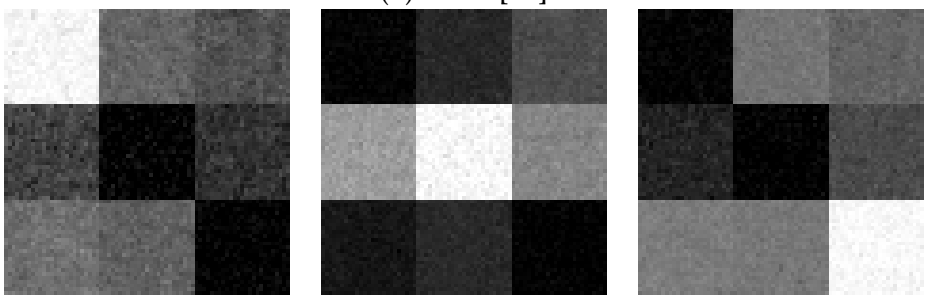

(c) Proposed [96]

Figure 3.4: Ground truth and estimated abundance maps for synthetically generated data for 5 dB SNR.

abundance maps using FCLS as well as the proposed are shown in Figure 3.4 (b) and (c), respectively, for 5 dB SNR. Looking at Figure 3.4, we observe that the homogeneous region in abundance maps estimated using the proposed approach appear smoother when compared to the FCLS. At the same time, our method better preserves the discontinuities among the abundances as evident at the borders of the abundance patterns. The quantitative comparison using three different measures for synthetic data is shown in Table 3.1. One can see that from Table 3.1, our results are better when compared to other approaches.

Table 3.1: Quantitative comparison on synthetic data.

Measure	Algorithm	SNR = 25dB	SNR = 20dB	SNR = 15dB	SNR = 10dB	SNR = 5dB
RMSE [93]	FCLS [58]	0.0079	0.0067	0.0114	0.0194	0.0343
	DGAE [82]	0.0941	0.0071	0.0140	0.0369	0.1198
	cSUnSAL [97]	0.0079	0.0067	0.0114	0.0194	0.0343
	Proposed [96]	**0.0070**	**0.0063**	**0.0095**	**0.0157**	**0.0276**
AAM [94]	FCLS [58]	0.0155	0.0126	0.0216	0.0370	0.0652
	DGAE [82]	0.1898	0.0134	0.0261	0.0647	0.2236
	cSUnSAL [97]	0.0155	0.0126	0.0216	0.0370	0.0652
	Proposed [96]	**0.0134**	**0.0115**	**0.0179**	**0.0297**	**0.0522**
AID [95]	FCLS [58]	0.0214	0.0224	0.0431	0.0729	0.1116
	DGAE [82]	1.3089	0.0392	0.0926	0.1798	2.4968
	cSUnSAL [97]	0.0215	0.0223	0.0431	0.0729	0.1116
	Proposed [96]	**0.0060**	**0.0058**	**0.0135**	**0.0305**	**0.0555**

3.4.2 Experiments on Urban data

In this experiment, we use real data of the Urban area at Copperas Cove, TX, US recorded by HYDICE [90]. This HSI data has a size of 307×307 pixels where each pixel covers $2m \times 2m$ area and there are 210 bands which are in spectral range of $400 - 2500nm$ with a spectral resolution of $10nm$. The bands $1 - 4, 76, 87, 101 - 111, 136 - 153$ and $198 - 210$ represent the atmospheric distortion and water absorption. Hence, we remove these bands and perform the experiments on the remaining 162 bands only. Our data consists of four endmembers, namely: Asphalt, Grass, Tree, and Roof. We obtain the ground truth abundance by using the steps given in [98]. The estimated abundance maps for Urban data are shown in the Figure 3.5, where we observe that the abundance patterns estimated using the proposed approach are closer to the ground truth when compared to the FCLS approach. As given in Table 3.2, the results for the proposed approach are better when compared to the other state-of-the-art methods.

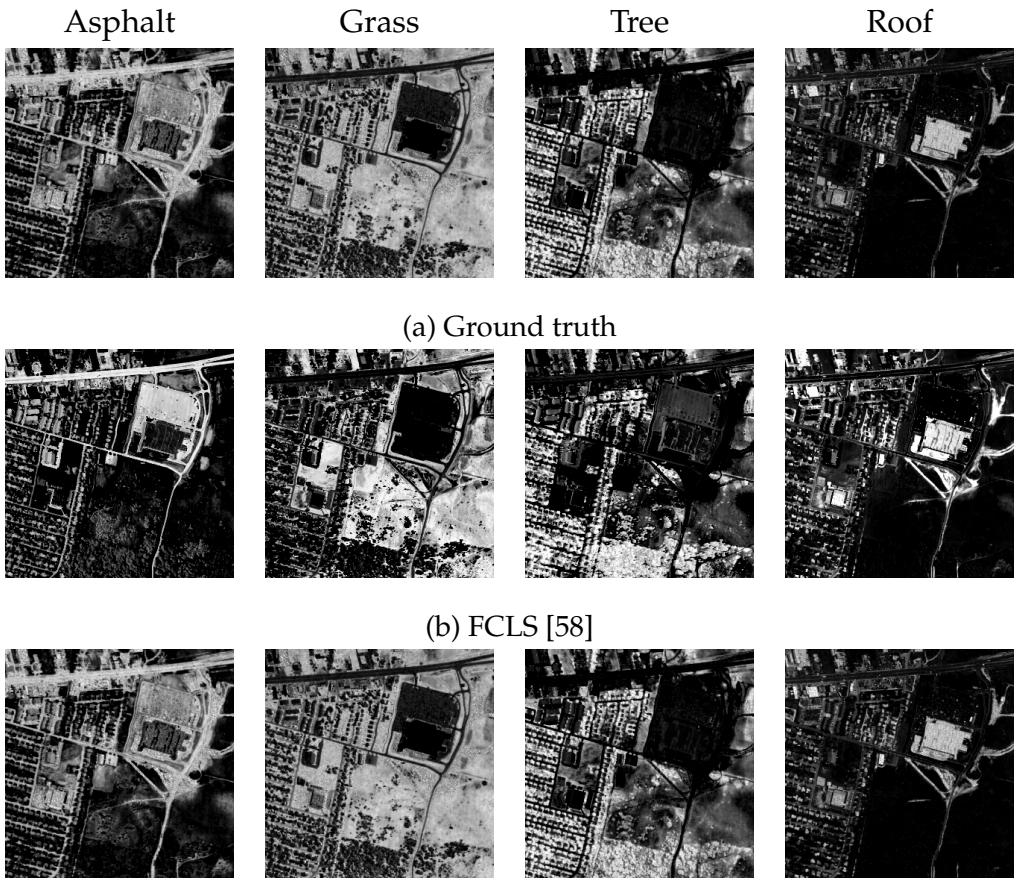

(a) Ground truth

(b) FCLS [58]

(c) Proposed [96]

Figure 3.5: Ground truth and estimated abundance maps for URBAN hyperspectral data.

Table 3.2: Quantitative comparison on Urban data acquired by HYDICE.

Algorithm	Measure		
	RMSE [93]	AAM [94]	AID [95]
FCLS [58]	0.0025	0.0057	0.0357
DGAE [82]	0.0025	0.0057	0.0356
cSUnSAL [97]	0.0025	0.0057	0.0363
Proposed [96]	**0.0022**	**0.0045**	**0.0414**

3.4.3 Experiments on Cuprite data

We conducted another experiment on real HSI data acquired by the AVIRIS sensor over the Cuprite mining site, USA. The acquired image consists of 224 bands with a spectral range $400 - 2500nm$ having the spectral resolution of $10nm$ and each pixel covers an area of $20m \times 20m$. For this experiment, we used sub-images of the size 250×190 pixels located towards the east-south centre of the scene. As in the previous experiment, here also we retain only 188 bands after removing the noisy bands $1, 2, 104 - 113, 148 - 167$, and $221 - 224$ which represent the atmospheric distortion and water absorption.

We first determine the endmembers for this HSI data and then perform abundance estimation. In this experiment, we used the VCA algorithm proposed in [44] to extract endmembers present in the data. As given in [44], there are 14 endmembers present in this Cuprite data. We then construct the endmember matrix using the extracted endmembers and then apply our proposed approach to find abundance maps. Note that in this case, the true abundances are not available. Hence, we use the data reconstruction error (DRE) as a measure which calculates the RMSE between the available and the reconstructed reflectance reconstructed using the estimated abundance map. The ideal value of DRE is zero. Here, experiments for each method are performed ten times, and with that the mean and standard deviation of the DRE values are shown in Table 3.3. The estimated abundances using the proposed approach are shown in Figure 3.6. As illustrated in Table 3.3, the results for the proposed approach are better than other state-of-the-art methods.

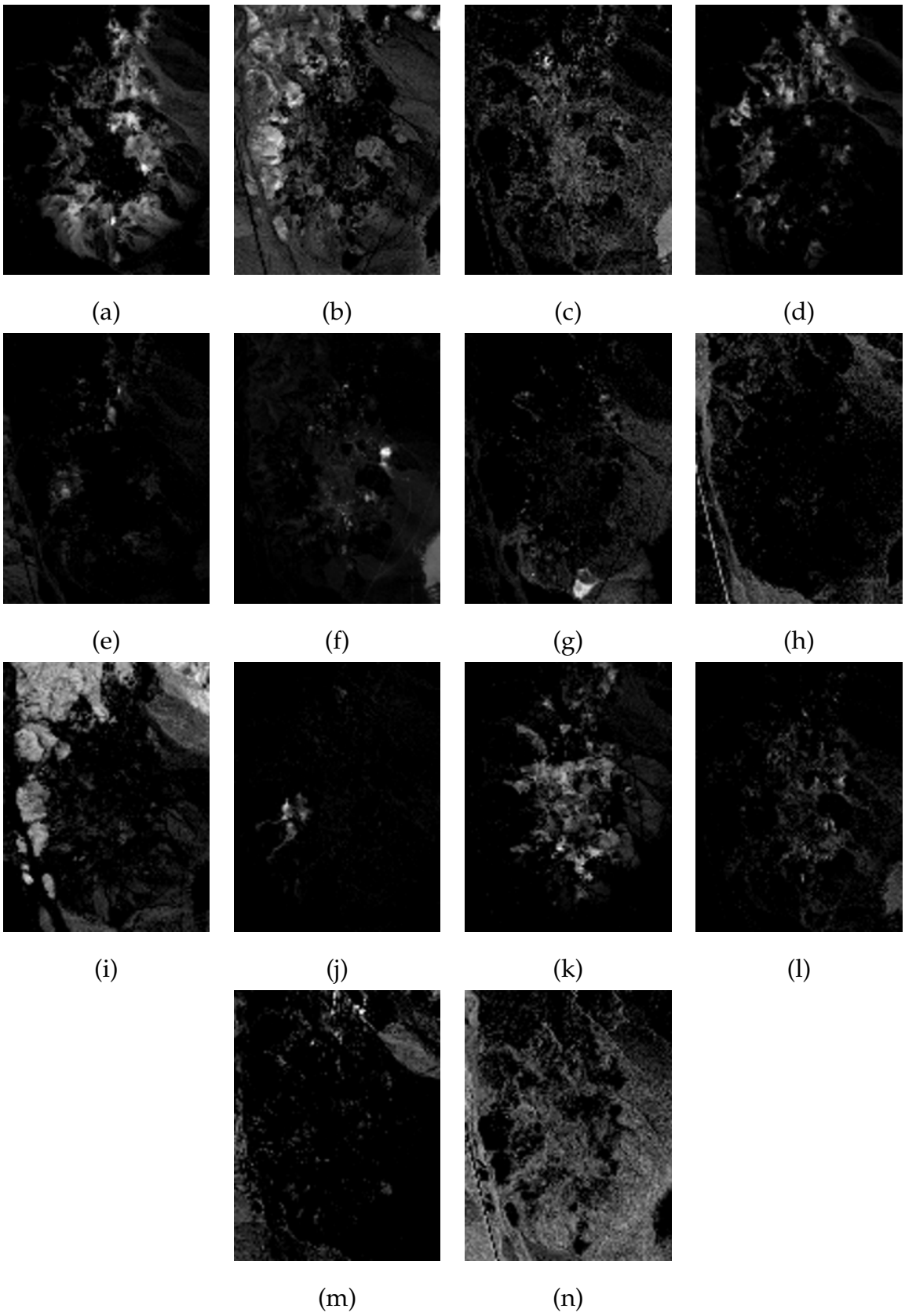

Figure 3.6: Estimated abundance maps for AVIRIS Cuprite data using the proposed approach. (a) Alunite (b) Pyrope #1 (c) Nontronite (d) Dumortierite (e) Kaolinite (f) Muscovite (g) Kaolinite #3 (h) Andradite #1 (i) Sphene (j) Buddingtonite (k) Chalcedony (l) Montmorillonite (m) Pyrope #2, and (n) Desert vanish.

Table 3.3: Quantitative comparison on Cuprite data acquired by AVIRIS.

Algorithm	DRE	
	mean	standard deviation
FCLS [58]	0.0041	0.0049
DGAE [82]	0.0046	0.0055
cSUnSAL [97]	0.0042	0.0051
Proposed [96]	**0.0039**	**0.0043**

3.5 Conclusion

In this chapter, we have proposed a novel approach to estimate abundance maps by energy minimization framework. A new discontinuity preserving prior is proposed by modifying the expression for IGMRF parameters. A two-step iterative algorithm is used to refine the abundance maps as well as the prior parameters. The experiments are conducted on synthetic and the real HSIs show that our method performs better when compared to other state-of-the-art approaches including at low SNR in the data.

Abundance maps have spatial redundancy and it can be captured using sparsity induced prior. Since the IGMRF parameters are computed using the initial estimate of abundances, their accuracy depends on the initial estimate and the noise in the data. Use of additional sparseness prior can gives a better solution under such a scenario. Hence, in the next chapter, we construct sparsity induced prior along with the modified IGMRF prior in order to better the estimate of abundances.

CHAPTER 4

Abundance Estimation using Discontinuity Preserving and Sparsity-induced Priors

In chapter 3, we discussed that the abundance maps have homogeneous regions with limited discontinuity, and they exhibit spatial redundancy. Inhomogeneous Gaussian Markov random field (IGMRF) prior captures the smoothness and preserves discontinuities among abundance values as shown in chapter 3. In this chapter, we address the spatial redundancy present in the abundances using sparsity induced prior. Many of the algorithms proposed for the abundance estimation are based on the least squares [58, 99, 100], geometry-based [82], and some are derived from sparse regression [97] methods. However, the solution is sensitive to noisy data and sudden variations in the unmixing components. The problem of abundance estimation is severely ill-posed in the presence of noise and outliers, and hence use of regularization helps in making it better posed [83].

Recently, few researchers have incorporated the spatial information using the sparse unmixing approach in order to improve the accuracy of estimated abundances [63–65]. Sparse unmixing obtains abundance maps by using the dictionary of endmember spectra (spectral library). Since the number of spectral signatures in a scene is much smaller than the total number of the signatures available in the spectral library, it provides a convenient approach for estimating abundances by the sparse representation. The authors in [63–65], use sparse regression for abundance estimation where the problem is formulated as : given hyperspectral image (HSI) data and the spectral library, the objective is to obtain the abundances by using the sparse representation of abundances. In [101], abundances are esti-

mated by incorporating endmember variability and their spatial information in order to reduce the error caused due to endmember variability. Considering that the abundances are spatially smooth, the authors in [102], use Markov random field (MRF) based prior to incorporate the smoothness in their framework. The MRF is also used for joint HSI unmixing and classification where simulated annealing optimization is employed to solve the problem [103]. Nonlinear mixing models (NLMM) are also introduced to address the nonlinearity in the data [104]. In [105, 106], a NLMM is proposed where the given HSI data is modelled using LMM with the additional nonlinearity terms. In [105], Potts MRF is used to detect the nonlinearity based on spatial regularity of nonlinear terms. Here, the HSI images are segmented into regions having similar statistical properties. Instead of Potts MRF, Gamma MRF is employed in [106] to model the joint distribution of the nonlinear terms. We know that, homogeneous MRF considers few global parameters only, thus making the solution too smooth which is not desirable. Since the abundance maps have homogeneous as well as non-homogeneous regions and their values vary locally, it is better to consider prior that adaptively takes care of variations in abundance values. To this end, as already mentioned use of IGMRF prior is better suited to capture the smoothness and also to preserve the discontinuities among the abundances as used in [84].

In practice, abundance maps have homogeneous regions with limited discontinuities, leading to global redundancy. Because of this, one can represent the abundance in a domain in which they are sparse. Though, the mIGMRF prior as developed in [96] captures the smoothness in addition to discontinuities, it does not account for global characteristic such as the sparseness present in the abundance maps. This motivates us to use an additional prior in addition to the mIGMRF prior (chapter 3) to incorporate the sparseness constraint. The sparse representation of an entity can be obtained by using a fixed or overcomplete learned dictionary. The overcomplete learned dictionary is adaptive to data which gives more precise sparse representation [107, 108]. Hence, in this chapter, we make use of the overcomplete learned dictionary for obtaining the sparse representation of abundances from the given (available) observation itself. To this end, we employ the K-

singular value decomposition (K-SVD) algorithm to learn the overcomplete dictionary since it has been proven effective in many image processing applications [28].

In what follows, we briefly compare the proposed approach with other competitive approaches. Authors in [63–65], use spatial regularization with sparse unmixing that make use of the entire spectral library to obtain the abundances. Note that, one needs the entire spectral library to estimate the abundances and these approaches do not make use of sparseness prior as used in our approach. Our method uses the already available endmembers (note that the endmembers are assumed to be known or their estimated values are available) and the sparsity-induced prior to captures the global dependencies inherent in abundance maps. It results in a better estimate of abundances under the noisy scenario. Besides, the proposed approach do not require the spectral library as used in [63–65]. Note that, though approaches in [64, 65], use the edge preserving priors, they do not consider the spatial adaptive prior mIGMRF as used in this chapter. In [105], MRF is used to model nonlinearity where the images representing the nonlinearity are divided in small regions. The approach is improved in [106], where Gamma MRF is used to model the nonlinearity that accounts for nonlinearity at every pixel location. Although, both [105] and [106] consider nonlinear model, they need to use the Markov Chain Monte Carlo (MCMC) method to solve the problem which is computationally expensive. When compared to these approaches, our proposed energy minimization framework, in this chapter, takes care of the local and the global dependencies present in the abundance maps. Also, the minimization is carried out by using a simple gradient based optimization technique.

In this chapter, we propose a two-phase iterative algorithm for abundance estimation. In phase one, we compute mIGMRF parameters of abundances estimated at each pixel location and learn the dictionary as well as the sparse coefficients of abundances using the current estimate of abundance maps. An initial estimate of abundances obtained using the FCLS is employed to start the iteration. In phase two, we minimize the energy function in order to refine abundance values by making use of the mIGMRF parameters, the current dictionary and the sparse co-

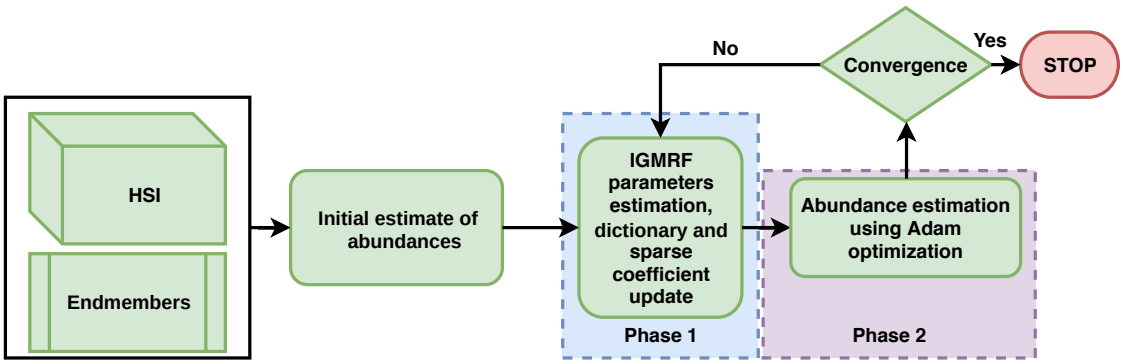

Figure 4.1: Block diagram of abundance estimation using discontinuity preserving and sparsity-induced priors.

efficients that are obtained in phase one. The two phases are iterated to refine the results until the convergence. Here, we consider the convergence in mean-squared error rate sense where the data reconstruction error, i.e., the error between the observed reflectance values and the reconstructed reflectance using the estimated unmixed components, is asymptotically constant over the iterations. The block diagram of the proposed approach is shown in Figure 4.1.

4.1 Problem formulation

Objective is to estimate abundance map for a given hyperspectral data and the endmembers. Continuing from chapter 3, we now formulate the problem by minimizing the following energy function,

$$E(\boldsymbol{\alpha}) = E_D(\boldsymbol{\alpha}) + E_P(\boldsymbol{\alpha}), \tag{4.1}$$

where, $E_D(\boldsymbol{\alpha})$ represents the data fitting term measuring the reconstruction error between the given and the reconstructed reflectance. $E_P(\boldsymbol{\alpha})$ represents the prior term performing regularization on abundances.

Using the same linear model, LMM at each location can be given as,

$$\mathbf{r} = \mathbf{M}\boldsymbol{\alpha} + \boldsymbol{\eta}, \tag{4.2}$$

As before, the abundance follows non-negativity and sum-to-one constraints. It is clear that number of abundance maps is the same as the number of endmembers p. Using Eq. (4.2), $E_D(\boldsymbol{\alpha})$ for pixel location (x, y) can be written as,

$$E_D(\boldsymbol{\alpha}) = \sum_{(x,y)} \|\mathbf{r}(x, y) - \mathbf{M}\boldsymbol{\alpha}(x, y)\|^2, \tag{4.3}$$

where, $\mathbf{r}(x, y)$ and $\boldsymbol{\alpha}(x, y)$ represent the reflectance and abundance vectors at location (x, y).

In this chapter, the prior term, $E_P(\boldsymbol{\alpha})$ is defined as the sum of mIGMRF and sparsity induced priors, and is given by,

$$E_P(\boldsymbol{\alpha}) := \beta E_{mIGMRF}(\boldsymbol{\alpha}) + \gamma E_{sparse}(\boldsymbol{\alpha}), \tag{4.4}$$

where, E_{mIGMRF} and E_{sparse} represent the mIGMRF (chapter 3) and sparsity prior (will be discussed in section 4.2) terms, respectively. Here, β and γ are the regularization parameters.

As discussed in section 3.2 of chapter 3, $E_{mIGMRF}(\boldsymbol{\alpha})$ is considered as the sum of squares of finite difference approximations to the first order derivatives of abundances at each pixel location (x, y) i.e., considering each of the endmember p in every abundance map we can write,

$$\begin{aligned} E_{mIGMRF}(\boldsymbol{\alpha}) = \sum_{(x,y)} \sum_{p} & b^{x_{mIGMRF}}_{(x,y,p)} (\alpha(x-1, y, p) - \alpha(x, y, p))^2 \\ & + b^{y_{mIGMRF}}_{(x,y,p)} (\alpha(x, y-1, p) - \alpha(x, y, p))^2, \end{aligned} \tag{4.5}$$

where, $b^{x_{mIGMRF}}$ and $b^{y_{mIGMRF}}$ are the spatially adaptive IGMRF parameters in horizontal and vertical directions, respectively. We have seen that these parameters can be given by,

$$\begin{aligned} b^{x_{mIGMRF}}_{(x,y,p)} &= 1 - \frac{1}{1 + \mathrm{e}^{-5\times|(\alpha_{in}(x-1,y,p) - \alpha_{in}(x,y,p))|}}, \\ b^{y_{mIGMRF}}_{(x,y,p)} &= 1 - \frac{1}{1 + \mathrm{e}^{-5\times|(\alpha_{in}(x,y-1,p) - \alpha_{in}(x,y,p))|}}. \end{aligned} \tag{4.6}$$

4.2 Sparse model for abundances

The mIGMRF prior captures the local characteristics of the abundance maps and helps in preserving smoothness as well as discontinuities. Now, in order to capture the hidden global characteristic, one can represent the abundance maps in a domain where they are sparse and use the sparsity as a prior in addition to the mIGMRF prior. The redundant characteristic of the abundance values can be captured by sparsity induced prior on the $\boldsymbol{\alpha}$. The sparsity induced prior is defined using the learned overcomplete sparseness of overlapping abundance patches. The sparseness within an abundance map is then obtained by averaging the sparseness over these overlapping patches.

Researchers have widely used the learned overcomplete dictionary to obtain the sparse representation of images in various image processing applications. When using the overcomplete dictionary, the number of dictionary atoms (column vectors in the dictionary) is much larger than the input data size. For a fixed number n an image patch of size $\sqrt{n} \times \sqrt{n}$ can be represented as a sparse linear combination of K dictionary atoms where $K >> n$. The representation obtained using a learned overcomplete dictionary is sparser than that obtained when the dictionary entries are fixed. Further, it is adaptive to the training data which is also used in inverse problems such as denoising [107] and restoration [108]. In this chapter, we use the K-SVD algorithm for learning the overcomplete dictionary which has been in use [107]. The K-SVD also takes care of the noise present in the initial estimate of abundance maps while learning the dictionary [28]. We generate overlapping patches of initial abundance maps which are then used for training our dictionary using the K-SVD.

To start with, we extract the $\boldsymbol{\alpha}_{x,y,p} \in \mathbb{R}^{n\times 1}$ abundance patch vector (vectorized version of abundance patch with the size of $n = \sqrt{n} \times \sqrt{n}$) at every location (x, y) in an abundance map for each of the endmembers p. The overcomplete dictionary $\mathbf{D}^p \in \mathbb{R}^{n\times K}$ for each of the endmembers p and the sparse vector $\boldsymbol{\mu}_{x,y,p} \in \mathbb{R}^{K\times 1}$ for each patch at every location (x, y) of each abundance map is learned by the

following objective function using the K-SVD algorithm as,

$$\begin{aligned} \underset{\mathbf{D}^p,\{\boldsymbol{\mu}_{x,y,p}\}}{\arg\min} \quad & \sum_p \sum_{(x,y)} \|\boldsymbol{\alpha}_{x,y,p} - \mathbf{D}^p \boldsymbol{\mu}_{x,y,p}\|_2^2, \\ \text{subject to} \quad & \|\boldsymbol{\mu}_{(x,y,p)}\|_0 \leq T, \forall (x,y). \end{aligned} \tag{4.7}$$

Here, T is the maximum number of non zero entries in $\boldsymbol{\mu}$ i.e., sparseness, in sparse vector at the (x, y). We know that $\|.\|_0$ represents the L_0 norm that enforces sparsity over the abundance patches within an abundance map. K-SVD algorithm works in two iterative steps. In the first step, the dictionary atoms are updated to better fit the data and in the second step, sparse representation is obtained for the updated dictionary.

The abundances can be recovered from the learned dictionary D and the sparse vectors $\boldsymbol{\mu}$ once they are obtained. Thus, one can introduce the sparsity prior $E_{sparse}(\boldsymbol{\alpha})$ in the minimization framework as,

$$E_{sparse}(\boldsymbol{\alpha}) = \sum_p \sum_{(x,y)} \|\boldsymbol{\alpha}_{x,y,p} - \mathbf{D}^p \boldsymbol{\mu}_{x,y,p}\|_2^2. \tag{4.8}$$

4.3 Estimation of final abundance maps

Once again, we estimate the abundance maps by using energy minimization framework that has data and prior terms. As given in Eq. (4.3), we use data reconstruction error by considering LMM. The prior term is formed by adding the mIGMRF and sparsity priors using Eq. (4.5), and Eq. (4.8), respectively. The final energy function to be minimized can be written as,

$$\begin{aligned} E(\boldsymbol{\alpha}) = & \sum_{(x,y)} \|\mathbf{r}(x,y) - \mathbf{M}\boldsymbol{\alpha}(x,y)\|^2 + \\ & \beta \sum_p \sum_{(x,y)} \left\{ b^{x_{mIGMRF}}_{(x,y,p)} \left\{ (\boldsymbol{\alpha}(x-1,y,p) - \boldsymbol{\alpha}(x,y,p))^2 \right\} + \right. \\ & \qquad \left. b^{y_{mIGMRF}}_{(x,y,p)} \left\{ (\boldsymbol{\alpha}(x,y-1,p) - \boldsymbol{\alpha}(x,y,p))^2 \right\} \right\} + \\ & \gamma \sum_p \sum_{(x,y)} \|\boldsymbol{\alpha}_{x,y,p} - \mathbf{D}^p \boldsymbol{\mu}_{x,y,p}\|_2^2. \end{aligned} \tag{4.9}$$

The energy function given in Eq. (4.9) is convex and hence can be minimized by using the gradient-descent optimization approach. Once again the minimization is carried out by using the Adam optimizer [87] that uses the adaptive learning rates. We use a similar approach as given in FCLS [58] to impose the sum-to-one constraint. The non-negativity constraint is incorporated by considering only the positive values of abundances while updating them. We use FCLS [58] to obtain the initial estimates of abundance maps. However, one may use any other suitable abundance estimation method in order to get the initial abundances. Once the initial values of abundances are known, we iterate on following two steps until the convergence in order to get the final abundance maps:

Phase 1: Keep $\boldsymbol{\alpha}$ fixed, learn the dictionary $\mathbf{D}$ and the set of sparse vectors $\boldsymbol{\mu}$ by using K-SVD algorithm. Compute $b^{x}{}_{mIGMRF}$ and $b^{y}{}_{mIGMRF}$ parameters using Eq. (3.6), at each pixel location for every endmember.

Phase 2: Optimize the Eq. (4.9) for $\boldsymbol{\alpha}$ using Adam optimizer keeping $\mathbf{D}$, $\boldsymbol{\mu}$, $b^{x}{}_{mIGMRF}$ and $b^{y}{}_{mIGMRF}$ fixed as obtained in the phase 1.

Here, we consider the convergence in the mean-squared error (MSE) sense [73]. We resort to a normalized MSE difference between iterations $i-1$ and i given by,

$$\begin{aligned} \delta = \Delta MSE^{i} =& \frac{MSE^{i-1}(\hat{\mathbf{r}}_{i-1}) - MSE^{i}(\hat{\mathbf{r}}_{i})}{MSE^{i-1}(\hat{\mathbf{r}}_{i-1})}, \\ \text{where, } MSE^{i}(\hat{\mathbf{r}}_{i}) &= \left(\mathbf{r_i} - \mathbf{M}\hat{\boldsymbol{\alpha}}_{i}\right)^{T} . \left(\mathbf{r_i} - \mathbf{M}\hat{\boldsymbol{\alpha}}_{i}\right), \forall i., \end{aligned} \tag{4.10}$$

Here, $\mathbf{r_i}$, $\hat{\mathbf{r}}_{\mathbf{i}}$ and $\hat{\boldsymbol{\alpha}}_{i}$ represent the available reflectance, the reconstructed reflectance, and the estimated abundance vectors, respectively. Note that, as the number of iterations i are increased, δ reduces to a very small value and we stop the algorithm when it becomes asymptotically constant.

4.4 Experimentations

In this section, we present experimental results to demonstrate the efficacy of the proposed two-phase energy minimization approach for abundance estimation. In all, we conduct four experiments to validate the proposed approach. We first

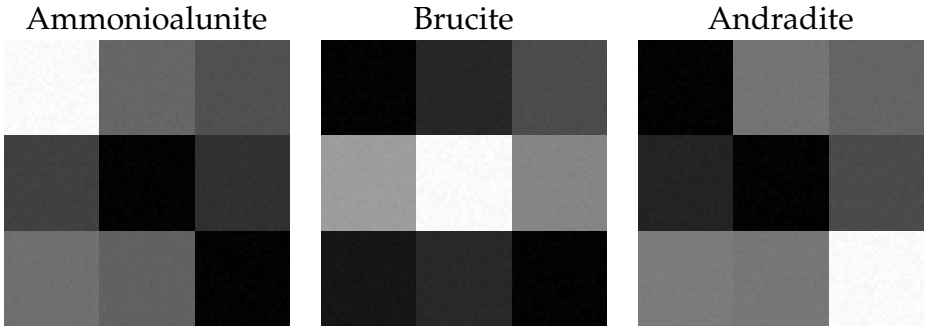

Figure 4.2: Ground truth abundance maps for synthetically generated data 1.

conduct experiments on two sets of synthetic HSIs generated using the spectral signatures of the U.S. Geological Survey (USGS) digital spectral library [89]. We next show an experiment on the Urban real data set captured by Hyperspectral Digital Imagery Collection Experiment (HYDICE) [90], where the true endmembers are available. In our final experiment, we extract endmembers of Cuprite data collected by the Airborne Visible/Infrared Imaging Spectrometer (AVIRIS) [91] using VCA [44] and then estimate the abundance maps for these extracted endmembers. We use FCLS [58] to obtain our initial estimate of abundances for finding the initial mIGMRF parameters and to get the sparse representation and then perform iterations in phase 1 and phase 2 until the convergence. We use the root mean-squared error (RMSE) [93], abundance angle mapper (AAM) [94] and the abundance information divergence (AID) [95] as the quantitative measures. The ideal value for each of these quantitative measures is zero.

4.4.1 Experiments on synthetic data 1

As done in chapter 3, our first experiment on synthetic data uses the same data generated by using the linear mixing of spectral signature recorded using 224 bands of the USGS library [109]. Here, the size of each synthetic HSI is 75×75 pixels which consist of three materials, namely: Ammonioalunite NMNH145596, Brucite HS247.3B, and Andradite WS487. The ground truth abundance maps of synthetic HSI are shown in Figure 4.2. These abundance maps have both the homogeneous and heterogeneous abundance values.

In this experiment, we choose the size of the dictionary as 81×256 that makes

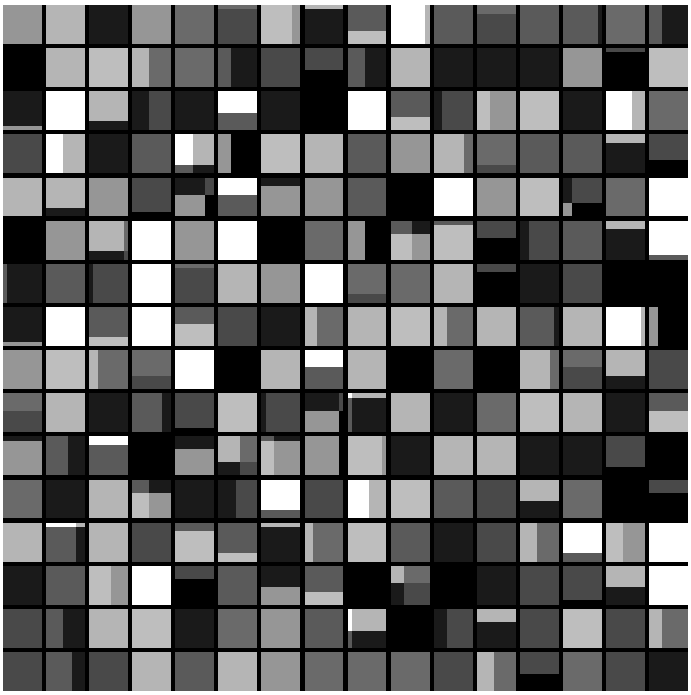

Figure 4.3: Learned dictionary from synthetic data 1.

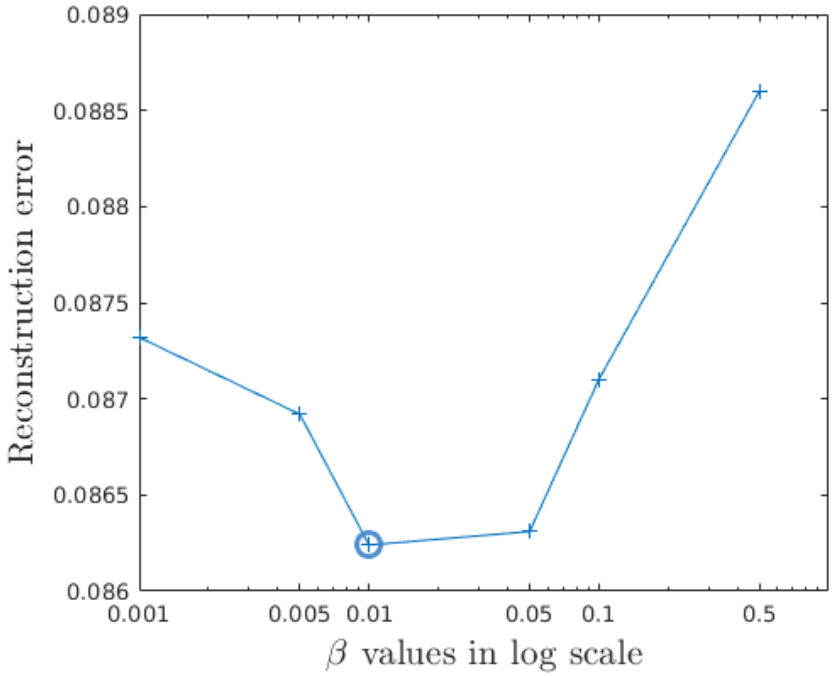

Figure 4.4: Sensitivity analysis for β.

the size of each abundance patch as 9×9, i.e., we have $n = 81$ and $K = 256$, i.e., patch vector has a size of 81×1 and the sparse vector is of size 256×1. The sparseness T is chosen as 6 in Eq. (4.7). The learned overcomplete dictionary for this synthetic data is shown in Figure 4.3 in which each square region has a size of 9×9 and there are 16 square regions in X and Y directions, respectively, making the total number of squares regions as 256. Note that, such a representation is adaptive to the dataset. To start the two-phase iteration process we initialize the mIGMRF parameters and the sparse coefficients by using the initial estimate of $\boldsymbol{\alpha}$ and iterate between the two phases until the convergence. In order to choose an appropriate value for β we first carryout the sensitivity analysis for β and choose that value of β which gives minimum data reconstruction error i.e., the measured error between the observed reflectance values and the one reconstructed using the estimated abundances. This value of β is used in all the other experiments while minimizing the energy function. To perform the sensitivity analysis on β, we generate synthetic data 1 at SNR of 5dB, minimize Eq. (4.9) by varying the γ exponentially from 10^{-4} to 10^{-1} until the convergence. This is repeated for different β values and the final value of β is decided (for all experiments) based on data reconstruction error (DRE) in MSE sense. As shown in Figure 4.4, one can see that $\beta = 0.01$ gives the least DRE. Hence, the β is chosen as 0.01 and γ varies from 10^{-4} to 10^{-1} in all our experiments.

Now, to test the performance, we consider different signal-to-noise ratios (SNR) in the data and conduct the experiment. The reflectance values are obtained using the LMM model and adding noise with different variance i.e., by using $r = \mathbf{M}\boldsymbol{\alpha} + \boldsymbol{\eta}$.

The proposed approach is compared with the following state-of-the-art approaches: FCLS [58], distance geometry-based abundance estimation (DGAE) [82], constrained sparse unmixing by variable splitting and augmented Lagrangian (cSUnSAL) [97], maximum entropy (MaxEnt) [59], simplex-projection unmixing (SPU) [60], FCLS with the total variation regularizer (TV) (FCLS-TV) [111] and our previous approach based on the mIGMRF prior [96] discussed in chapter 3. FCLS-TV [111] uses the total variation regularizer to impose smoothness on abun-

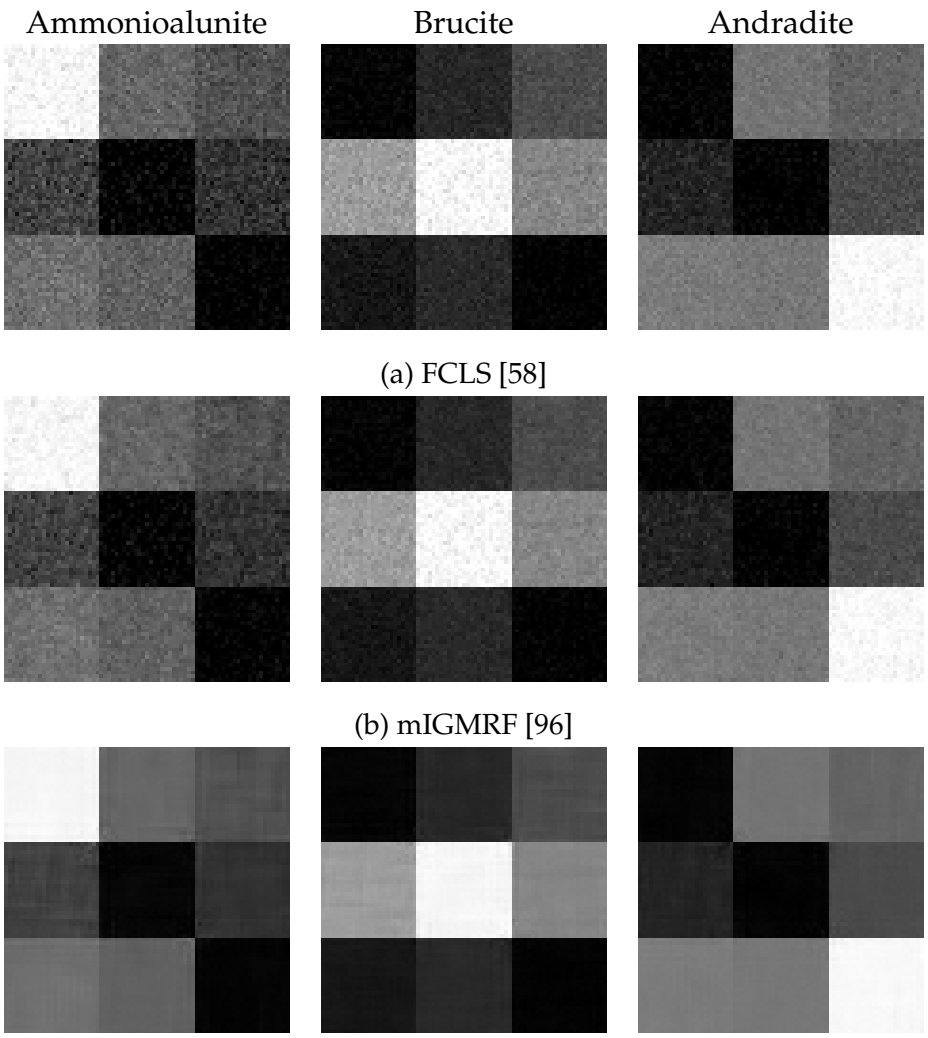

(a) FCLS [58]

(b) mIGMRF [96]

(c) Proposed [110]

Figure 4.5: Estimated abundance maps for the synthetically generated data 1 at 5dB SNR, using (a) FCLS [58], (b) mIGMRF [96], and (c) Proposed [110].

dance maps. Our approach also performs better when compared to other spatial regularization based approaches i.e., FCLS-TV [111] and mIGMRF [96]. The estimated abundance maps using the FCLS [58], mIGMRF prior [96] and the proposed method are shown in Figure 4.5 for the case where the SNR is small i.e., 5dB in the data. We can see that the estimated abundances using the proposed approach are visually consistent with the ground truth shown in Figure 4.2. From Figure 4.5, one can observe that the homogeneous regions in abundance maps estimated using the proposed approach appear smoother when compared to the other two approaches. At the same time, our method better preserves the discontinuities among the abundances, which is evident from the reconstructed borders

Table 4.1: Quantitative comparison on synthetic data 1.

Measure	Algorithm	SNR = 25dB	SNR = 20dB	SNR = 15dB	SNR = 10dB	SNR = 5dB
RMSE [93]	FCLS [58]	0.0079	0.0067	0.0114	0.0194	0.0343
	DGAE [82]	0.0941	0.0071	0.0140	0.0369	0.1198
	cSUnSAL [97]	0.0079	0.0067	0.0114	0.0194	0.0343
	mIGMRF [96]	0.0070	0.0063	0.0095	0.0157	0.0276
	MaxEnt [59]	0.0219	0.0129	0.0171	0.0244	0.0367
	SPU [60]	0.0079	0.0067	0.0114	0.0194	0.0343
	FCLS-TV [111]	0.0069	0.0065	0.0106	0.0202	0.0380
	Proposed [110]	**0.0058**	**0.0058**	**0.0063**	**0.0079**	**0.0120**
AAM [94]	FCLS [58]	0.0155	0.0126	0.0216	0.0370	0.0652
	DGAE [82]	0.1898	0.0134	0.0261	0.0647	0.2236
	cSUnSAL [97]	0.0155	0.0126	0.0216	0.0370	0.0652
	mIGMRF [96]	0.0134	0.0115	0.0179	0.0297	0.0522
	MaxEnt [59]	0.0414	0.0230	0.0305	0.0443	0.0680
	SPU [60]	0.0155	0.0126	0.0216	0.0370	0.0652
	FCLS-TV [111]	0.0138	0.0123	0.0196	0.0376	0.0715
	Proposed [110]	**0.0105**	**0.0104**	**0.0114**	**0.0137**	**0.0205**
AID [95]	FCLS [58]	0.0214	0.0224	0.0431	0.0729	0.1116
	DGAE [82]	1.3089	0.0392	0.0926	0.1798	2.4968
	cSUnSAL [97]	0.0215	0.0223	0.0431	0.0729	0.1116
	mIGMRF [96]	0.0060	0.0058	0.0135	0.0305	0.0555
	MaxEnt [59]	0.0232	0.0128	0.0169	0.0245	0.0407
	SPU [60]	0.0214	0.0224	0.0431	0.0729	0.1116
	FCLS-TV [111]	0.0052	0.0061	0.0103	0.0192	0.0403
	Proposed [110]	**0.0038**	**0.0039**	**0.0044**	**0.0059**	**0.0101**

of the abundance in the proposed method. The quantitative comparison considering different SNR levels is shown in the Table 4.1. Note that the values indicated in the table represent the average over the entire set of abundance values. From Table 4.1, it is clear that our approach consistently performs better when compared to other methods which do not consider spatial regularization.

In order to demonstrate the performance of our approach in the homogeneous, heterogeneous and edge regions of the abundance maps, we show the plots of pixel locations versus estimated abundance values at those locations. To do this we select small portions (rectangular boxes) of homogeneous and heterogeneous region from the abundance maps of Ammonioalunite, Brucite, and Andradite as shown in Figure 4.6. The homogeneous, heterogeneous and edge regions are represented by GREEN, RED and BLUE colored borders, respectively. Plots of pixel locations versus abundance values for one of the rows in the selected regions of the abundance maps are shown in Figure 4.7. It can be seen from the plots that the abundance values estimated using the proposed approach are closer to the ground truth.

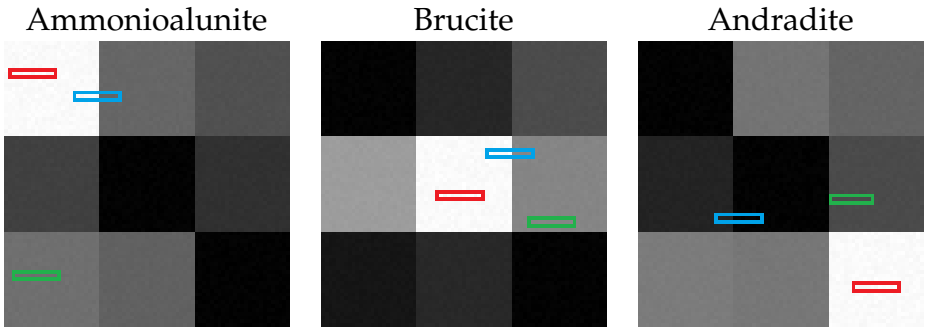

Figure 4.6: Selected homogeneous (GREEN border), heterogeneous (RED border), and edge (BLUE border) regions shown in the abundance maps for synthetically generated data 1. Refer to Figure 4.7. for corresponding plots of estimated abundance values.

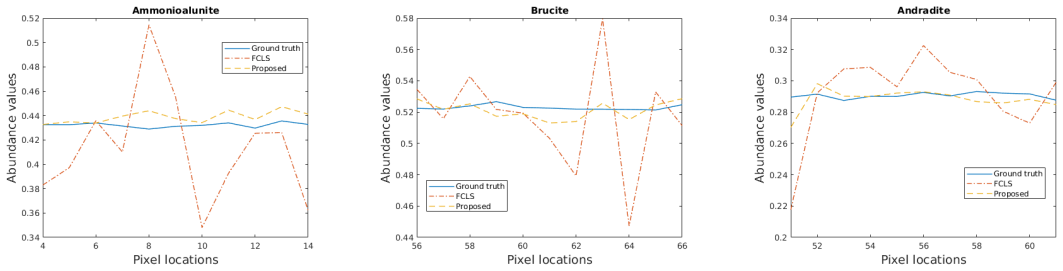

(a) Homogeneous reflectance region referring to Figure 4.6.

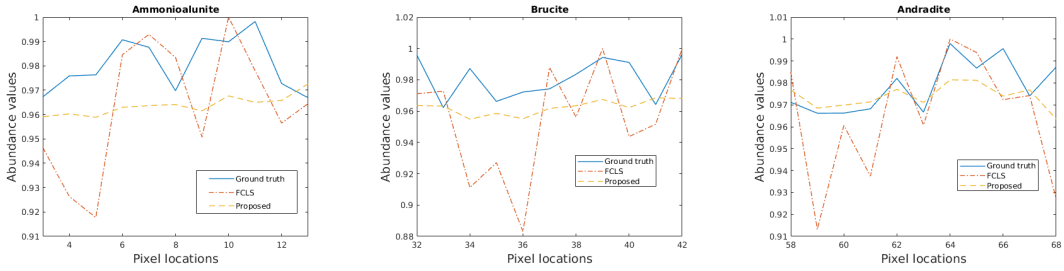

(b) Heterogeneous reflectance region referring to Figure 4.6.

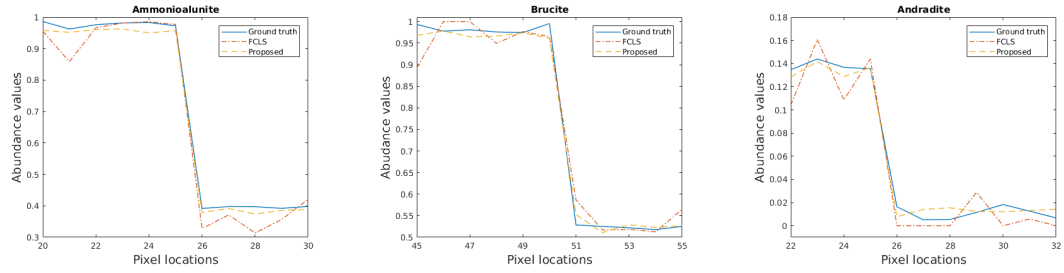

(c) Edge reflectance region referring to Figure 4.6.

Figure 4.7: Pixel locations versus estimated abundances on the selected regions of Figure 4.6 within the synthetic data 1. The plots are shown for Ground truth, estimated abundances using FCLS method [58], and using the proposed approach. (a) Homogeneous reflectance region, (b) Heterogeneous reflectance region, and (c) Edge reflectance region.

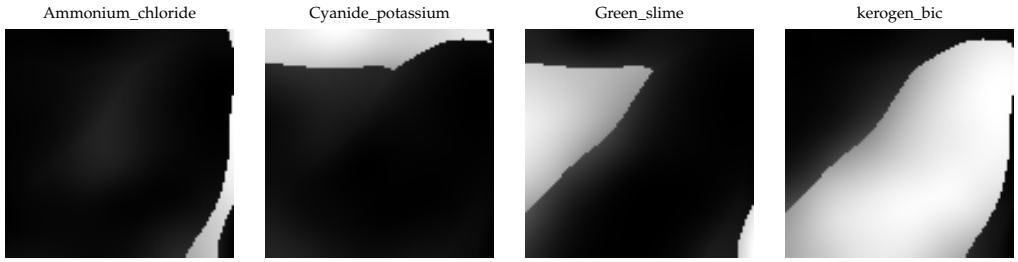

Figure 4.8: Ground truth abundance maps for synthetically generated data 2.

4.4.2 Experiments on synthetic data 2

In this subsection, we discuss the results of another synthetic data 2 generated by using the linear mixing of the spectral signatures of four materials, namely: Ammonium_chloride, Cyanide_potassium, Green_slime, and kerogen_bic selected from USGS spectral library [89]. We use the Hyperspectral Imagery Synthesis tools [112] to generate the HSIs with the above material signatures. In this case, the spectral signatures of 480 contiguous bands are recorded and these are in the spectral range of $400 - 2500nm$. We generate image cube of the size $100 \times 100 \times 480$ using the abundance maps of size $100 \times 100 \times 4$. The ground truth abundance maps are shown in Figure 4.8. These abundance maps are generated using the Gaussian field, and hence they contain both the smooth regions as well as edges with significantly high heterogeneous regions when compared to the synthetic data 1 making the estimation of abundances more challenging.

In order to show the qualitative comparison for this experiment, the estimated abundance maps using the FCLS [58], mIGMRF prior [96] and the proposed method are displayed in Figure 4.9, for the low SNR of 5dB in the data. It can be seen that spatial patterns in the abundance maps estimated using the proposed approach are consistent with the ground truths displayed in Figure 4.8. The quantitative comparison is shown in the Table 4.2 for the different SNR levels. One can clearly see that our approach performs better when compared to the other state-of-the-art approaches.

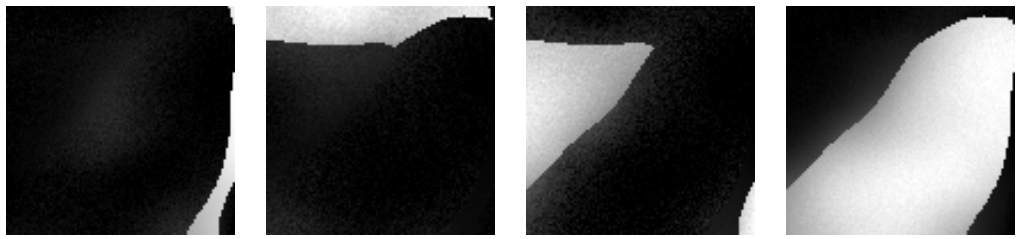

(a) FCLS [58]

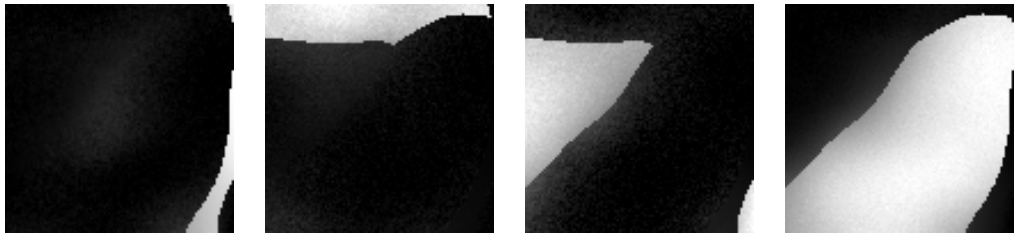

(b) mIGMRF [96]

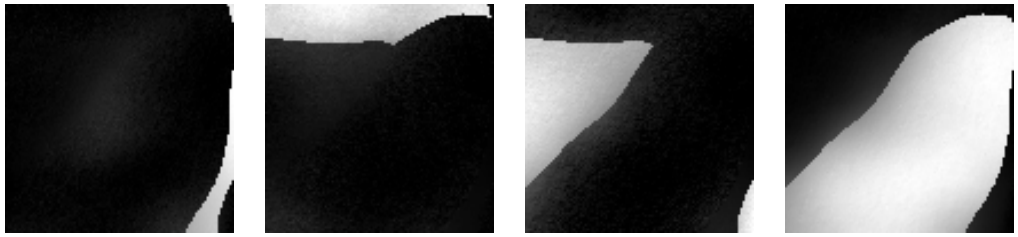

(c) Proposed

Figure 4.9: Estimated abundance maps for synthetically generated data 2 at 5dB SNR using (a) FCLS [58], (b) mIGMRF [96], (c) Proposed.

Finally, before we start explaining the experiments using real data we discuss in brief the computation time of the proposed two-phase iterative approach. All the approaches used in comparison have been implemented in MATLAB15 version installed on Intel i5 processor with 3.20 GHz clock speed, 8-GB memory. In Table 4.3, we display the average computation time to estimate abundances for the synthetic data 1 and 2 using different methods. It can be seen that computation time for the proposed approach is more when compared with the other approaches. Although, this is undesirable, note that the state-of-the-art approaches proposed in [58–60, 82, 97] are non-iterative and are either statistical or geometrical based, making them computationally less expensive. However, our approach requires dictionary learning (which is not considered in [96]) and also it is iterative resulting in slightly higher computational time. But the advantage here is that, our method considers the spatial correlation of abundances at every location

Table 4.2: Quantitative comparison on synthetic data 2.

Measure	Algorithm	SNR = 25dB	SNR = 20dB	SNR = 15dB	SNR = 10dB	SNR = 5dB
RMSE [93]	FCLS [58]	0.0025	0.0043	0.0072	0.0121	0.0193
	DGAE [82]	0.0026	0.0048	0.0098	0.0226	0.0466
	cSUnSAL [97]	0.0025	0.0043	0.0072	0.0121	0.0193
	mIGMRF [96]	0.0022	0.0037	0.0066	0.0112	0.0180
	MaxEnt [59]	0.0040	0.0053	0.0074	0.0120	0.0192
	SPU [60]	0.0025	0.0043	0.0072	0.0121	0.0193
	FCLS-TV [111]	0.0022	0.0039	0.0070	0.0130	0.0228
	Proposed	**0.0020**	**0.0029**	**0.0053**	**0.0090**	**0.0138**
AAM [94]	FCLS [58]	0.0045	0.0078	0.0131	0.0219	0.0350
	DGAE [82]	0.0047	0.0085	0.0166	0.0357	0.0718
	cSUnSAL [97]	0.0045	0.0078	0.0131	0.0219	0.0350
	mIGMRF [96]	0.0040	0.0068	0.0121	0.0204	0.0326
	MaxEnt [59]	0.0075	0.0099	0.0136	0.0209	0.0347
	SPU [60]	0.0045	0.0078	0.0131	0.0219	0.0350
	FCLS-TV [111]	0.0040	0.0071	0.0127	0.0237	0.0424
	Proposed	**0.0032**	**0.0051**	**0.0089**	**0.0154**	**0.0251**
AID [95]	FCLS [58]	0.0078	0.0199	0.0470	0.1098	0.2404
	DGAE [82]	0.0086	0.0246	0.0791	0.3549	1.4439
	cSUnSAL [97]	0.0078	0.0200	0.0470	0.1099	0.2404
	mIGMRF [96]	0.0035	0.0041	0.0095	0.0773	0.0868
	MaxEnt [59]	0.0037	0.0053	0.0078	0.0932	0.0862
	SPU [60]	0.0078	0.0199	0.0470	0.1098	0.2404
	FCLS-TV [111]	0.0018	0.0044	0.0110	0.1138	0.2668
	Proposed	**0.0009**	**0.0021**	**0.0048**	**0.0109**	**0.0217**

Table 4.3: Average computation time.

Algorithm	Computation time (seconds)	
	synthetic data 1	synthetic data 2
FCLS [58]	01.6352	05.0707
DGAE [82]	00.1956	00.2798
cSUnSAL [97]	00.0922	00.1888
mIGMRF [96]	02.7187	04.0489
MaxEnt [59]	38.3950	50.9030
SPU [60]	00.0806	00.2481
FCLS-TV [111]	04.5100	12.6400
Proposed	07.6171	13.8242

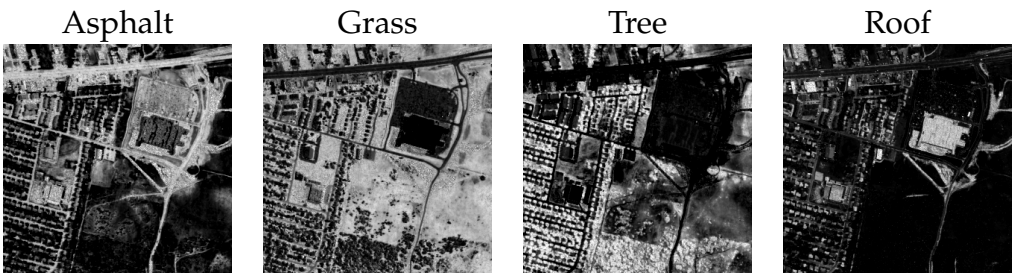

Figure 4.10: Ground truth abundance maps for HYDICE Urban data [98].

in the form of mIGMRF parameters and also use the sparsity present in abundance maps which gives us better results as is evident from Figure 4.5, Figure 4.9, Table 4.1, and 4.2.

4.4.3 Experiments on HYDICE Urban data

We now apply our algorithm on Urban hyperspectral images of HYDIC [90] of size 307×307 pixels having 210 bands with 4 endmembers i.e., Asphalt, Grass, Tree, and Roof. Here, the noisy bands representing the water adsorptions were removed and the experiment was performed on 162 bands only. The ground truth abundance maps for each of the endmembers are shown in Figure 4.10.

Here, we choose the size of a patch as 3×3, i.e., $n = 9$ and $K = 256$ since the data has a low spatial resolution. The estimated abundance maps using different approaches are shown in the Figure 4.11, where we observe that the abundance maps estimated using the proposed approach are visually closer to the ground truth shown in Figure 4.10 as well as consistent with the FCLS [58] and mIGMRF [96] based methods. The quantitative measures for this experiment are shown in Table 4.4. One can see that the results for the proposed approach are superior when compared to other state-of-the-art methods.

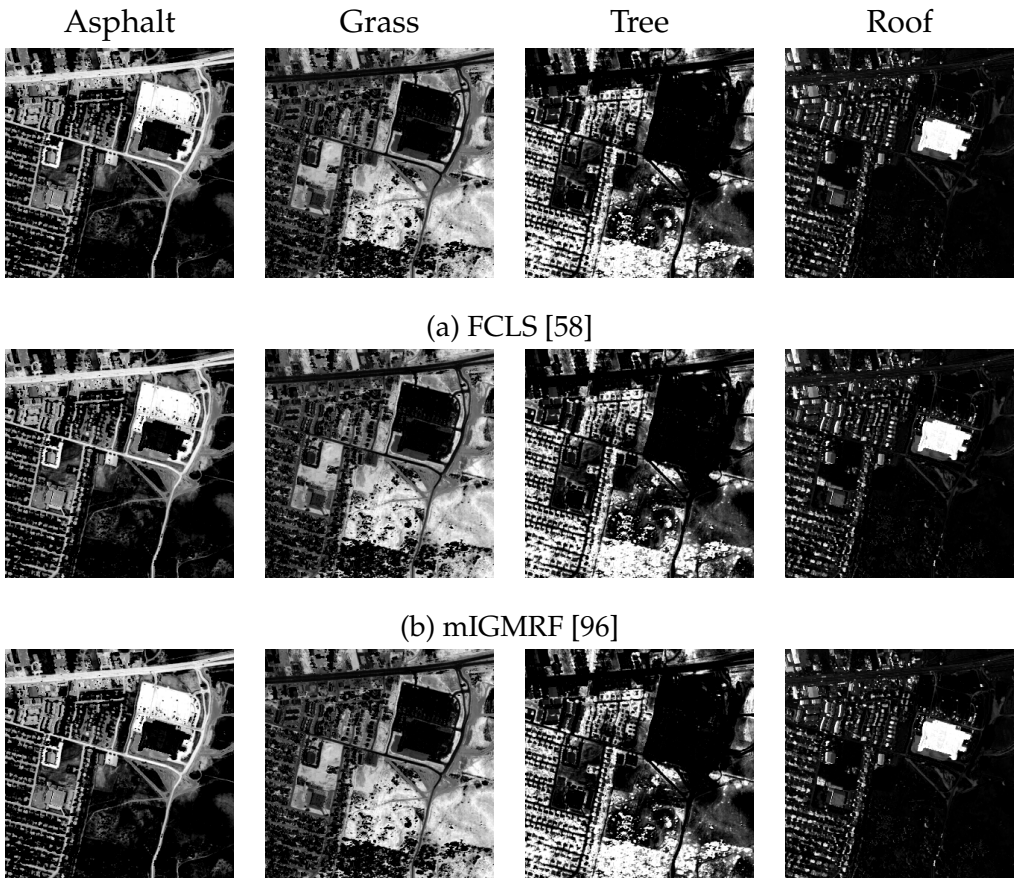

(a) FCLS [58]

(b) mIGMRF [96]

(c) Proposed

Figure 4.11: Estimated abundance maps for HYDICE Urban hyperspectral data using (a) FCLS [58], (b) mIGMRF [96], and (c) Proposed.

Table 4.4: Quantitative comparison on Urban data acquired by HYDICE.

Algorithm	Measure		
	RMSE [93]	AAM [94]	AID [95]
FCLS [58]	0.0025	0.0057	0.0357
DGAE [82]	0.0025	0.0057	0.0356
cSUnSAL [97]	0.0025	0.0057	0.0363
mIGMRF [96]	0.0022	0.0045	0.0414
MaxEnt [59]	0.0288	0.0608	0.9760
SPU [60]	0.0025	0.0057	0.0357
FCLS-TV [111]	0.0023	0.0051	0.0336
Proposed	**0.0018**	**0.0038**	**0.0334**

4.4.4 Experiments on AVIRIS Cuprite data

We now conduct experiment on HSI data acquired by AVIRIS sensor [113] and for this experiment, we use sub-images of the size 250×190 pixels having 224 bands with 14 endmembers. On this data, the experiment is conducted on 188 bands after removing the noisy bands.

Since in this case, the ground truth abundances are not available, we used the data reconstruction error (DRE) measured in terms of RMSE at each pixel, between the original and the reconstructed HSI (reconstructed using the estimated abundance maps) as the quantitative measure. The quantitative comparison are shown in Table 4.5. It can be seen that the proposed approach has the least DRE (both least mean and standard deviation) when compared to the other methods. The estimated abundances using the proposed approach are found visually consistent with the state-of-the-art approaches and are shown in Figure 4.12.

Table 4.5: Quantitative comparison on real Cuprite data acquired by AVIRIS.

Algorithm	DRE	
	mean	standard deviation
FCLS [58]	0.0041	0.0049
DGAE [82]	0.0046	0.0055
cSUnSAL [97]	0.0042	0.0051
mIGMRF [96]	0.0039	0.0043
MaxEnt [59]	0.0064	0.0059
SPU [60]	0.0041	0.0049
FCLS-TV [111]	0.0040	0.0045
Proposed	**0.0038**	**0.0042**

4.5 Conclusion

In this chapter, we have presented a new approach for abundance estimation by using mIGMRF and sparsity-based priors in the regularization framework. We have incorporated a sparsity-induced prior that provides sparse representation of

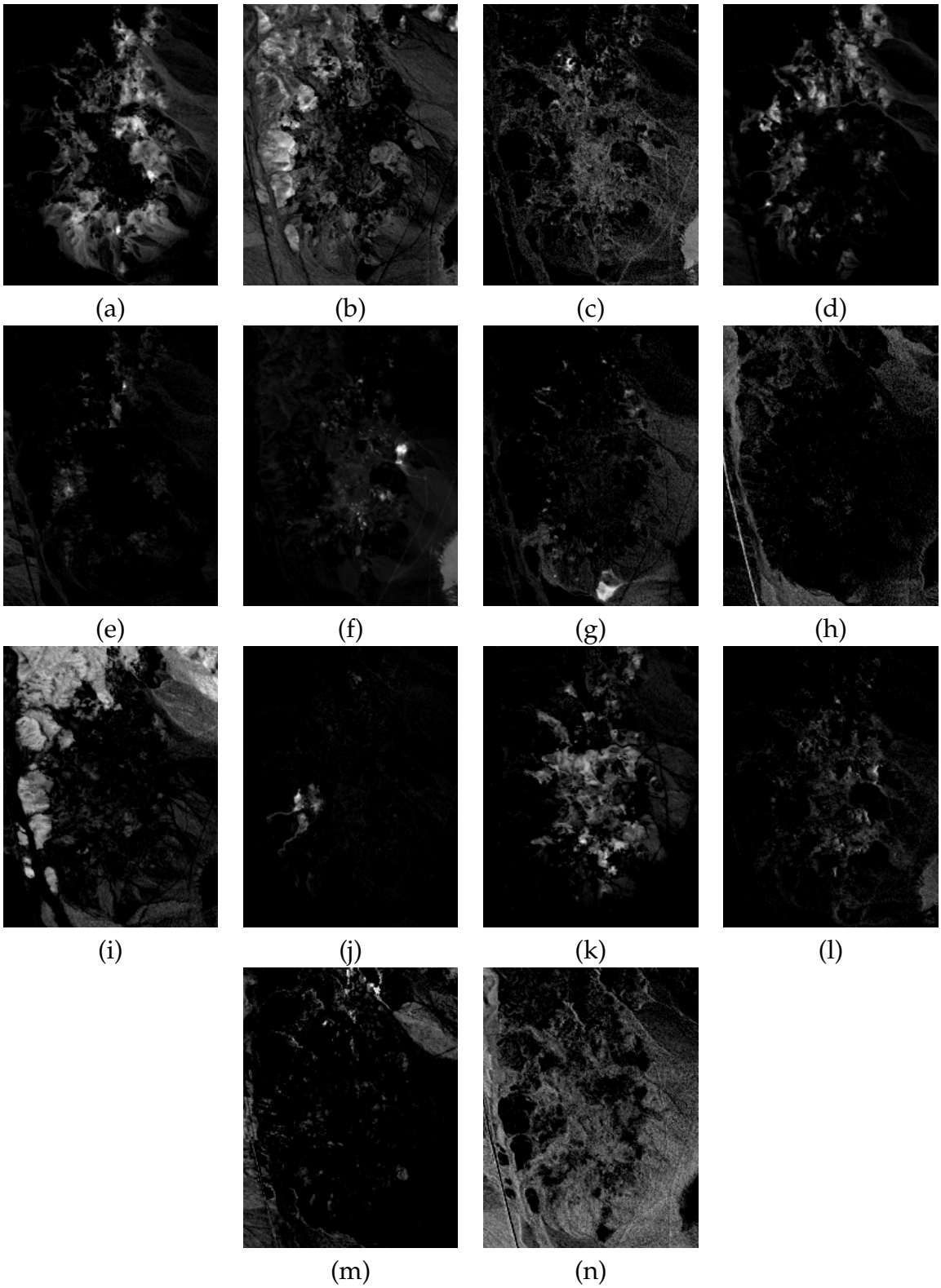

Figure 4.12: Estimated abundance maps for AVIRIS Cuprite data using the proposed approach. (a) Alunite (b) Pyrope #1 (c) Nontronite (d) Dumortierite (e) Kaolinite (f) Muscovite (g) Kaolinite #3 (h) Andradite #1 (i) Sphene (j) Buddingtonite (k) Chalcedony (l) Montmorillonite (m) Pyrope #2, and (n) Desert vanish.

abundance using the K-SVD based adaptive dictionaries. Use of two priors resulted in a better estimate of the abundances. The estimation is carried out using a two-phase iterative algorithm that refines the abundance maps at every iteration. The experiments conducted on two synthetic and two real datasets confirm the efficacy of the proposed approach.

In the next chapter, we continue with our work on abundances and use them in super-resolving the HSI data. We know that HSIs have a low spatial resolution, and the estimated abundance maps carry the spatial information of these. To this end, we discuss a new framework to increase the spatial resolution of the abundances first and then use them to super-resolve the HSIs.

CHAPTER 5

Hyperspectral Image Super-resolution using Spectral Unmixing and Transfer learning

In the last two chapters, we discussed on estimation of abundances using spatial regularizations. In this chapter, we deal with how one can make use of abundances in spatial resolution enhancement of hyperspectral images (HSIs). We know that, HSIs represent reflectance in hundreds of contiguous electromagnetic bands of narrow bandwidth. Abundance maps and endmembers convey spatial and spectral characteristics within the scene. The richness in spectral information in HSIs can be made use of in numerous applications, such as classification of scene data, target detection, change detection, and anomaly detection. However, it is difficult to acquire the high (spatial) resolution (HR) for HSI due to the hardware constraints. One can improve the accuracy of the tasks at hand if we have the data with high spectral as well as spatial resolutions [114, 115]. This motivates us to develop an algorithm to super-resolve HSI that gives us high spatial resolution HSI without much compromise on its spectral details.

The low spectral resolution (LR) images such as panchromatic image (PAN), and multispectral image (MSI) have been recorded in a few spectral bands. However, these images have much finer spatial information when compared to HSIs. So, the high spatial auxiliary image can be used to improve the spatial resolution of the HSI. Recently, many HSI super-resolution (SR) methods have been proposed [116–124] which use the auxiliary HR image to enhance low-resolution (LR) HSI image. Here, auxiliary image and the LR HSI represent the same scene. A pan-sharpening is a similar process which enhances the spatial resolution of

HSI by fusing it with a PAN [125]. Some techniques [117–119] fuse luminance component of a high spatial resolution image with HSI, however, they distort spectral information of HSI [126]. Methods based on matrix factorization have been used to improve the spatial resolution of HSI with the help of high spatial resolution auxiliary image [120–124]. Note that, it is challenging to acquire such an auxiliary image for the same scene. Also, the resultant super-resolved images may be blurred due to the registration error that happens due to capture of different resolution images. This motivates us to use SR methods in which auxiliary image itself is not required.

We know that the process of spectral unmixing reveals abundance (material) maps of the HSI data. Hence, use of the estimated abundances can be used in enhancing the spatial resolution of HSI images. In this chapter, first the spectral unmixing is used to obtain the abundances which are in turn used in obtaining the HR abundances for super-resolution of band images of HSI.

In order to learn the mapping from LR to HR, one can train a deep convolution neural network (CNN) using large number of LR-HR HSI pairs. However, such pairs are seldom available for remotely sensed data. Nevertheless, we know that transfer learning can be used to apply the learned feature knowledge in one domain to another domain. The remotely sensed images exhibit low-level feature similarities with the natural images [127]. Hence, we derive this knowledge from natural images to enhance the spatial resolution of HSIs. Pretrained weights with input as natural images can be used to find the mapping from LR to HR abundance maps. This kind of representation refers to transfer learning. The super-resolved HSIs are then generated by first obtaining the HR abundances after regularization, and combining them with the estimated endmembers. It is interesting to note that the given HSIs are not directly used here to get their HR images. The most important advantage in super-resolving the abundance maps using transfer learning is the reduced computational complexity when compared to directly using HSIs since the number of abundances in a scene is much less when compared to total number of band images in a HSI data.

As discussed in earlier chapters, the abundance maps have homogeneous as

well as non-homogeneous regions and their values vary locally. Hence, for regularization, we consider a prior that is adaptive to variations in abundance values. To this end, we use the modified Inhomogeneous Gaussian Markov random field (mIGMRF) prior as used in chapter 3 since it better captures the smoothness and also the discontinuities among the abundances. We apply mIGMRF priors on both LR and HR abundance maps which results in improved HR estimate of abundance maps and the same are then used to obtain the super-resolved HSIs.

In summary, we develop a novel super-resolution technique for HSIs by making use of spectral unmixing and transfer learning. To do this, we first train a deep CNN to learn the mapping from the LR to HR natural images and use the same for transfer learning to get the initial estimates of the super-resolved abundances where the input corresponds to LR abundances. To get the better estimates of abundances and hence to improve the SR of HSIs, we use a regularization framework in which both the LR and HR abundances are modelled as IGMRF that serves as the prior. Finally, the SR HSIs are obtained by using a linear mixing model that uses the SR abundances and the endmembers estimated using an appropriate technique.

5.1 Proposed approach

The block diagram of the proposed approach is shown in Figure 5.1. Given the LR HSI, we first unmix it using robust collaborative nonnegative matrix factorization (R-CoNMF) [72] to obtain the endmembers and initial LR abundance maps. Note that any other suitable approach may also be used. Using the LR abundances, we obtain the initial estimate of super-resolved (initial HR) abundances by transfer learning in which a pre-trained CNN on natural images is used [128]. In the next stage, we optimize an objective function consisting of data term that uses linear mixture model (LMM) and two IGMRF prior terms to obtain super-resolved abundance maps. Every iteration in optimization process improves spatial resolution of abundances which are then used as input to trained CNN network to get updated HR abundances. Super-resolved HSIs are obtained using the HR abun-

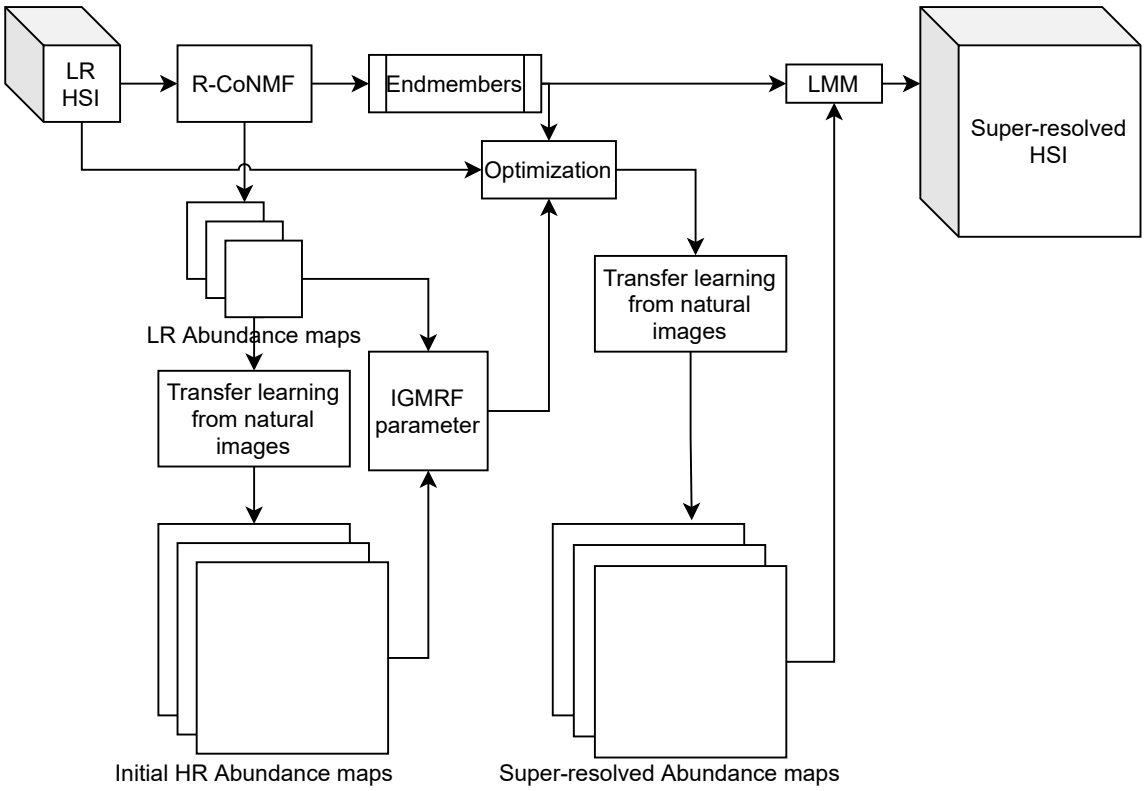

Figure 5.1: Block diagram of hyperspectral image super-resolution using spectral unmixing and transfer learning.

dance maps obtained by the optimization and the estimated endmembers.

In order to apply IGMRF model for SR, two IGMRF terms one for LR abundances and another one for HR abundances are considered along with the LMM data term. We estimate the both prior parameters knowing the abundances as explained in section 3.2 of chapter 3. For the LR abundances, the IGMRF parameters can be obtained using the abundance maps derived using R-CoNMF and the same for HR can be obtained from the initial estimate of HR abundances explained in (section 5.2). These parameters are then used in our regularization framework (section 5.3) and refined iteratively to obtain the super-resolved abundances which are then used to get the super-resolved HSIs.

5.2 Transfer learning for super-resolution of abundance maps

Transfer learning opens the scope for knowledge transfer from one domain to another which has a similar data distribution [129]. In this chapter, to obtain the SR of abundance maps, we use a deep CNN model trained on natural images for SR presented in [128] for transfer learning. This deep CNN architecture directly finds the mapping from LR image X to HR image Y by optimizing the following objective function among HR training and reconstructed $\mathcal{F}\left(X^i;\Theta\right)$ images, where, Θ correspond to the model parameters.

$$\min_{\Theta} \sum_{i=1}^{n} \|\mathcal{F}\left(X^i;\Theta\right) - Y^i\|_F^2. \tag{5.1}$$

Here, n corresponds to total number of training images, and F stands for Frobenius norm. We use the learnt parameters Θ and the function $\mathcal{F}(.)$ (trained network) to super-resolve the estimated abundance maps to generate the HR abundance maps. We thus obtain the initial HR abundances by super-resolving the initial LR abundances.

5.3 Regularization and HSI super-resolution

Given the LR HSI data, we obtain the LR abundances and the corresponding endmembers using the R-CoNMF [72]. We then estimate the HR abundance maps by using the following regularization (energy minimization) framework that has both data and prior terms and then using transfer learning. Here, the data term is constructed by considering LMM, the prior terms are formed by adding the two IGMRF priors on LR and HR abundance maps. With this, and using Eqs. in

chapter 3 i.e., (3.3),(3.4). the final energy function can be written as,

$$
\begin{aligned}
&E(\boldsymbol{\alpha}_{LR}) \\
&= \sum_{(x,y)} \|\mathbf{r}(x,y) - \mathbf{M}\boldsymbol{\alpha}_{LR}(x,y)\|^2 + \\
&\sum_{p}\sum_{(x,y)} \left\{ b^{x_{IGMRFLR}}_{(x,y,p)} \left\{ (\alpha_{LR}(x-1,y,p) - \alpha_{LR}(x,y,p))^2 \right\} \right. \\
&\left. + b^{y_{IGMRFLR}}_{(x,y,p)} \left\{ (\alpha_{LR}(x,y-1,p) - \alpha_{LR}(x,y,p))^2 \right\} \right\} + \\
&\sum_{p}\sum_{(x,y)} \left\{ b^{x_{IGMRFHR}}_{(x,y,p)} \left\{ (\alpha_{HR}(x-1,y,p) - \alpha_{HR}(x,y,p))^2 \right\} \right. \\
&\left. + b^{y_{IGMRFHR}}_{(x,y,p)} \left\{ (\alpha_{HR}(x,y-1,p) - \alpha_{HR}(x,y,p))^2 \right\} \right\}.
\end{aligned}
\tag{5.2}
$$

Note that we have replaced b^{x}_{IGMRF} and b^{y}_{IGMRF} in Eq. (3.4) by $b^{x_{IGMRFLR}}$, $b^{y_{IGMRFLR}}$, $b^{x_{IGMRFHR}}$ and $b^{y_{IGMRFHR}}$. This is to incorporate IGMRF prior on both LR and HR images. Optimization of Eq. (5.2) for $\boldsymbol{\alpha}_{LR}$ is carried out using Adam optimizer [87] and used as input to trained CNN to get the updated $\boldsymbol{\alpha}_{HR}$ at every iteration till convergence. Note that Eq (5.2) is optimized for $\boldsymbol{\alpha}_{LR}$ and the transfer learning is used to update $\boldsymbol{\alpha}_{HR}$. Final $\boldsymbol{\alpha}_{HR}$ considered as the super-resolved abundance map is then incorporated in the LMM framework to yield the super-resolved HSI. Note that in Eq. (5.2), $b^{x_{IGMRFLR}}$, $b^{y_{IGMRFLR}}$ are obtained using initial estimate of LR abundance maps and $b^{x_{IGMRFHR}}$, $b^{y_{IGMRFHR}}$ are obtained using initial estimate of HR abundances. These IGMRF parameters as well as $\boldsymbol{\alpha}$'s are updated iteratively by optimization and transfer learning to get the final super-resolved abundances.

Let LR HSI has the size of $m \times n \times l$ and can be represented in matrix form $Y \in R^{l \times mn}$. Similarly, abundance maps $\boldsymbol{\alpha}_{LR}$of size of $m \times n \times p$ can be represented as matrix $\boldsymbol{S}_{LR} \in R^{p \times mn}$. Both LR and HR HSI represent the same scene, their end-member matrix $\boldsymbol{M} \in R^{l \times p}$ will be the same. Once the super-resolved abundance maps $\boldsymbol{\alpha}_{HR}$of size of $\mathcal{M} \times \mathcal{N} \times p$ are obtained ($\mathcal{M} > m$, $\mathcal{N} > n$) and are represented as matrix $\boldsymbol{S}_{HR} \in R^{p \times \mathcal{MN}}$, the final super-resolved HSIs are obtained by $Y_{HR_{l \times \mathcal{MN}}} = \boldsymbol{M}_{l \times p} \boldsymbol{S}_{HR_{p \times \mathcal{MN}}}$. To better understand, in Figure 5.2, Illustration for an example data is shown for both proposed and auxiliary image based method. As shown in Figure 5.2 (a), only three abundance maps are used to super-resolve LR

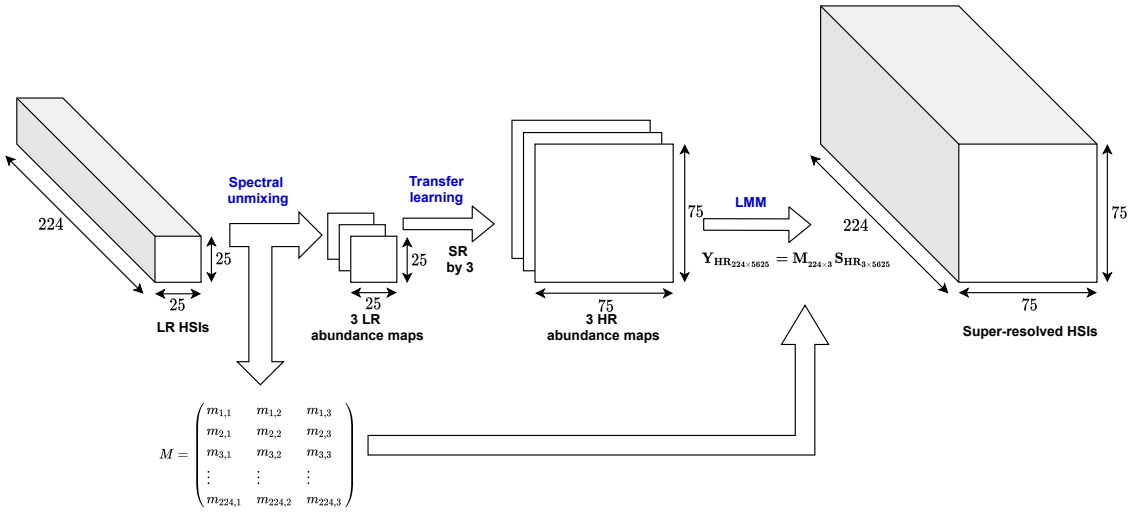

(a) Proposed

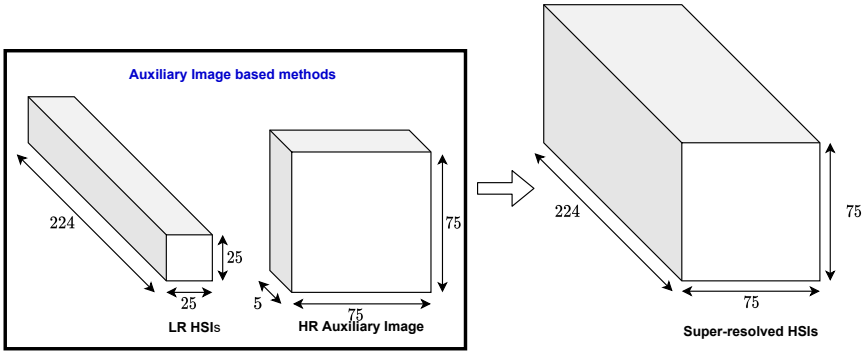

(b) Auxiliary image based method

Figure 5.2: Illustration of HR HSI generation process.

HSIs of size $25 \times 25 \times 224$. While, in case of auxiliary based method, both LR HSIs and HR auxiliary image of size $75 \times 75 \times 5$ are used to get super-resolved HSIs.

5.4 Experimental Illustration

We now demonstrate the efficacy of our approach by conducting experiments on synthetic as well as on the real HSIs. The synthetic data is generated using the linear mixing of spectral signatures with 224 bands from the USGS library [89] as explained in section 3.4.1. The size of each synthetically generated HSI is 75×75 pixels. The real HSIs used in our experiment has 610×340 pixels spread in 103 spectral bands with 9 endmembers captured at Pavia University by ROSIS sensor [130].

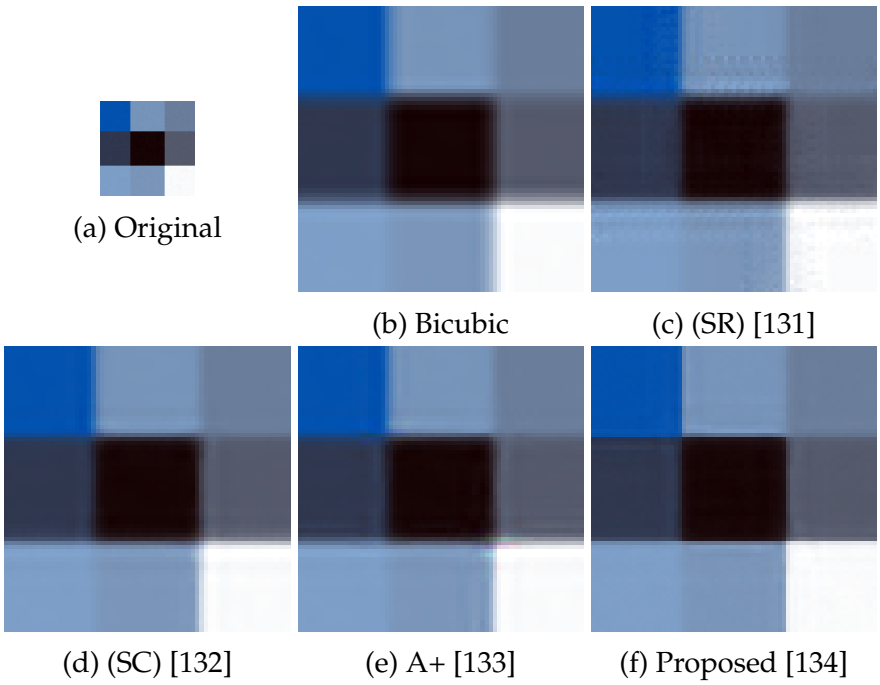

(a) Original (b) Bicubic (c) (SR) [131]

(d) (SC) [132] (e) A+ [133] (f) Proposed [134]

Figure 5.3: Super-resolution by a factor of 3 for synthetic data (pseudo colour images (composed of bands 183, 193 and 207 for the red, green, and blue channels, respectively)).

Table 5.1: Results of super-resolution on synthetic data.

Measure	Algorithm				
	Bicubic	SR [131]	SC [132]	A+ [135]	Proposed [134]
RMSE [93]	0.0575	0.0455	0.0431	0.0474	**0.0316**
MPSNR [136]	24.7941	26.8211	27.2912	26.3122	**29.7253**
MSSIM [136]	0.8650	0.8837	0.9204	0.9021	**0.9378**
SAM [94]	0.04636	0.0392	0.0334	0.0361	**0.0261**
UIQI [137]	0.3536	0.3355	0.3928	0.3929	**0.4896**

To perform experiment we generate LR data by downsampling both synthetic and real data by a factor of 3. Comparison of the proposed method is shown with the state-of-the-art methods of single image SR approaches such as sparse representation (SR) [131], sparse coding (SC) [132], and A+: Adjusted Anchored Neighborhood Regression for Fast SR (A+) [135]. The results are quantitatively evaluated using root mean squared error (RMSE) [93], mean peak signal-to-noise ratio (MPSNR) [136], mean structure similarity index (MSSIM) [136], spectral angle mapper (SAM) [94], and universal image quality index (UIQI) [137]. Note that these measures are used by the SR community. Here, ideal values of RMSE,

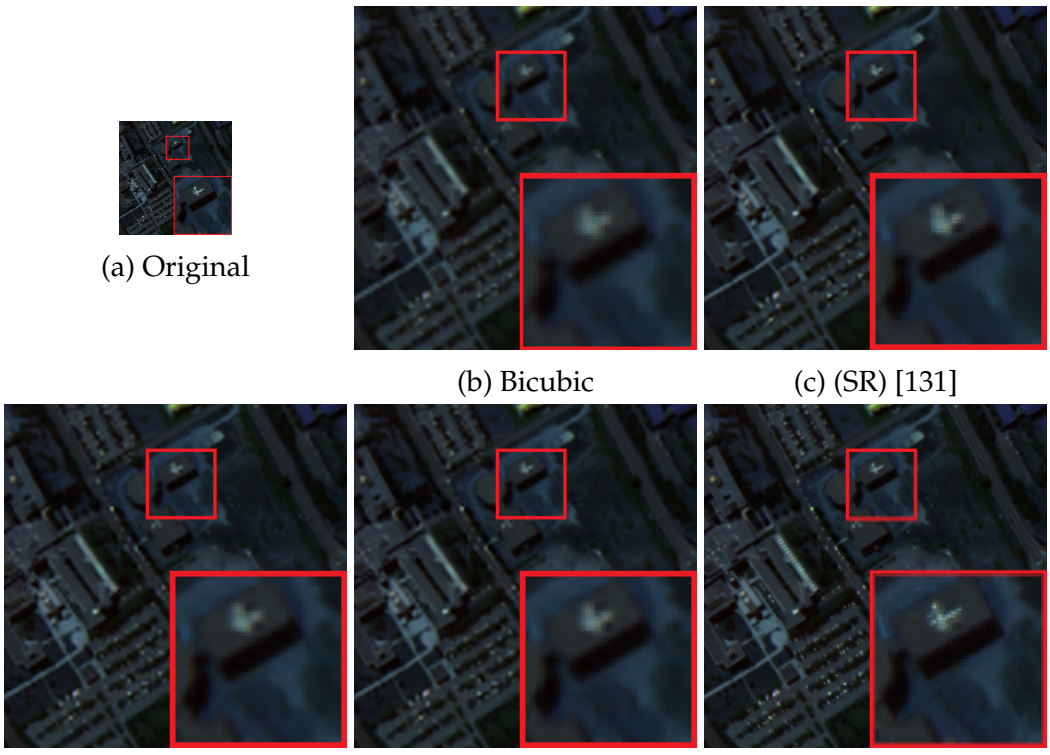

(a) Original (b) Bicubic (c) (SR) [131]

(d) (SC) [132] (e) A+ [135] (f) Proposed [134]

Figure 5.4: Super-resolution by a factor of 3 for real data (pseudo colour images (composed of bands 5, 28 and 56 for the red, green, and blue channels, respectively)) captured at Pavia university.

MPSNR, MSSIM, SAM, UIQI are 0,∞,1,0,1, respectively.

The quantitative results on synthetic data are given in TABLE 5.1 and the SR pseudo colour images (composed of bands 183, 193 and 207 for the red, green, and blue channels, respectively) are shown in Figure 5.3. It is clear from the TABLE 5.1 and Figure 5.3 that our approach performs better in terms of quantitative measures as well as qualitative assessment when compared to other approaches. The results on real data are shown in TABLE 5.2 and the corresponding SR pseudo colour images (composed of bands 5, 28 and 56) magnified by a factor of 3 are displayed in Figure 5.4. It can be seen that the super-resolved image obtained using the proposed method shown in Figure 5.4 (f) appears visually better and has better contrast when compared to the others displayed in Figure 5.4 (b)-(e). The low values of SAM in TABLE 5.1 and TABLE 5.2 indicate that spectral distortion is minimum in the proposed approach.

Table 5.2: Results on real data.

Measure	Algorithm				
	Bicubic	SR [131]	SC [132]	A+ [135]	Proposed [134]
RMSE [93]	0.0351	0.0315	0.0314	0.0312	**0.0301**
MPSNR [136]	29.0781	30.0182	30.0572	30.0530	**31.5491**
MSSIM [136]	0.8100	0.8336	0.8461	0.8466	**0.8586**
SAM [94]	0.0816	0.0811	0.0748	0.0768	**0.0696**
UIQI [137]	0.6916	0.6771	0.7518	0.7533	**0.7886**

5.5 Conclusion

Here, we have proposed a novel approach to enhance the spatial resolution of HSIs by spectral unmixing using regularization and transfer learning. We use spatial information available in the abundance maps of the HSI data, and transfer this knowledge to super-resolve the HSI. The experiments conducted on synthetic and real HSI give better results for the proposed method when compared to state-of-the-art. Results show the capability of transfer learning and regularization to super-resolve HSI images without compromising on the spectral details.

In the previous chapters, we used spatial regularization framework while working with abundances. We know that the spectral signatures are recorded in contiguous narrow bands and hence are spectrally correlated. Hence, in our final work in the next chapter, we use spectral regularization in addition to spatial regularization for improving the spectral unmixing. There we estimate both the endmembers and abundances.

CHAPTER 6

Spectral unmixing using autoencoder with spatial and spectral regularizations

In many of the practical scenarios, the endmembers present in the HSI are unknown which motivates us to extract endmembers using the unsupervised method. Hence, in this chapter we estimate both the endmembers and the abundances. Many of the researchers have developed endmember extraction algorithms by considering pure pixel assumption [12]. One of the convex-geometry-based algorithms called vertex component analysis (VCA) [44] considers pure pixel assumption for endmember extraction. Here, the endmembers represent the vertices of a simplex that represent the data. Some of convex-geometry-based algorithms minimize or maximize the volume of the simplex to extract the endmembers [43, 48, 138–140]. The non-negative matrix factorization (NMF) is also explored for unsupervised spectral unmixing that extracts the endmembers and estimate their abundances without considering pixel purity assumption [47, 72, 141, 142]. NMF is a technique to factorize a matrix into two non-negative matrices. In the case of spectral unmixing, the NMF can be used to factorize HSI data matrix into endmember and abundance matrices.

Recently, approaches based on deep learning are outperforming traditional approaches for solving various problems in the area of hyperspectral imaging [77]. Here, to perform unsupervised spectral unmixing, one can use autoencoder (AE) which can be trained to find the lower dimensional representation of the data by minimizing the reconstruction error. The authors in [80], use cascade autoencoder to solve for spectral unmixing where HSI data is denoised using the marginalize

denoising autoencoder (mDA) and then AE is used to unmix the HSI using non-negative sparse autoencoder with tied weights. In [143], untied weights approach that overcomes the limitations of tied weights is proposed. However, the authors in [143] do not use regularizations to capture the dependencies inherent in the data.

Regularization based techniques are used to improve the solution in hyperspectral imaging [83]. Researchers have used spatial regularization in semi-supervised way in which they apply it on abundance maps [63–65], while the priors are not adaptive. We know that abundances have both homogeneous as well as non-homogeneous regions. Hence, the adaptive prior that captures the variation in abundance values should improve the solution. In order to capture smoothness while preserving discontinuities among the abundances, IGMRF is used at every pixel location [96, 110]. In the case of spectral signatures, the neighbouring values are close to each other since they are recorded in contiguous spectral bands. Hence, to capture the spectral dependencies, we also use IGMRF on these signatures.

In this chapter, given the HSI and number of endmembers, we employ AE with IGMRF priors to extract endmembers and their abundances. By using the linear decoder, the AE incorporates LMM that represents abundances as hidden units. To obtain IGMRF parameters, an initial estimates of endmembers and abundances are required. To do this, we extract endmembers using VCA [44] and estimate the abundances using FCLS [58]. Nevertheless, one may use any suitable unmixing technique to obtain the initial parameters. With these initial estimates, the network is trained using backpropagation to get the final solution. Other approaches use additional methodology to denoise data while here spatial and spectral regularizations take care of noise giving us improved results.

6.1 Problem formulation and proposed method

Let us consider the HSI data representation as $\boldsymbol{Y} \in R^{l \times n}$ matrix containing the n observed spectral vectors in its columns, then LMM in (3.1) can be described as,

$$\boldsymbol{Y} = \boldsymbol{M}\boldsymbol{S} + \boldsymbol{N}, \tag{6.1}$$

where, $\boldsymbol{N} \in R^{l \times n}$ represents the noise; $\boldsymbol{M} \in R^{l \times p}$ is the endmember matrix with each column representing one of the endmember signatures, and $\boldsymbol{S} \in R^{p \times n}$ denotes the corresponding abundance matrix, with each column representing the mixing coefficient of the p endmembers in making one mixed pixel.

We know that an autoencoder can be used to learn the lower dimension of the data in an unsupervised manner using data reconstruction error as the criteria. Spectral unmixing can be achieved by encoding HSI data in the hidden units representing the abundances and reconstructing the data using a linear operator, i.e., using decoder as a endmember matrix. HSI data $\boldsymbol{Y}$ is encoded using weight $\boldsymbol{W} \in R^{p \times l}$ as the abundance matrix $\boldsymbol{S}$, where rectified linear unit (ReLU) is used as a non-linear activation function. ReLU provides non-negative values of abundances, i.e., $\boldsymbol{S} = \sigma(\boldsymbol{W}\boldsymbol{Y})$, where σ represents ReLU function. Here, we use a similar approach proposed in [58] for sum-to-one constraint on abundance. At the decoder, abundance vector is multiplied with the endmember matrix M to reconstruct the data as $\widehat{\boldsymbol{Y}}$. The endmembers are extracted as the trained weights of the decoder and abundances are calculated by the obtained encoder weights. The decoder weights are made non-negative using non-negativity cost. To find both the endmembers and abundances, we minimize the cost function consisting of reconstruction error (based on LMM) and priors. The reconstruction error is given by,

$$J_{LMM}(\boldsymbol{W}, \boldsymbol{M}) = \frac{1}{2}\|\boldsymbol{M}\boldsymbol{S} - \widehat{\boldsymbol{Y}}\|_F^2. \tag{6.2}$$

In HSI data, abundance maps have a smooth region with edges and hence spatial regularization can be applied on these maps to obtain a better solution. In

addition to that, the reflectances are recorded in hundreds of contiguous bands which makes the variation of reflectance band-wise smooth with limited discontinuity. These observations motivate us to use spatial as well as spectral regularization for better solution of spectral unmixing. In [96], IGMRF is used to capture smoothness by preserving discontinuity in data. Hence, IGMRF prior is used for spatial and spectral regularization and for that IGMRF priors are applied on abundances and endmembers. To initialize IGMRF parameters, we need initial estimates of endmembers and abundances. Initial endmembers are extracted using VCA [44] and then abundances are estimated using FCLS [58]. The IGMRF parameters for abundance maps in horizontal and vertical directions are calculated using the initial estimate of abundances to capture spatial dependencies. In order to capture spectral dependencies, we calculate IGMRF parameters using the initial estimate of endmembers computed band-wise. To improve the solution, we also apply IGMRF priors spatially as well as spectrally on reconstructed HSI. The initial reconstructed HSI is obtained by the initial estimate of endmembers and abundances. The total cost function consists of reconstruction error, IGMRF prior terms and non-negativity cost for the decoder. The Adam optimizer [87] is used to minimize this cost function to obtain the final solutions. The block diagram for proposed approach shown in Figure 6.1.

6.2 IGMRF priors for spatial and spectral regularization

In this section, we describe IGMRF priors employed on abundances, endmembers and on reconstructed HSI.

6.2.1 Spatial regularization on abundance maps

We incorporate IGMRF on the hidden unit of Autoencoder to apply spatial regularization on abundance maps. Here, the abundance at (x, y) location can be represented as $\alpha(x, y) \in \boldsymbol{S}$. Hence, abundance value at (x, y) location for the p^{th} endmember can be represented as $\alpha(x, y, p) = r(x, y)W(:, p)$, where $r(x, y) \in \boldsymbol{Y}$

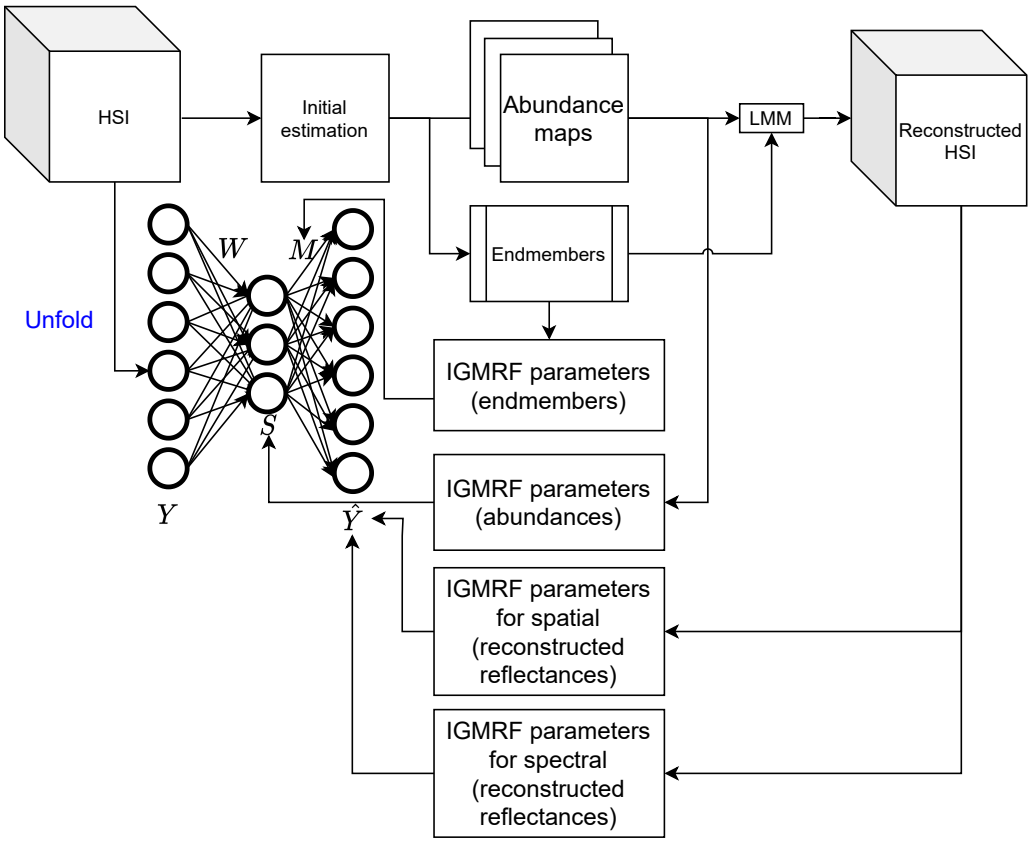

Figure 6.1: Block diagram of proposed spectral unmixing using autoencoder with spatial and spectral regularizations.

and $W(:,p) \in \boldsymbol{W}$. The cost function for spatial regularization on abundances can be given [84] as,

$$\begin{aligned} J_{\boldsymbol{\alpha}}(\boldsymbol{W},\boldsymbol{M}) = \\ \sum_{p}\sum_{(x,y)} \Big\{ b_1^x(x,y,p) \Big\{ (\alpha(x-1,y,p) - \alpha(x,y,p))^2 \Big\} \\ + b_1^y(x,y,p) \Big\{ (\alpha(x,y-1,p) - \alpha(x,y,p))^2 \Big\} \Big\}, \end{aligned} \tag{6.3}$$

where, b_1^x and b_1^y represent the spatially adaptive IGMRF parameters in horizontal and vertical directions for abundance maps. Since the values of abundances vary between 0 and 1, the expression proposed in [84] (as seen in chapter 3) sets the parameter values to constant thus imposing the same penalty at every location. In order to avoid this a modified expression for IGMRF was derived in chapter 3

as,

$$b_1^x(x,y,p) = 1 - \frac{1}{1+\mathrm{e}^{-5\times|(\alpha_{in}(x-1,y,p)-\alpha_{in}(x,y,p))|}},$$
$$b_1^y(x,y,p) = 1 - \frac{1}{1+\mathrm{e}^{-5\times|(\alpha_{in}(x,y-1,p)-\alpha_{in}(x,y,p))|}}, \tag{6.4}$$

where, $\boldsymbol{\alpha}_{in}$ represent the initial estimate of abundance. The IGMRF parameter is now a nonlinear function of the difference between two neighbouring abundances and has a larger penalty smooth region and a smaller penalty for edges. Since the reflectance values also vary between 0 and 1, the IGMRF parameters for endmembers and reconstructed HSI are calculated in a similar manner.

6.2.2 Spectral regularization on endmembers

Since HSI data is recorded on hundreds of contiguous bands, the reflectance values for neighbouring bands do not vary much except at few locations. Hence, IGMRF priors can be applied on endmembers as well. With this the cost function for spectral regularization can be given by,

$$J_M(\boldsymbol{W},\boldsymbol{M}) = \sum_p \sum_l \left\{ b_2(l,p) \left\{ (M(l-1,p) - M(l,p))^2 \right\} \right. \tag{6.5}$$

where, b_2 represents spectrally adaptive IGMRF parameter for endmember. These parameters are calculated using the initial estimates of endmember $\boldsymbol{M}_{in}$. The parameter b_2 can be obtained as,

$$b_2(l,p) = 1 - \frac{1}{1+\mathrm{e}^{-5\times|(M_{in}(l-1,p)-M_{in}(l,p))|}}. \tag{6.6}$$

6.2.3 Spatial and spectral regularization on reconstructed HSI

We also apply IGMRF on reconstructed HSI data $\widehat{\boldsymbol{Y}}$ for spatial and spectral regularization to improve the solution. Here, the reconstructed reflectance at (x,y) location can be represented as $\hat{r}(x,y) \in \widehat{\boldsymbol{Y}}$. One can consider $\widehat{\boldsymbol{Y}}$ as stack of l images (one for each spectral band) and the reconstructed reflectance value at (x,y) location for l^{th} band can be represented as $\hat{r}(x,y,l) = \alpha(x,y)M(:,l)$ where,

$M(:,l) \in \boldsymbol{M}$. Similarly, the IGMRF prior for spectral regularization is applied on reconstructed HSI in band-wise manner. The final energy function for spatial and spectral regularization on reconstructed HSI can be given as,

$$\begin{aligned} J_r(\boldsymbol{W},\boldsymbol{M}) = \\ &\sum_{l}\sum_{(x,y)} \Big\{ b_3^x(x,y,l) \Big\{ (\hat{r}(x-1,y,l) - \hat{r}(x,y,l))^2 \Big\} \\ &+ b_3^y(x,y,l) \Big\{ (\hat{r}(x,y-1,l) - \hat{r}(x,y,l))^2 \Big\} \Big\} \\ &+ \sum_{l}\sum_{(x,y)} \Big\{ b_4(x,y,l-1) \Big\{ (\hat{r}(x,y,l-1) - \hat{r}(x,y,l))^2 \Big\} \Big\}, \end{aligned} \tag{6.7}$$

where, b_3^x and b_3^y represent the spatially adaptive IGMRF parameters in horizontal and vertical directions while b_4 represent spectrally adaptive IGMRF parameters. The IGMRF parameter b_3^x, b_3^y and b_4 can be computed as,

$$\begin{aligned} b_3^x(x,y,l) &= 1 - \frac{1}{1+\mathrm{e}^{-5\times|(\hat{r}_{in}(x-1,y,l) - \hat{r}in(x,y,l))|}}, \\ b_3^y(x,y,l) &= 1 - \frac{1}{1+\mathrm{e}^{-5\times|(\hat{r}_{in}(x,y-1,l) - \hat{r}_{in}(x,y,l))|}}, \\ b_4(x,y,l) &= 1 - \frac{1}{1+\mathrm{e}^{-5\times|(\hat{r}_{in}(x,y,l-1) - \hat{r}_{in}(x,y,l))|}}. \end{aligned} \tag{6.8}$$

where, $\hat{\boldsymbol{r}}_{in}$ corresponds to reconstructed HSI using the initial estimate of abundance maps and endmembers.

6.3 Unmixing using modified Autoencoder

In the proposed approach, autoencoder is modified to represent LMM and also to apply spatial and spectral regularizations. In order to apply LMM, the decoder is considered as linear. With decoder weights representing the endmember matrix, the following cost is used to obtain non-negative endmembers which can be given as,

$$J(\boldsymbol{M}) = \|abs(\boldsymbol{M}) - \boldsymbol{M}\|_F^2. \tag{6.9}$$

Abundance values which represent the hidden units of the network have to follow non-negative and sum to one constraint. To apply non-negativity on the hidden unit, we use ReLU as activation function and the sum-to-one constraint is applied using an approach as given in FCLS [58].

Spatial regularization is carried out on the hidden units of the autoencoder while the spectral regularization is applied on decoder weights. Besides that, both regularizations are applied on the reconstructed HSI data. To apply these regularizations, IGMRF parameters are calculated using initial estimates of abundance and endmembers. Here, we use VCA [44] to obtain the initial estimates of endmembers and abundances are estimated using FCLS [58]. As given in Eqs. 6.4 and 6.6, b_1^x and b_1^y are calculated using initial abundances while b_2 is calculated using initial endmembers and, b_3^x,b_3^y and b_4 are calculated using reconstructed HSI generated by the initial abundances and endmembers.

To perform unmixing the autoencoder is trained using combined cost function resulting from Eqs. 6.2, 6.3, 6.5, 6.7 and 6.9. Thus the final cost function to be minimized is given by,

$$
\begin{aligned}
J(\boldsymbol{W},\boldsymbol{M}) &= \frac{1}{2}\|\boldsymbol{M}\boldsymbol{S}-\widehat{\boldsymbol{Y}}\|_F^2 \\
&+\sum_p \sum_{(x,y)} \Big\{ b_1^x(x,y,p)\Big\{(\alpha(x-1,y,p)-\alpha(x,y,p))^2\Big\} \\
&\qquad + b_1^y(x,y,p)\Big\{(\alpha(x,y-1,p)-\alpha(x,y,p))^2\Big\}\Big\} \\
&+\sum_p \sum_l \Big\{ b_2(l,p)\Big\{(M(l-1,p)-M(l,p))^2\Big\} \\
&+\sum_l \sum_{(x,y)} \Big\{ b_3^x(x,y,l)\Big\{(\hat{r}(x-1,y,l)-\hat{r}(x,y,l))^2\Big\} \\
&\qquad + b_3^y(x,y,l)\Big\{(\hat{r}(x,y-1,l)-\hat{r}(x,y,l))^2\Big\}\Big\} \\
&+\sum_l \sum_{(x,y)} \Big\{ b_4(x,y,l-1)\Big\{(\hat{r}(x,y,l-1)-\hat{r}(x,y,l))^2\Big\} \\
&+\|abs(\boldsymbol{M})-\boldsymbol{M}\|_F^2.
\end{aligned}
\tag{6.10}
$$

To carry out the optimization, we use the Adam optimizer [87] as done earlier.

6.4 Experimental Results

In this section, we present experimental results to demonstrate the efficacy of the proposed approach. Here, we conduct two experiments to test the performance of the our approach. In the first experiment, we generate synthetic data using the spectral signatures of the U.S. Geological Survey (USGS) digital spectral library [89], and perform the experiments by considering different noise levels in the data. We then show the results of another experiment on Japser Ridge real data set [144], where the true endmembers are available. We use root-mean-squre-error (RMSE) [93], abundance angle mapper (AAM) [94] and abundance information divergence (AID) [95] as quantitative measures for abundances, and spectral angle mapper (SAM) [94] and spectral information divergence (SID) [95] as quantitative measures for endmembers. The ideal values for all these measures are zero. Note that we have used three different data sets when compared to chapters 3 and 4, where we estimate abundances. One of the data sets is common. We could have compared our results of abundance estimation with methods discussed in chapter 3 and 4. However, it is clear that, since endmembers are not known here, the accuracy of estimation is lesser and hence we avoid comparing our results with the proposed methods in chapter 3 and 4.

6.4.1 Experiments on synthetic data

We generate synthetic HSIs using the Hyperspectral Imagery Synthesis tools [112] by using the linear mixing of five signatures of the USGS library [89]. The signatures of five materials are: cynide potassium, cynide zink, ammonium chloride, green slime, and cynide trihydrate. The spectral signatures of 480 contiguous bands are recorded and these are in the spectral range of $400 - 2500nm$. We generate an image cube of the size $100 \times 100 \times 480$ using the abundance maps of size $100 \times 100 \times 5$. The ground truth abundance maps are shown in Figure 6.2 (a). These abundance maps generated using synthesis tools contain both the smooth regions as well as edges.

To show the qualitative comparison, the estimated abundance maps using the

Table 6.1: Quantitative comparison of spectral unmixing on synthetic data.

Measure	Algorithm	SNR = 30dB	SNR = 20dB	SNR = 10dB	SNR = 0dB
RMSE [93]	VCA [44]	0.0882	0.0847	0.1215	0.1421
	RoCONMf [72]	0.0621	0.0713	0.1023	0.1231
	uDAS [143]	0.0618	0.0688	0.0917	0.1017
	Proposed	**0.0506**	**0.0522**	**0.0685**	**0.0920**
AAM [94]	VCA [44]	10.8919	11.7363	15.1311	18.1208
	RoCONMf [72]	5.4483	8.4213	14.2761	15.9187
	uDAS [143]	4.8712	7.2161	12.7156	13.8234
	Proposed	**4.0032**	**6.2031**	**11.5421**	**13.6534**
AID [95]	VCA [44]	2.6280	3.8489	4.1371	5.2135
	RoCONMf [72]	1.2343	2.9132	4.1008	5.2051
	uDAS [143]	0.9795	2.8327	3.3512	4.0072
	Proposed	**0.8976**	**2.6013**	**3.2712**	**3.6831**
SAM [94]	VCA [44]	5.7549	6.5536	8.0189	8.5718
	RoCONMF[72]	4.0016	5.8312	7.9122	8.0131
	uDAS[143]	3.9917	4.7490	6.8316	7.2315
	Proposed	**3.2196**	**3.5518**	**6.1669**	**7.1809**
SID [95]	VCA [44]	0.0627	0.0780	0.1109	0.2137
	RoCONMf [72]	0.0718	0.0691	0.1017	0.1801
	uDAS [143]	0.0528	0.0512	0.0802	0.1633
	Proposed	**0.0523**	**0.0507**	**0.0764**	**0.1521**

VCA-FCLS [44, 58], uDAS [143] and the proposed method are displayed in Figure 6.2 (b), (c) and (d), respectively, for the low signal-to-noise ratio (SNR) of 10dB in the data. It can be seen that spatial patterns in the abundance maps estimated using the proposed approach are consistent with the ground truths displayed in Figure 6.2 (a). In Figure 6.3, we show the plots of spectral bands vs reflectance. Here, reflectance is the endmember signature. These plots represent the estimated endmembers signatures. One can observe that the plots of estimated endmembers appear closer to the ground truth when compared to other approaches. The quantitative comparison for the synthetic data is shown in the Table 6.1 for the different SNR levels. Looking at these quantitative measures, we observe that our approach performs better when compared to the other state-of-the-art methods as illustrated in the Table 6.1.

6.4.2 Experiments on Japser Ridge data

The Japser Ridge data set consists of HSI of size 512×617 pixels and there are 224 bands which are in the spectral range of $380 - 2500nm$ with a spectral reso-

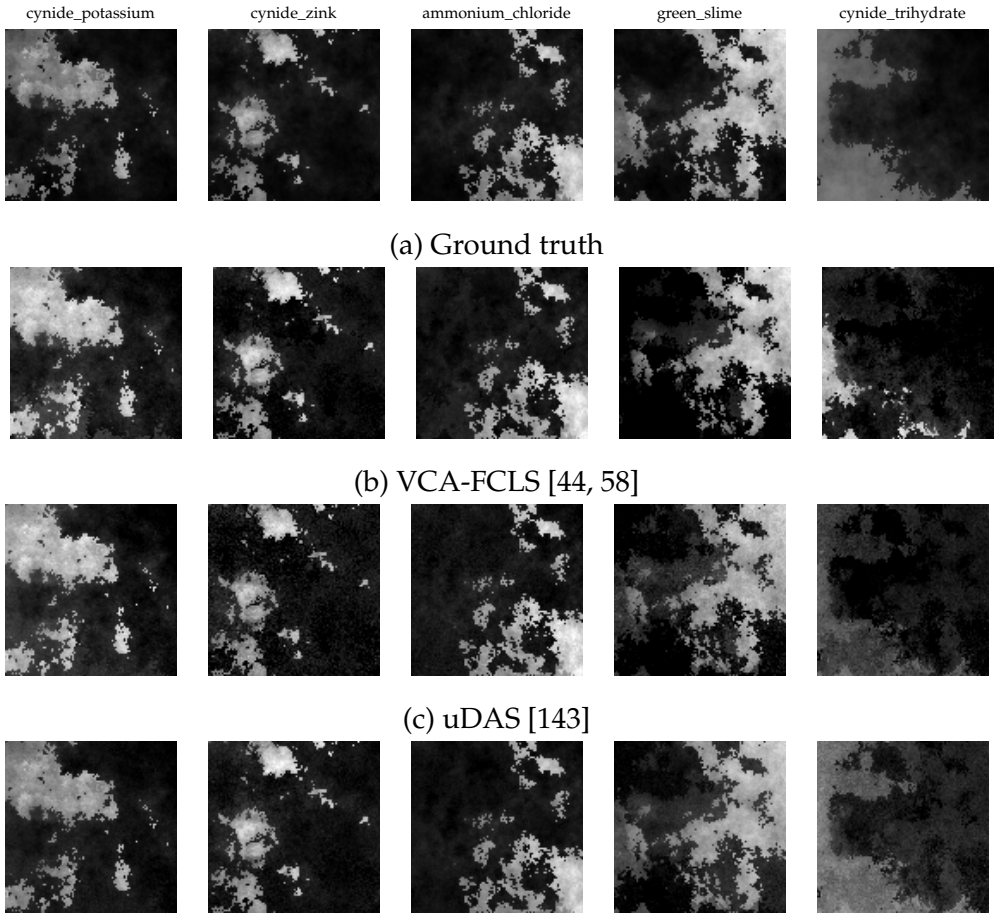

(a) Ground truth

(b) VCA-FCLS [44, 58]

(c) uDAS [143]

(d) Proposed

Figure 6.2: (a) Ground truth abundance maps for synthetically generated data at 10 dB SNR. Estimated abundance maps using (b) VCA-FCLS [44, 58], (c) uDAS [143], (d) Proposed.

lution of $9.46nm$. The bands $1-3, 108-112, 154-166$ and $220-224$ represent the atmospheric distortion and water absorption. Hence, after removing these bands, 198 bands are used for the experiments which consists of four endmembers : Tree, Water, Dirt, and Road. The ground truth abundance maps for each of the endmembers are shown in Figure 6.4 (a) and the estimated abundance maps using different approaches are shown in the Figure 6.4 (b), (c) and (d), where we observe that the abundance maps estimated using the proposed approach are visually closer to the ground truth shown in Figure 6.4 (a), as well as consistent with the VCA-FCLS [58] and uDAS [143]. The extracted endmembers using different methods are shown in Figure 6.5 which also has the endmembers extracted using the proposed method. It can be clearly seen that the extracted endmebers using

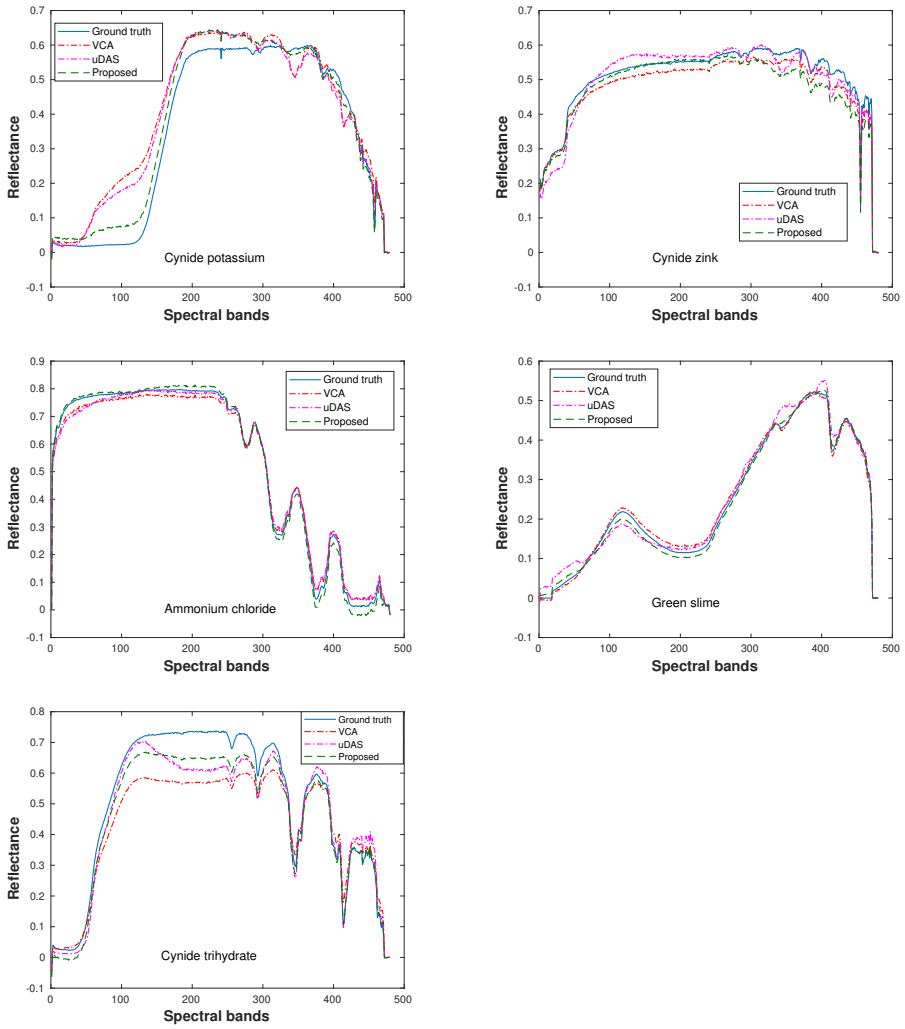

Figure 6.3: Estimated endmembers using different approaches and the ground truth considering synthetic data

the proposed method better match the ground truth when compared to other approaches. The quantitative measures for this experiment are shown in Table 6.2. Here also we see that the results for the proposed approach are superior when compared to other methods.

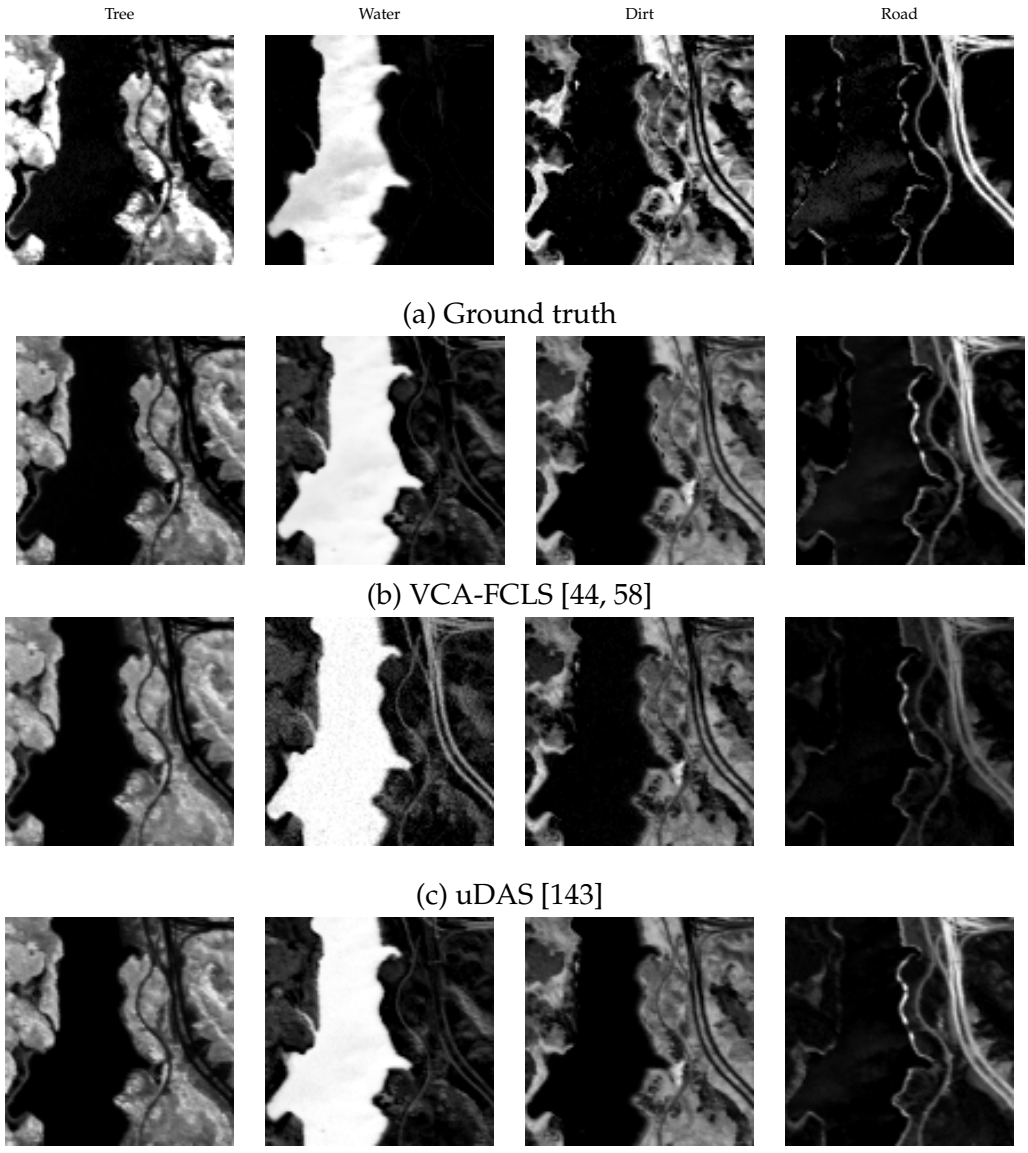

(a) Ground truth

(b) VCA-FCLS [44, 58]

(c) uDAS [143]

(d) Proposed

Figure 6.4: (a) Ground truth abundance maps for real jasper Ridge data set. Estimated abundance maps using (b) VCA-FCLS [44, 58], (c) uDAS [143], (d) Proposed.

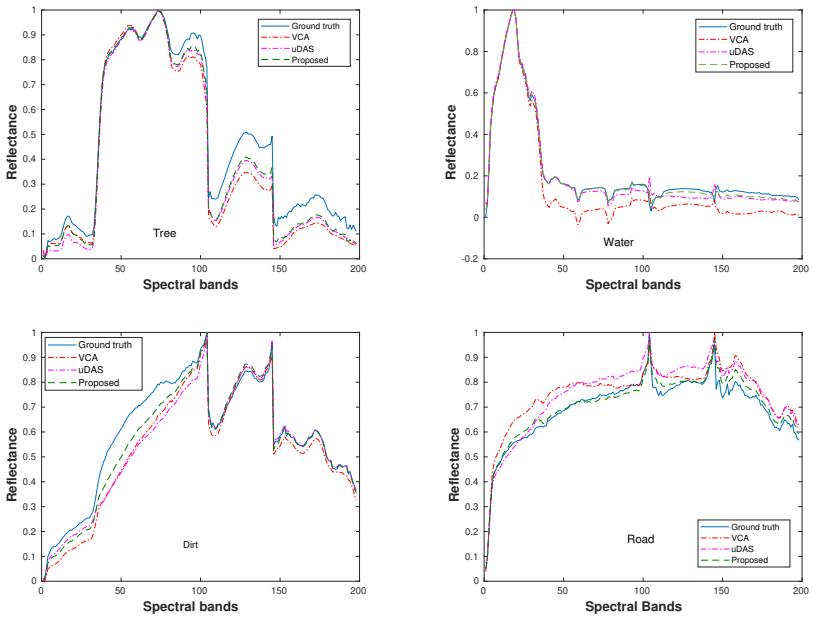

Figure 6.5: Estimated endmembers using different approaches and the ground truth considering Jasper ridge data

Table 6.2: Quantitative comparison of spectral unmixing on Jasper ridge data.

Algorithm	Measure				
	RMSE [93]	AAM [94]	AID [95]	SAM [94]	SID [95]
VCA-FCLS [44, 58]	0.1535	14.1353	4.1322	9.2681	0.1432
RoCONMF [72]	0.1491	12.2337	4.1023	8.5627	0.1301
uDAS [143]	0.1372	11.3101	4.0921	8.2219	0.1161
Proposed	**0.1279**	**10.0836**	**3.0986**	**7.9457**	**0.1082**

6.4.3 Experiments on HYDICE Urban real data

HYDICE Urban real data has a size of 307×307 pixels and there are 210 bands and after removal of bands with distortion and absorption 162 bands are used for this experiment. This data consists of four endmembers, namely: Asphalt, Grass, Tree, and Roof. For qualitative comparison, we show the ground truth along with estimated abundance maps using the he VCA+FCLS [44, 58], uDAS [143] and the proposed method which are shown in Figure 6.6. One can see that the abundance maps estimated by the proposed approach are more consistent with the ground truth than those estimated by other approaches.

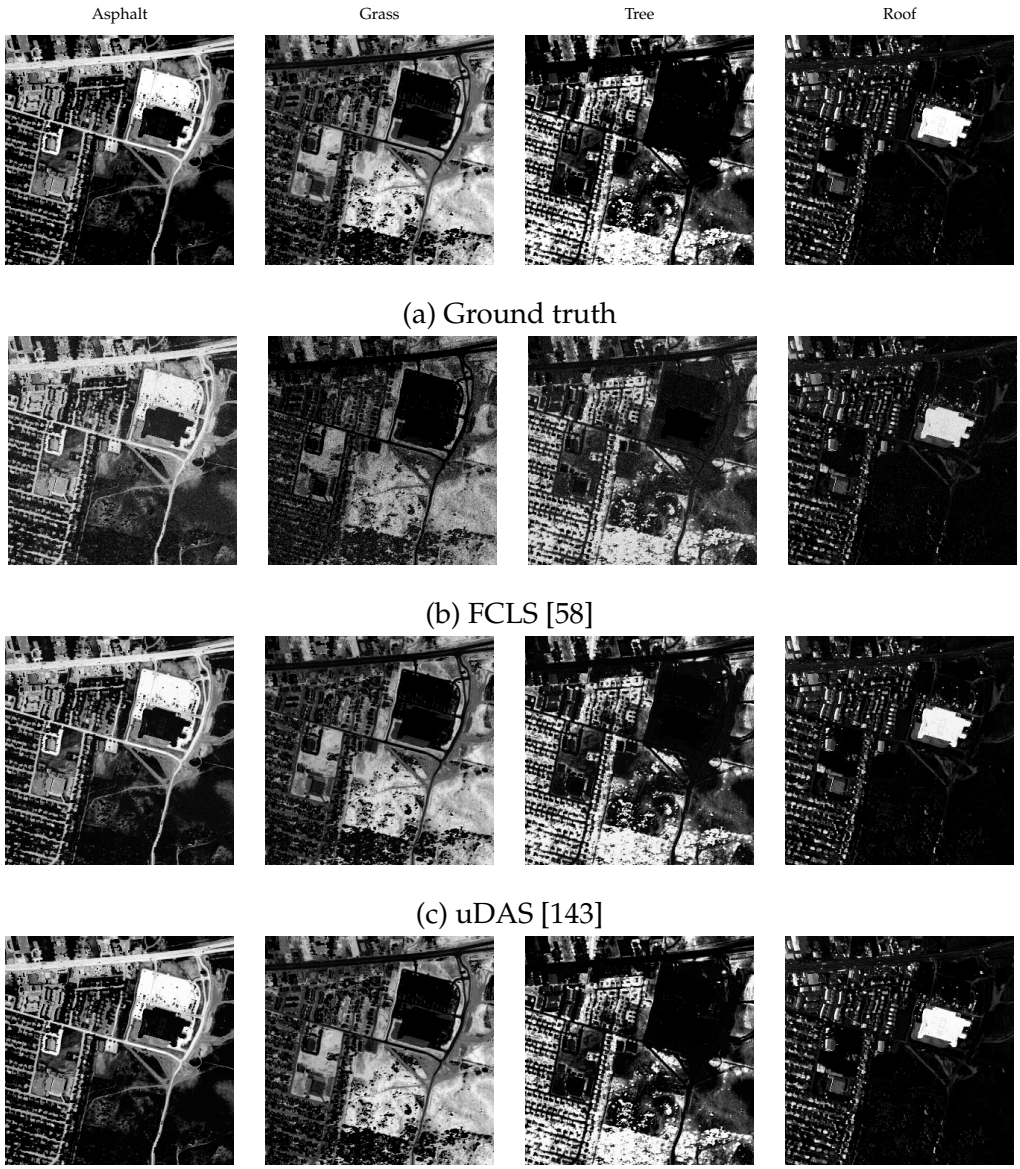

(a) Ground truth

(b) FCLS [58]

(c) uDAS [143]

(d) Proposed

Figure 6.6: (a) Ground truth abundance maps for real HYDICE Urban data set. Estimated abundance maps using (b) VCA+FCLS [44, 58], (c) uDAS [143], (d) Proposed.

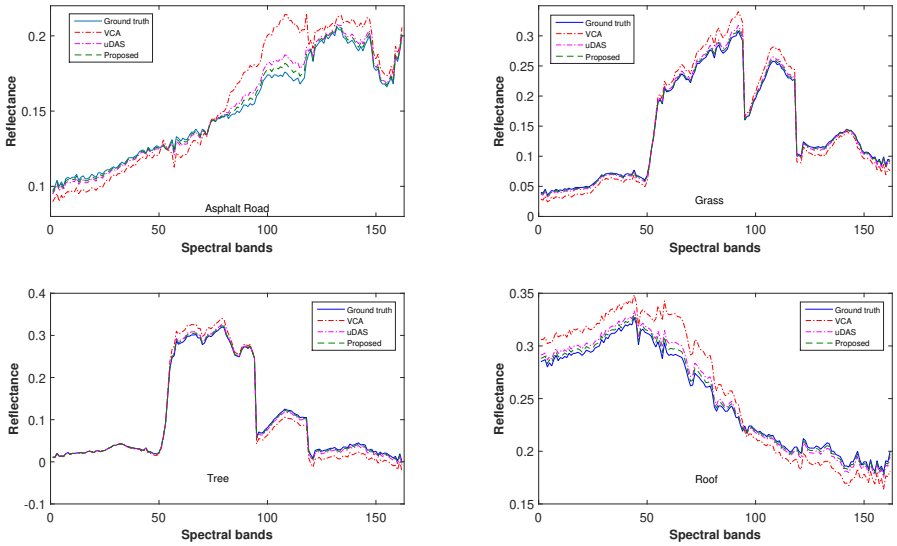

Figure 6.7: Estimated endmembers using different approaches and the ground truth considering HYDICE Urban data

Table 6.3: Quantitative comparison on HYDICE Urban data.

Algorithm	Measure				
	RMSE [93]	AAM [94]	AID [95]	SAM [94]	SID [95]
VCA-FCLS [44, 58]	0.2544	7.1347	4.5123	9.8681	0.2413
RoCONMF [72]	0.2493	6.8135	4.1103	9.5847	0.2312
uDAS [143]	0.2381	6.0312	4.1029	9.1219	0.2109
Proposed	**0.2161**	**5.9813**	**4.0965**	**8.7467**	**0.2091**

The comparison of the extracted endmembers plots using different methods along with ground truth are shown in Figure 6.7. Here, the endmembers extracted by the proposed approach are almost similar to the ground truth, whereas endmembers extracted by other methods appear slightly different from the ground truth. The quantitative measures for this experiment are shown in Table 6.3 which indicates that the proposed approach performs better than other approaches.

6.5 Conclusion

In this chapter, a novel approach for spectral unmixing using autoencoder considering spatial as well as the spectral regularizations is proposed. We use IGMRF prior to impose the constraints when using an autoencoder. To train the autoencoder, we have used backpropagation with Adam optimization. Use of IGMRF regularizer improves the efficacy of spectral unmixing that refines the endmembers as well as abundance maps. Synthetic as well as real HSI data are used in our experimentations and the outcomes validate the effectiveness of our approach. aa2

CHAPTER 7

Conclusions and Future Research Directions

The low spatial (ground) resolution hyperspectral imagery has mixed pixel phenomena, leading to a poor scene analysis. Spectral unmixing techniques decompose reflectance at each pixel location to endmembers and their abundances. Regularization based techniques give an accurate estimation that results in better quantitative analysis of the remotely acquired scene data. This thesis has focused on providing regularization based frameworks to better estimate unmixing components of hyperspectral data. In all our work, hyperspectral data is considered using linear mixing model. In this thesis, we have proposed regularization and machine learning based approaches for spectral decompositions as well as spatial resolution enhancements.

We have proposed a novel approach to estimate abundance maps by energy minimization framework by capturing spatial dependencies present in abundance maps. In this work, a new discontinuity preserving prior is proposed by modifying the expressions to compute Inhomogeneous Gaussian Markov random field (IGMRF) parameters. The modified IGMRF prior is better suited for capturing spatial dependencies within the abundance maps.

In order to capture global dependencies present in abundance, we have further incorporated a sparsity-induced prior that provides sparse representation using the K- singular value decomposition (K-SVD) based adaptive dictionaries. The experiments conducted on two synthetic and two real datasets confirm the efficacy of the proposed approach. The abundance estimation performance is significantly improved by using sparsity induced prior along with IGMRF prior in the two-step iterative algorithm.

We then propose a novel approach to enhance the spatial resolution of hyperspectral image (HSI) by using spectral unmixing, transfer learning and spatial regularization. We use the spatial information available in abundance maps of the HSI data, and transfer the knowledge to super-resolve HSI. The experiments conducted on synthetic as well as real HSI give better results for the proposed method when compared to other state-of-the-art methods. The results demonstrate the capability of transfer learning and regularization to increase the spatial resolution of HSI images without much compromising on the spectral details. It is unlike many existing approaches having the need of auxiliary HR images which is difficult to obtain in practice.

In our final work, we estimate both endmembers and abundances from the given HSI data where we have proposed a novel approach for spectral unmixing using autoencoder considering spatial as well as the spectral regularizations. We use IGMRF prior to impose these constraints within the proposed autoencoder based method. To train the autoencoder, we have used the backpropagation algorithm with Adam optimizer. Use of IGMRF regularizer improves the efficacy of spectral unmixing which refines the abundance maps as well as endmembers. Synthetic and real HSI data are used in our experimentations and outcomes of the same confirm the effectiveness of the proposed approach.

Future Research Directions

Considering the work done in this thesis, one may explore the following future directions:

- We know that a satellite can cover a vast area of the earth and can collect massive data. However, the data analysis requires ground truth information which can be collected by ground surveys and laboratory experiments on materials. So, for better earth observation, one can use online learning. For example, as proposed in chapter 6, spectral decomposition can be performed on the selected area, and the proposed network can be fine-tuned with newly collected data. It would lead to an interesting research direction of streamed data analytics for hyperspectral data.

- In chapter 6, we have proposed unsupervised spectral unmixing framework

to extract endmembers and their abundances using spatial and spectral regularizations. We consider the number of endmembers as prior knowledge. However, number of endmembers is unknown and can be restricted by imposing additional constraints such as sparsity on the hidden unit, and thus an optimum subspace can be found for better spectral unmixing.

- We use transfer learning for hyperspectral image super-resolution. One can explore supervised deep learning based model if enough training data is available.

- In the current time, Graphical processing unit (GPU) developer kits are available. These can be used to make the real-time prototype for spectral decomposition using the trained models. In chapter 6, autoencoder is trained for joint estimation of endmembers and their abundances. The learned encoder weights can be used to estimate abundances for new reflectance values. So, one can integrate these weights in the GPU developer kit, and then estimate the abundances for the given reflectance in real time applications.

References

[1] G. Camps-Valls, D. Tuia, L. Gómez-Chova, S. Jiménez, and J. Malo, "Remote sensing image processing," *Synthesis Lectures on Image, Video, and Multimedia Processing*, vol. 5, no. 1, pp. 1–192, 2011.

[2] R. N. Clark, G. A. Swayze, K. E. Livo, R. F. Kokaly, S. J. Sutley, J. B. Dalton, R. R. McDougal, and C. A. Gent, "Imaging spectroscopy: Earth and planetary remote sensing with the usgs tetracorder and expert systems," *Journal of Geophysical Research: Planets*, vol. 108, no. E12, pp. 5–1 to 5–44, 2003. [Online]. Available: https://agupubs.onlinelibrary.wiley.com/doi/abs/10.1029/2002JE001847

[3] A. F. Goetz, G. Vane, J. E. Solomon, and B. N. Rock, "Imaging spectrometry for earth remote sensing," *Science*, vol. 228, no. 4704, pp. 1147–1153, 1985. [Online]. Available: https://science.sciencemag.org/content/228/4704/1147

[4] C. M. Pieters and J. F. Mustard, "Exploration of crustal/mantle material for the earth and moon using reflectance spectroscopy," *Remote Sensing of Environment*, vol. 24, no. 1, pp. 151 – 178, 1988, imaging Spectrometry. [Online]. Available: http://www.sciencedirect.com/science/article/pii/0034425788900107

[5] B.-C. Gao, M. J. Montes, C. O. Davis, and A. F. Goetz, "Atmospheric correction algorithms for hyperspectral remote sensing data of land and ocean," *Remote Sensing of Environment*, vol. 113, pp. S17 – S24, 2009, imaging Spectroscopy Special Issue. [Online]. Available: http://www.sciencedirect.com/science/article/pii/S0034425709000741

[6] F. A. Kruse, "Advances in hyperspectral remote sensing for geologic mapping and exploration," in *Proceedings 9th Australasian remote sensing conference*, 1998, p. 19.

[7] M. Berman, P. Connor, L. Whitbourn, D. Coward, B. Osborne, and M. Southan, "Classification of sound and stained wheat grains using visible and near infrared hyperspectral image analysis," *Journal of Near Infrared Spectroscopy*, vol. 15, no. 6, pp. 351–358, 2007. [Online]. Available: https://doi.org/10.1255/jnirs.754

[8] A. Gowen, C. O'Donnell, P. Cullen, G. Downey, and J. Frias, "Hyperspectral imaging -an emerging process analytical tool for food quality and safety control," *Trends in Food Science & Technology*, vol. 18, no. 12, pp. 590–598, 2007.

[9] M. B. Lopes, J.-C. Wolff, J. M. Bioucas-Dias, and M. A. T. Figueiredo, "Near-infrared hyperspectral unmixing based on a minimum volume criterion for fast and accurate chemometric characterization of counterfeit tablets," *Analytical Chemistry*, vol. 82, no. 4, pp. 1462–1469, 2010, pMID: 20095581. [Online]. Available: https://doi.org/10.1021/ac902569e

[10] G. Begelman, M. Zibulevsky, E. Rivlin, and T. Kolatt, "Blind decomposition of transmission light microscopic hyperspectral cube using sparse representation," *IEEE Transactions on Medical Imaging*, vol. 28, no. 8, pp. 1317–1324, 2009.

[11] L. N. Brewer, J. A. Ohlhausen, P. G. Kotula, and J. R. Michael, "Forensic analysis of bioagents by x-ray and tof-sims hyperspectral imaging," *Forensic Science International*, vol. 179, no. 2, pp. 98 – 106, 2008. [Online]. Available: http://www.sciencedirect.com/science/article/pii/S0379073808001734

[12] J. M. Bioucas-Dias, A. Plaza, N. Dobigeon, M. Parente, Q. Du, P. Gader, and J. Chanussot, "Hyperspectral unmixing overview: Geometrical, statistical, and sparse regression-based approaches," *IEEE Journal of Selected Top-*

ics in Applied Earth Observations and Remote Sensing, vol. 5, no. 2, pp. 354–379, April 2012.

[13] J. M. Bioucas-Dias, A. Plaza, G. Camps-Valls, P. Scheunders, N. Nasrabadi, and J. Chanussot, "Hyperspectral remote sensing data analysis and future challenges," *IEEE Geoscience and Remote Sensing Magazine*, vol. 1, no. 2, pp. 6–36, 2013.

[14] A. Villa, J. Chanussot, J. A. Benediktsson, and C. Jutten, "Spectral unmixing for the classification of hyperspectral images at a finer spatial resolution," *IEEE Journal of Selected Topics in Signal Processing*, vol. 5, no. 3, pp. 521–533, 2011.

[15] G. S. Okin, "Relative spectral mixture analysis - a multitemporal index of total vegetation cover," *Remote Sensing of Environment*, vol. 106, no. 4, pp. 467 – 479, 2007. [Online]. Available: http://www.sciencedirect.com/science/article/pii/S0034425706003488

[16] J. Meola, M. T. Eismann, R. L. Moses, and J. N. Ash, "Detecting changes in hyperspectral imagery using a model-based approach," *IEEE Transactions on Geoscience and Remote Sensing*, vol. 49, no. 7, pp. 2647–2661, 2011.

[17] A. J. Plaza, "Content-based hyperspectral image retrieval using spectral unmixing," in *Image and Signal Processing for Remote Sensing XVII*, L. Bruzzone, Ed., vol. 8180, International Society for Optics and Photonics. SPIE, 2011, pp. 167 – 174. [Online]. Available: https://doi.org/10.1117/12.898833

[18] P. A. Mitchell, "Hyperspectral digital imagery collection experiment (HYDICE)," in *Geographic Information Systems, Photogrammetry, and Geological/Geophysical Remote Sensing*, J. B. Lurie, J. J. Pearson, and E. Zilioli, Eds., vol. 2587, International Society for Optics and Photonics. SPIE, 1995, pp. 70 – 95. [Online]. Available: https://doi.org/10.1117/12.226807

[19] W. M. Porter and H. T. Enmark, "A System Overview Of The Airborne Visible/Infrared Imaging Spectrometer (AVIRIS)," in *Imaging*

Spectroscopy II, G. Vane, Ed., vol. 0834, International Society for Optics and Photonics. SPIE, 1987, pp. 22 – 31. [Online]. Available: https://doi.org/10.1117/12.942280

[20] S. G. Ungar, J. S. Pearlman, J. A. Mendenhall, and D. Reuter, "Overview of the earth observing one (eo-1) mission," *IEEE Transactions on Geoscience and Remote Sensing*, vol. 41, no. 6, pp. 1149–1159, 2003.

[21] H. Kaufmann, K. Segl, L. Guanter, S. Hofer, K. . Foerster, T. Stuffler, A. Mueller, R. Richter, H. Bach, P. Hostert, and C. Chlebek, "Environmental mapping and analysis program (enmap) - recent advances and status," in *2008 IEEE International Geoscience and Remote Sensing Symposium (IGARSS)*, vol. 4, 2008, pp. IV – 109–IV – 112.

[22] L. Candela, R. Formaro, R. Guarini, R. Loizzo, F. Longo, and G. Varacalli, "The prisma mission," in *2016 IEEE International Geoscience and Remote Sensing Symposium (IGARSS)*, 2016, pp. 253–256.

[23] M. J. Barnsley, J. J. Settle, M. A. Cutter, D. R. Lobb, and F. Teston, "The proba/chris mission: a low-cost smallsat for hyperspectral multiangle observations of the earth surface and atmosphere," *IEEE Transactions on Geoscience and Remote Sensing*, vol. 42, no. 7, pp. 1512–1520, 2004.

[24] C. M. Lee, M. L. Cable, S. J. Hook, R. O. Green, S. L. Ustin, D. J. Mandl, and E. M. Middleton, "An introduction to the nasa hyperspectral infrared imager (hyspiri) mission and preparatory activities," *Remote Sensing of Environment*, vol. 167, pp. 6 – 19, 2015, special Issue on the Hyperspectral Infrared Imager (HyspIRI). [Online]. Available: http://www.sciencedirect.com/science/article/pii/S0034425715300419

[25] G. Camps-Valls, D. Tuia, L. Gómez-Chova, S. Jiménez, and J. Malo, *Remote sensing image processing*. Morgan & Claypool Publishers, 2011, vol. 5, no. 1.

[26] A. Remón, S. Sánchez, S. Bernabé, E. S. Quintana-Ortí, and A. Plaza, "Performance versus energy consumption of hyperspectral unmixing

algorithms on multi-core platforms," *EURASIP Journal on Advances in Signal Processing*, vol. 2013, no. 1, p. 68, Apr 2013. [Online]. Available: https://doi.org/10.1186/1687-6180-2013-68

[27] J. W. Boardman, "Analysis, understanding, and visualization of hyperspectral data as convex sets in n space," in *Imaging Spectrometry*, M. R. Descour, J. M. Mooney, D. L. Perry, and L. R. Illing, Eds., vol. 2480, International Society for Optics and Photonics. SPIE, 1995, pp. 14 – 22. [Online]. Available: https://doi.org/10.1117/12.210878

[28] R. Rubinstein, T. Peleg, and M. Elad, "Analysis k-svd: A dictionary-learning algorithm for the analysis sparse model," *IEEE Transactions on Signal Processing*, vol. 61, no. 3, pp. 661–677, Feb 2013.

[29] B. Hapke, *Theory of Reflectance and Emittance Spectroscopy*, ser. Topics in Remote Sensing. Cambridge University Press, 1993.

[30] C. C. Borel and S. A. Gerstl, "Nonlinear spectral mixing models for vegetative and soil surfaces," *Remote Sensing of Environment*, vol. 47, no. 3, pp. 403 – 416, 1994. [Online]. Available: http://www.sciencedirect.com/science/article/pii/0034425794901074

[31] J. M. Bioucas-Dias and J. M. P. Nascimento, "Hyperspectral subspace identification," *IEEE Transactions on Geoscience and Remote Sensing*, vol. 46, no. 8, pp. 2435–2445, 2008.

[32] H. Li, C. Chang, L. Wang, and Y. Li, "Constrained multiple band selection for hyperspectral imagery," in *2016 IEEE International Geoscience and Remote Sensing Symposium (IGARSS)*, 2016, pp. 6149–6152.

[33] I. T. Jolliffe and J. Cadima, "Principal component analysis: a review and recent developments," *Philosophical Transactions of the Royal Society A: Mathematical, Physical and Engineering Sciences*, vol. 374, no. 2065, p. 20150202, 2016.

[34] J. H. Bowles, J. A. Antoniades, M. M. Baumback, J. M. Grossmann, D. Haas, P. J. Palmadesso, and J. Stracka, "Real-time analysis of hyperspectral data sets using NRL's ORASIS algorithm," in *Imaging Spectrometry III*, M. R. Descour and S. S. Shen, Eds., vol. 3118, International Society for Optics and Photonics. SPIE, 1997, pp. 38 – 45. [Online]. Available: https://doi.org/10.1117/12.283841

[35] R. Guerra, L. Santos, S. LÃşpez, and R. Sarmiento, "A new fast algorithm for linearly unmixing hyperspectral images," *IEEE Transactions on Geoscience and Remote Sensing*, vol. 53, no. 12, pp. 6752–6765, 2015.

[36] J. Harsanyi, W. H. Farrand, and C. Chang, "Determining the number and identity of spectral endmembers; an integrated approach using neyman-person eigen-thresholding and iterative constrained rms error minimization," in *Thematic Conf. Geologic Remote Sens*, vol. 1, 1993, pp. 1 – 10.

[37] C.-I. Chang and Q. Du, "Estimation of number of spectrally distinct signal sources in hyperspectral imagery," *IEEE Transactions on Geoscience and Remote Sensing*, vol. 42, no. 3, pp. 608–619, March 2004.

[38] S. S. Vijayashekhar, J. S. Bhatt, and B. Chattopadhyay, "A statistical approach to improve virtual dimensionality of hyperspectral data," in *IGARSS 2019 - 2019 IEEE International Geoscience and Remote Sensing Symposium*, 2019, pp. 2272–2275.

[39] ——, "Virtual dimensionality of hyperspectral data: Use of multiple hypothesis testing for controlling type-i error," *IEEE Journal of Selected Topics in Applied Earth Observations and Remote Sensing*, vol. 13, pp. 2974–2985, 2020.

[40] P. Demartines and J. Herault, "Curvilinear component analysis: a self-organizing neural network for nonlinear mapping of data sets," *IEEE Transactions on Neural Networks*, vol. 8, no. 1, pp. 148–154, 1997.

[41] J. Boardman, "Automating spectral unmixing of aviris data using convex geometry concepts," in *Proc. Ann. JPL Airborne Geosci. Workshop*, vol. 1, 1993, pp. 11 – 14.

[42] J. Boardman, F. A. Kruse, and R. Green, "Mapping target signatures via partial unmixing of aviris data: in summaries," in *Proc. Ann. JPL Airborne Geosci. Workshop*, 1995, pp. 23 – 26.

[43] M. E. Winter, "N-findr: an algorithm for fast autonomous spectral end-member determination in hyperspectral data," pp. 3753 – 3753 – 10, 1999. [Online]. Available: https://doi.org/10.1117/12.366289

[44] J. M. P. Nascimento and J. M. B. Dias, "Vertex component analysis: a fast algorithm to unmix hyperspectral data," *IEEE Transactions on Geoscience and Remote Sensing*, vol. 43, no. 4, pp. 898–910, April 2005.

[45] J. H. Gruninger, A. J. Ratkowski, and M. L. Hoke, "The sequential maximum angle convex cone (SMACC) endmember model," in *Algorithms and Technologies for Multispectral, Hyperspectral, and Ultraspectral Imagery X*, S. S. Shen and P. E. Lewis, Eds., vol. 5425, International Society for Optics and Photonics. SPIE, 2004, pp. 1 – 14. [Online]. Available: https://doi.org/10.1117/12.543794

[46] N. Gillis, *Nonnegative Matrix Factorization*. Philadelphia, PA: Society for Industrial and Applied Mathematics, 2020. [Online]. Available: https://epubs.siam.org/doi/abs/10.1137/1.9781611976410

[47] L. Miao and H. Qi, "Endmember extraction from highly mixed data using minimum volume constrained nonnegative matrix factorization," *IEEE Transactions on Geoscience and Remote Sensing*, vol. 45, no. 3, pp. 765–777, March 2007.

[48] J. Li and J. M. Bioucas-Dias, "Minimum volume simplex analysis: A fast algorithm to unmix hyperspectral data," in *IGARSS 2008 - 2008 IEEE International Geoscience and Remote Sensing Symposium*, vol. 3, July 2008, pp. III – 250–III – 253.

[49] J. M. Bioucas-Dias, "A variable splitting augmented lagrangian approach to linear spectral unmixing," in *2009 First Workshop on Hyperspectral Image and Signal Processing: Evolution in Remote Sensing*, 2009, pp. 1–4.

[50] T. Tu, "Unsupervised signature extraction and separation in hyperspectral images: a noise-adjusted fast independent component analysis," *Optical Engineering*, vol. 39, no. 4, pp. 897 – 906, 2000. [Online]. Available: https://doi.org/10.1117/1.602461

[51] J. M. P. Nascimento and J. M. B. Dias, "Does independent component analysis play a role in unmixing hyperspectral data?" *IEEE Transactions on Geoscience and Remote Sensing*, vol. 43, no. 1, pp. 175–187, 2005.

[52] J. M. P. Nascimento and J. M. Bioucas-Dias, "Hyperspectral unmixing algorithm via dependent component analysis," in *2007 IEEE International Geoscience and Remote Sensing Symposium*, 2007, pp. 4033–4036.

[53] S. Moussaoui, C. Carteret, D. Brie, and A. Mohammad-Djafari, "Bayesian analysis of spectral mixture data using markov chain monte carlo methods," *Chemometrics and Intelligent Laboratory Systems*, vol. 81, no. 2, pp. 137 – 148, 2006. [Online]. Available: http://www.sciencedirect.com/science/article/pii/S0169743905001747

[54] M. Arngren, M. N. Schmidt, and J. Larsen, "Unmixing of hyperspectral images using bayesian non-negative matrix factorization with volume prior," *Journal of Signal Processing Systems*, vol. 65, no. 3, pp. 479–496, Dec 2011. [Online]. Available: https://doi.org/10.1007/s11265-010-0533-2

[55] J. C. Harsanyi and C. . Chang, "Hyperspectral image classification and dimensionality reduction: an orthogonal subspace projection approach," *IEEE Transactions on Geoscience and Remote Sensing*, vol. 32, no. 4, pp. 779–785, 1994.

[56] J. J. SETTLE and N. A. DRAKE, "Linear mixing and the estimation of ground cover proportions," *International Journal of Remote Sensing*, vol. 14, no. 6, pp. 1159–1177, 1993. [Online]. Available: https://doi.org/10.1080/01431169308904402

[57] R. Bro and S. De Jong, "A fast non-negativity-constrained least squares algo-

rithm," *Journal of Chemometrics: A Journal of the Chemometrics Society*, vol. 11, no. 5, pp. 393–401, 1997.

[58] D. C. Heinz and Chein-I-Chang, "Fully constrained least squares linear spectral mixture analysis method for material quantification in hyperspectral imagery," *IEEE Transactions on Geoscience and Remote Sensing*, vol. 39, no. 3, pp. 529–545, Mar 2001.

[59] L. Miao, H. Qi, and H. Szu, "A maximum entropy approach to unsupervised mixed-pixel decomposition," *IEEE Transactions on Image Processing*, vol. 16, no. 4, pp. 1008–1021, April 2007.

[60] R. Heylen, D. Burazerovic, and P. Scheunders, "Fully constrained least squares spectral unmixing by simplex projection," *IEEE Transactions on Geoscience and Remote Sensing*, vol. 49, no. 11, pp. 4112–4122, Nov 2011.

[61] N. Keshava and J. F. Mustard, "Spectral unmixing," *IEEE Signal Processing Magazine*, vol. 19, no. 1, pp. 44–57, Jan 2002.

[62] M. Iordache, J. M. Bioucas-Dias, and A. Plaza, "Sparse unmixing of hyperspectral data," *IEEE Transactions on Geoscience and Remote Sensing*, vol. 49, no. 6, pp. 2014–2039, 2011.

[63] M. D. Iordache, J. M. Bioucas-Dias, and A. Plaza, "Total variation spatial regularization for sparse hyperspectral unmixing," *IEEE Transactions on Geoscience and Remote Sensing*, vol. 50, no. 11, pp. 4484–4502, Nov 2012.

[64] R. Feng, Y. Zhong, and L. Zhang, "An improved nonlocal sparse unmixing algorithm for hyperspectral imagery," *IEEE Geoscience and Remote Sensing Letters*, vol. 12, no. 4, pp. 915–919, April 2015.

[65] S. Zhang, J. Li, H. Li, C. Deng, and A. Plaza, "Spectral spatial weighted sparse regression for hyperspectral image unmixing," *IEEE Transactions on Geoscience and Remote Sensing*, vol. 56, no. 6, pp. 3265–3276, June 2018.

[66] J. S. Bhatt, M. V. Joshi, and M. S. Raval, "A regularization based method for spectral unmixing of imaging spectrometer data," in *Image*

and Signal Processing for Remote Sensing XVIII, L. Bruzzone, Ed., vol. 8537, International Society for Optics and Photonics. SPIE, 2012, pp. 150 – 156. [Online]. Available: https://doi.org/10.1117/12.974649

[67] J. S. Bhatt, M. V. Joshi, and M. S. Raval, "A data-driven stochastic approach for unmixing hyperspectral imagery," *IEEE Journal of Selected Topics in Applied Earth Observations and Remote Sensing*, vol. 7, no. 6, pp. 1936–1946, 2014.

[68] S. S. Vijayashekhar and J. S. Bhatt, "A novel approach for abundance estimation in wavelet domain," in *IGARSS 2019 - 2019 IEEE International Geoscience and Remote Sensing Symposium*, 2019, pp. 2159–2162.

[69] A. Zare and P. Gader, "Sparsity promoting iterated constrained endmember detection in hyperspectral imagery," *IEEE Geoscience and Remote Sensing Letters*, vol. 4, no. 3, pp. 446–450, 2007.

[70] Z. Yang, G. Zhou, S. Xie, S. Ding, J. Yang, and J. Zhang, "Blind spectral unmixing based on sparse nonnegative matrix factorization," *IEEE Transactions on Image Processing*, vol. 20, no. 4, pp. 1112–1125, 2011.

[71] R. Rajabi and H. Ghassemian, "Spectral unmixing of hyperspectral imagery using multilayer nmf," *IEEE Geoscience and Remote Sensing Letters*, vol. 12, no. 1, pp. 38–42, 2015.

[72] J. Li, J. M. Bioucas-Dias, A. Plaza, and L. Liu, "Robust collaborative nonnegative matrix factorization for hyperspectral unmixing," *IEEE Transactions on Geoscience and Remote Sensing*, vol. 54, no. 10, pp. 6076–6090, 2016.

[73] J. S. Bhatt, M. V. Joshi, and S. S. Vijayashekhar, "A multitemporal linear spectral unmixing: An iterative approach accounting for abundance variations," in *2018 9th Workshop on Hyperspectral Image and Signal Processing: Evolution in Remote Sensing (WHISPERS)*, 2018, pp. 1–5.

[74] N. Dobigeon, S. Moussaoui, M. Coulon, J. Tourneret, and A. O. Hero, "Joint bayesian endmember extraction and linear unmixing for hyperspectral im-

agery," *IEEE Transactions on Signal Processing*, vol. 57, no. 11, pp. 4355–4368, 2009.

[75] N. Dobigeon, S. Moussaoui, J.-Y. Tourneret, and C. Carteret, "Bayesian separation of spectral sources under non-negativity and full additivity constraints," *Signal Processing*, vol. 89, no. 12, pp. 2657 – 2669, 2009, special Section: Visual Information Analysis for Security. [Online]. Available: http://www.sciencedirect.com/science/article/pii/S0165168409002187

[76] J. M. P. Nascimento and J. M. Bioucas-Dias, "Hyperspectral unmixing based on mixtures of dirichlet components," *IEEE Transactions on Geoscience and Remote Sensing*, vol. 50, no. 3, pp. 863–878, 2012.

[77] J. S. Bhatt and M. V. Joshi, "Deep learning in hyperspectral unmixing: a review," in *2020 IEEE International Geoscience and Remote Sensing Symposium (IGARSS)*, September 2020, pp. 2189 – 2192.

[78] G. A. Licciardi and F. Del Frate, "Pixel unmixing in hyperspectral data by means of neural networks," *IEEE Transactions on Geoscience and Remote Sensing*, vol. 49, no. 11, pp. 4163–4172, 2011.

[79] X. Zhang, Y. Sun, J. Zhang, P. Wu, and L. Jiao, "Hyperspectral unmixing via deep convolutional neural networks," *IEEE Geoscience and Remote Sensing Letters*, vol. 15, no. 11, pp. 1755–1759, 2018.

[80] R. Guo, W. Wang, and H. Qi, "Hyperspectral image unmixing using autoencoder cascade," in *IEEE 7th Workshop on Hyperspectral Image and Signal Processing: Evolution in Remote Sensing*, 2015, pp. 1–4.

[81] J. J. SETTLE and N. A. DRAKE, "Linear mixing and the estimation of ground cover proportions," *International Journal of Remote Sensing*, vol. 14, no. 6, pp. 1159–1177, 1993. [Online]. Available: https://doi.org/10.1080/01431169308904402

[82] H. Pu, W. Xia, B. Wang, and G. M. Jiang, "A fully constrained linear spec-

tral unmixing algorithm based on distance geometry," *IEEE Transactions on Geoscience and Remote Sensing*, vol. 52, no. 2, pp. 1157–1176, Feb 2014.

[83] J. S. Bhatt and M. V. Joshi, *Regularization in Hyperspectral Unmixing*, ser. Spotlight Author Series in Digital Photograohy. SPIE Press, Washington, USA, 2016, vol. SL25.

[84] A. Jalobeanu, L. Blanc-Feraud, and J. Zerubia, "An adaptive gaussian model for satellite image deblurring," *IEEE Transactions on Image Processing*, vol. 13, no. 4, pp. 613–621, April 2004.

[85] M. V. Joshi and A. Jalobeanu, "MAP estimation for multiresolution fusion in remotely sensed images using an igmrf prior model," *IEEE Transactions on Geoscience and Remote Sensing*, vol. 48, no. 3, pp. 1245–1255, 2010.

[86] S. Nahar and M. V. Joshi, "Dense disparity estimation based on feature matching and igmrf regularization," in *2016 23rd International Conference on Pattern Recognition (ICPR)*, 2016, pp. 3804–3809.

[87] D. Kingma and J. Ba, "Adam: A method for stochastic optimization," *arXiv preprint arXiv:1412.6980*, 2014.

[88] J. S. Cramer, "The origins of logistic regression," 2002. [Online]. Available: https://dx.doi.org/10.2139/ssrn.360300

[89] R. N. Clark, G. A. Swayze, R. Wise, K. E. Livo, T. Hoefen, R. F. Kokaly, and S. J. Sutley, "Usgs digital spectral library splib06a," *US geological survey, digital data series*, vol. 231, 2007. [Online]. Available: http://speclab.cr.usgs.gov/spectral.lib06

[90] S. J. Ford, J. C. McGlone, S. D. Cochran, J. A. Shufelt, W. A. Harvey, and D. M. McKeown, "Analysis of hydice data for information fusion in cartographic feature extraction," in *Geoscience and Remote Sensing Symposium Proceedings, 1998. IGARSS '98. 1998 IEEE International*, vol. 5, Jul 1998, pp. 2702–2706 vol.5.

[91] G. Vane, R. O. Green, T. G. Chrien, H. T. Enmark, E. G. Hansen, and W. M. Porter, "The airborne visible/infrared imaging spectrometer (aviris)," *Remote sensing of environment*, vol. 44, no. 2-3, pp. 127–143, 1993.

[92] F. Zhu, Y. Wang, B. Fan, S. Xiang, G. Meng, and C. Pan, "Spectral unmixing via data-guided sparsity," *IEEE Transactions on Image Processing*, vol. 23, no. 12, pp. 5412–5427, Dec 2014.

[93] Z. Wang and A. C. Bovik, "Mean squared error: Love it or leave it? a new look at signal fidelity measures," *IEEE Signal Processing Magazine*, vol. 26, no. 1, pp. 98–117, Jan 2009.

[94] R. H. Yuhas, A. F. Goetz, and J. W. Boardman, "Discrimination among semi-arid landscape endmembers using the spectral angle mapper (sam) algorithm," 1992.

[95] C.-I. Chang, "An information-theoretic approach to spectral variability, similarity, and discrimination for hyperspectral image analysis," *IEEE Transactions on Information Theory*, vol. 46, no. 5, pp. 1927–1932, Aug 2000.

[96] J. R. Patel, M. V. Joshi, and J. S. Bhatt, "A novel approach for abundance estimation using discontinuity preserving prior," in *2018 IEEE International Geoscience and Remote Sensing Symposium (IGARSS)*, July 2018, pp. 6171–6174.

[97] J. M. Bioucas-Dias and M. A. T. Figueiredo, "Alternating direction algorithms for constrained sparse regression: Application to hyperspectral unmixing," in *2010 2nd Workshop on Hyperspectral Image and Signal Processing: Evolution in Remote Sensing*, June 2010, pp. 1–4.

[98] S. Jia and Y. Qian, "Spectral and spatial complexity-based hyperspectral unmixing," *IEEE Transactions on Geoscience and Remote Sensing*, vol. 45, no. 12, pp. 3867–3879, Dec 2007.

[99] B. Sirkeci, D. Brady, and J. Burman, "Restricted total least squares solutions for hyperspectral imagery," in *2000 IEEE International Conference on Acous-*

tics, Speech, and Signal Processing. Proceedings (Cat. No.00CH37100), vol. 1, 2000, pp. 624–627 vol.1.

[100] Y. H. Hu, H. B. Lee, and F. L. Scarpace, "Optimal linear spectral unmixing," *IEEE Transactions on Geoscience and Remote Sensing*, vol. 37, no. 1, pp. 639–644, Jan 1999.

[101] T. Uezato, R. J. Murphy, A. Melkumyan, and A. Chlingaryan, "Incorporating spatial information and endmember variability into unmixing analyses to improve abundance estimates," *IEEE Transactions on Image Processing*, vol. 25, no. 12, pp. 5563–5575, Dec 2016.

[102] O. Eches, N. Dobigeon, and J. Tourneret, "Enhancing hyperspectral image unmixing with spatial correlations," *IEEE Transactions on Geoscience and Remote Sensing*, vol. 49, no. 11, pp. 4239–4247, Nov 2011.

[103] P. Chen, J. D. B. Nelson, and J. Tourneret, "Toward a sparse Bayesian Markov random field approach to hyperspectral unmixing and classification," *IEEE Transactions on Image Processing*, vol. 26, no. 1, pp. 426–438, Jan 2017.

[104] N. Dobigeon, J. Tourneret, C. Richard, J. C. M. Bermudez, S. McLaughlin, and A. O. Hero, "Nonlinear unmixing of hyperspectral images: Models and algorithms," *IEEE Signal Processing Magazine*, vol. 31, no. 1, pp. 82–94, Jan 2014.

[105] Y. Altmann, N. Dobigeon, S. McLaughlin, and J. Tourneret, "Residual component analysis of hyperspectral image - application to joint nonlinear unmixing and nonlinearity detection," *IEEE Transactions on Image Processing*, vol. 23, no. 5, pp. 2148–2158, 2014.

[106] Y. Altmann, M. Pereyra, and S. McLaughlin, "Bayesian nonlinear hyperspectral unmixing with spatial residual component analysis," *IEEE Transactions on Computational Imaging*, vol. 1, no. 3, pp. 174–185, Sep. 2015.

[107] M. Elad and M. Aharon, "Image denoising via sparse and redundant representations over learned dictionaries," *IEEE Transactions on Image Processing*, vol. 15, no. 12, pp. 3736–3745, Dec 2006.

[108] J. Mairal, M. Elad, and G. Sapiro, "Sparse representation for color image restoration," *IEEE Transactions on Image Processing*, vol. 17, no. 1, pp. 53–69, Jan 2008.

[109] R. Clark, G. Swayze, A. Gallagher, T. King, and W. Calvin, "The us geological survey digital spectral library: Version 1: 0.2 to 3.0 μm. open file report 93-592," *US Geological Survey*, 1993.

[110] J. R. Patel, M. V. Joshi, and J. S. Bhatt, "Abundance estimation using discontinuity preserving and sparsity-induced priors," *IEEE Journal of Selected Topics in Applied Earth Observations and Remote Sensing*, vol. 12, no. 7, pp. 2148–2158, July 2019.

[111] C. Shi and L. Wang, "Incorporating spatial information in spectral unmixing: A review," *Remote Sensing of Environment*, vol. 149, pp. 70 – 87, 2014. [Online]. Available: http://www.sciencedirect.com/science/article/pii/S0034425714001357

[112] [Online]. Available: http://www.ehu.eus/ccwintco/index.php

[113] G. A. Swayze, *The hydrothermal and structural history of the Cuprite Mining District, southwestern Nevada: An integrated geological and geophysical approach*, 1997.

[114] J. Zhao, Y. Zhong, H. Shu, and L. Zhang, "High-resolution image classification integrating spectral-spatial-location cues by conditional random fields," *IEEE Transactions on Image Processing*, vol. 25, no. 9, pp. 4033–4045, 2016.

[115] Y. Zhong, Q. Zhu, and L. Zhang, "Scene classification based on the multifeature fusion probabilistic topic model for high spatial resolution remote

sensing imagery," *IEEE Transactions on Geoscience and Remote Sensing*, vol. 53, no. 11, pp. 6207–6222, 2015.

[116] M. SimÃţes, J. Bioucas?Dias, L. B. Almeida, and J. Chanussot, "A convex formulation for hyperspectral image superresolution via subspace-based regularization," *IEEE Transactions on Geoscience and Remote Sensing*, vol. 53, no. 6, pp. 3373–3388, June 2015.

[117] B. Aiazzi, S. Baronti, and M. Selva, "Improving component substitution pansharpening through multivariate regression of ms +pan data," *IEEE Transactions on Geoscience and Remote Sensing*, vol. 45, no. 10, pp. 3230–3239, 2007.

[118] F. H. Imai and R. S. Berns, "High-resolution multi-spectral image archives: a hybrid approach," in *Color and imaging conference*, vol. 1998, no. 1. Society for Imaging Science and Technology, 1998, pp. 224–227.

[119] N. Koutsias and M. Karteris, "The use of intensity-hue-saturation transformation of landsat-5 thematic mapper data for burned land mapping," *Photogrammetric Engineering and Remote Sensing*, vol. 66, no. 7, pp. 829–840, 2000.

[120] N. Akhtar, F. Shafait, and A. Mian, "Sparse spatio-spectral representation for hyperspectral image super-resolution," in *European Conference on Computer Vision*. Springer, 2014, pp. 63–78.

[121] ——, "Bayesian sparse representation for hyperspectral image super resolution," in *2015 IEEE Conference on Computer Vision and Pattern Recognition (CVPR)*, 2015, pp. 3631–3640.

[122] R. Kawakami, Y. Matsushita, J. Wright, M. Ben-Ezra, Y. Tai, and K. Ikeuchi, "High-resolution hyperspectral imaging via matrix factorization," in *CVPR 2011*, 2011, pp. 2329–2336.

[123] N. Yokoya, T. Yairi, and A. Iwasaki, "Coupled nonnegative matrix factorization unmixing for hyperspectral and multispectral data fusion," *IEEE Transactions on Geoscience and Remote Sensing*, vol. 50, no. 2, pp. 528–537, 2012.

[124] B. Huang, H. Song, H. Cui, J. Peng, and Z. Xu, "Spatial and spectral image fusion using sparse matrix factorization," *IEEE Transactions on Geoscience and Remote Sensing*, vol. 52, no. 3, pp. 1693–1704, 2014.

[125] L. Alparone, L. Wald, J. Chanussot, C. Thomas, P. Gamba, and L. M. Bruce, "Comparison of pansharpening algorithms: Outcome of the 2006 grs-s data-fusion contest," *IEEE Transactions on Geoscience and Remote Sensing*, vol. 45, no. 10, pp. 3012–3021, 2007.

[126] M. Cetin and N. Musaoglu, "Merging hyperspectral and panchromatic image data: qualitative and quantitative analysis," *International Journal of Remote Sensing*, vol. 30, no. 7, pp. 1779–1804, 2009. [Online]. Available: https://doi.org/10.1080/01431160802639525

[127] M. Castelluccio, G. Poggi, C. Sansone, and L. Verdoliva, "Land use classification in remote sensing images by convolutional neural networks," *arXiv preprint arXiv:1508.00092*, 2015. [Online]. Available: https://arxiv.org/abs/1508.00092

[128] C. Dong, C. C. Loy, K. He, and X. Tang, "Image super-resolution using deep convolutional networks," *IEEE Transactions on Pattern Analysis and Machine Intelligence*, vol. 38, no. 2, pp. 295–307, 2016.

[129] S. J. Pan and Q. Yang, "A survey on transfer learning," *IEEE Transactions on Knowledge and Data Engineering*, vol. 22, no. 10, pp. 1345–1359, 2010.

[130] "http://www.ehu.eus/ccwintco/index.php." [Online]. Available: http://www.ehu.eus/ccwintco/index.php

[131] J. Yang, J. Wright, T. S. Huang, and Y. Ma, "Image super-resolution via sparse representation," *IEEE Transactions on Image Processing*, vol. 19, no. 11, pp. 2861–2873, Nov 2010.

[132] R. Zeyde, M. Elad, and M. Protter, "On single image scale-up using sparse-representations," in *International conference on curves and surfaces*. Springer, 2010, pp. 711–730.

[133] H. Chang, D.-Y. Yeung, and Y. Xiong, "Super-resolution through neighbor embedding," in *Computer Vision and Pattern Recognition, 2004. CVPR 2004. Proceedings of the 2004 IEEE Computer Society Conference on*, vol. 1. IEEE, 2004, pp. I–I.

[134] J. R. Patel, M. V. Joshi, and J. S. Bhatt, "A novel approach for hyperspectral image super-resolution using spectral unmixing and transfer learning," in *2020 IEEE International Geoscience and Remote Sensing Symposium (IGARSS)*, September 2020, pp. 1512–1515.

[135] R. Timofte, V. DeÂăSmet, and L. VanÂăGool, "A+: Adjusted anchored neighborhood regression for fast super-resolution," in *Computer Vision – ACCV 2014*, D. Cremers, I. Reid, H. Saito, and M.-H. Yang, Eds. Cham: Springer International Publishing, 2015, pp. 111–126.

[136] Y. Yuan, X. Zheng, and X. Lu, "SpectralâĂŞspatial kernel regularized for hyperspectral image denoising," *IEEE Transactions on Geoscience and Remote Sensing*, vol. 53, no. 7, pp. 3815–3832, 2015.

[137] Z. Wang and A. C. Bovik, "A universal image quality index," *IEEE Signal Processing Letters*, vol. 9, no. 3, pp. 81–84, March 2002.

[138] T. H. Chan, W. K. Ma, A. Ambikapathi, and C. Y. Chi, "A simplex volume maximization framework for hyperspectral endmember extraction," *IEEE Transactions on Geoscience and Remote Sensing*, vol. 49, no. 11, pp. 4177–4193, Nov 2011.

[139] M. D. Craig, "Minimum-volume transforms for remotely sensed data," *IEEE Transactions on Geoscience and Remote Sensing*, vol. 32, no. 3, pp. 542–552, May 1994.

[140] M. Berman, H. Kiiveri, R. Lagerstrom, A. Ernst, R. Dunne, and J. F. Huntington, "Ice: a statistical approach to identifying endmembers in hyperspectral images," *IEEE Transactions on Geoscience and Remote Sensing*, vol. 42, no. 10, pp. 2085–2095, Oct 2004.

[141] S. Jia and Y. Qian, "Constrained nonnegative matrix factorization for hyperspectral unmixing," *IEEE Transactions on Geoscience and Remote Sensing*, vol. 47, no. 1, pp. 161–173, Jan 2009.

[142] S. S. Vijayashekhar and J. S. Bhatt, "A blind spectral unmixing in wavelet domain," *TechRxiv preprint*, 2021.

[143] Y. Qu and H. Qi, "udas: An untied denoising autoencoder with sparsity for spectral unmixing," *IEEE Transactions on Geoscience and Remote Sensing*, vol. 57, no. 3, pp. 1698–1712, March 2019.

[144] F. Zhu, Y. Wang, S. Xiang, B. Fan, and C. Pan, "Structured sparse method for hyperspectral unmixing," *ISPRS Journal of Photogrammetry and Remote Sensing*, vol. 88, pp. 101–118, 2014.

List of Publications

Journal

- J. R. Patel, M. V. Joshi, and J. S. Bhatt, "Abundance estimation using discontinuity preserving and sparsity-induced priors," *IEEE Journal of Selected Topics in Applied Earth Observations and Remote Sensing*, vol. 12, no. 7, pp. 2148–2158, July 2019.

International Conference Proceedings

- J. R. Patel, M. V. Joshi, and J. S. Bhatt, "Spectral unmixing using autoencoder with spatial and spectral regularizations," in *2021 IEEE International Geoscience and Remote Sensing Symposium (IGARSS)*, July 2021, pp. 3321–3324.
- J. R. Patel, M. V. Joshi, and J. S. Bhatt, "A novel approach for hyperspectral image super-resolution using spectral unmixing and transfer learning," in *2020 IEEE International Geoscience and Remote Sensing Symposium (IGARSS)*, September 2020, pp. 1512–1515.
- J. R. Patel, M. V. Joshi, and J. S. Bhatt, "A novel approach for abundance estimation using discontinuity preserving prior," in *2018 IEEE International Geoscience and Remote Sensing Symposium (IGARSS)*, July 2018, pp. 6171–6174.